

AZA-BODIPY BASED CARBONIC ANHYDRASE IX (CAIX) SPECIFIC  
PROBES FOR PHOTODYNAMIC CANCER THERAPY



A Thesis Submitted in Partial Fulfillment of the Requirement for the  
Degree of Master of Science in Chemistry  
Suranaree University of Technology  
Academic Year 2021

สารกลุ่มเอซาโบราณไดเพอร์โรเมธีนที่จำเพาะต่อเอนไซม์คาร์บอนิก  
แอนไฮเดรส ไอโซไซม์ 9 สำหรับการรักษามะเร็งผ่านการกระตุ้นด้วยแสง

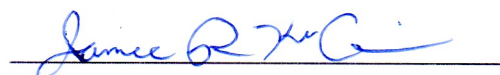


วิทยานิพนธ์นี้เป็นส่วนหนึ่งของการศึกษาตามหลักสูตรปริญญาวิทยาศาสตรมหาบัณฑิต  
สาขาวิชาเคมี  
มหาวิทยาลัยเทคโนโลยีสุรนารี  
ปีการศึกษา 2564

**AZA-BODIPY BASED CARBONIC ANHYDRASE IX (CAIX) SPECIFIC PROBES  
FOR PHOTODYNAMIC CANCER THERAPY**

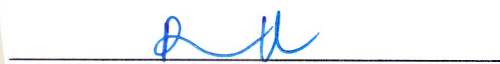
Suranaree University of Technology has approved this thesis submitted in partial fulfillment of the requirement for a master's degree.

Thesis Examining Committee



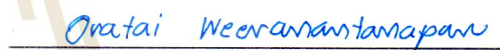
(Prof. Dr. James R. Ketudat-Cairns)

Chairperson



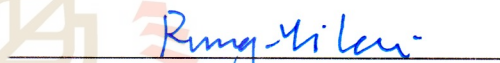
(Asst. Prof. Dr. Anyanee Kamkaew)

Member (Thesis Advisor)



(Asst. Prof. Dr. Oratai Weeranantanapan)

Member



(Dr. Rung-Yi Lai)

Member



(Dr. Kantapat Chansaenpak)

Member



(Assoc. Prof. Dr. Chatchai Jothityangkoon)

Vice Rector for Academic Affairs

and Quality Assurance



(Prof. Dr. Santi Maensiri)

Dean of Institute of Science

ฐิติมา ผิวกลาง : สารกลุ่มเอซาโบรอนไดเพอร์โรเมธินที่จำเพาะต่อเอนไซม์คาร์บอนิกแอนไฮเดรส ไอโซไซม์ 9 สำหรับการรักษามะเร็งผ่านการกระตุ้นด้วยแสง (AZA-BODIPIY BASED CARBONIC ANHYDRASE IX (CAIX) SPECIFIC PROBES FOR PHOTODYNAMIC CANCER THERAPY) อาจารย์ที่ปรึกษา : ผู้ช่วยศาสตราจารย์ ดร.อัญญาณี คำแก้ว, 74 หน้า.

คำสำคัญ: สารกลุ่มเอซาโบรอนไดเพอร์โรเมธิน, คาร์บอนิกแอนไฮเดรส ไอโซไซม์ 9, การรักษาผ่านการกระตุ้นด้วยแสง, สภาวะพร่องออกซิเจน

ในการหลีกเลี่ยงการเนื้องอกภาวะพร่องออกซิเจนที่เกิดจากการรักษามะเร็งแบบใช้แสงเป็นตัวกระตุ้นเป็นความท้าทายที่สำคัญในการรักษามะเร็งประเภทนี้ ซึ่งสามารถนำไปสู่การกลับมาซ้ำของมะเร็งหลังการรักษาและการลุกลามโดยการกระตุ้นของปัจจัยการสร้างหลอดเลือดใหม่ต่าง ๆ เป็นผลให้ประสิทธิภาพการรักษาลดลงอย่างมาก ในงานวิจัยนี้จึงรายงานโมเลกุล AZB-I-CAIX<sub>2</sub> ซึ่งเป็นการเชื่อม acetazolamide (สารต้านการสร้างหลอดเลือดใหม่และสามารถกำหนดเป้าหมายเป็นคาร์บอนิกแอนไฮเดรส ไอโซไซม์ 9 ได้) ร่วมกับสารกลุ่มเอซาโบรอนไดเพอร์โรเมธิน (สารไวแสงที่มีคุณสมบัติสำหรับการรักษาแบบใช้แสงประเภทไกลอินฟราเรด) เพื่อลดผลกระทบจากปัญหาดังกล่าว โดยผลจากการต้านการสร้างหลอดเลือดใหม่ควบคู่กับการรักษามะเร็งแบบใช้แสงเป็นตัวกระตุ้น ผลการทดลองแสดงให้เห็นว่า AZB-I-CAIX<sub>2</sub> มีความจำเพาะเจาะจงต่อเซลล์มะเร็งที่มีจำนวนคาร์บอนิกแอนไฮเดรส ไอโซไซม์ 9 มาก (MDA-MB-231) และมีความเป็นพิษต่อมะเร็งโดยการให้แสงเมื่อเปรียบเทียบกับ AZB-I-control (สารควบคุมที่ไม่มีตัวกำหนดเป้าหมายเป็นคาร์บอนิกแอนไฮเดรส ไอโซไซม์ 9) นอกจากนี้ เพื่อตรวจวัดความเป็นพิษต่อมะเร็งโดยการให้แสงในสัตว์ทดลอง เซลล์มะเร็งของหนูที่พร่องออกซิเจนเป็นแบบจำลองสถานการณ์เนื้องอกที่สามารกระตุ้นการแสดงออกของคาร์บอนิกแอนไฮเดรส ไอโซไซม์ 9 โดยสภาพแวดล้อมที่ขาดออกซิเจน จากผลการทดลอง AZB-I-CAIX<sub>2</sub> มีความสามารถในการจำเพาะต่อสภาวะพร่องออกซิเจนและสามารถกำจัดเซลล์มะเร็งโดยการรักษาแบบใช้แสงเป็นตัวกระตุ้นได้ในสภาวะดังกล่าว ดังนั้นในงานวิจัยนี้ ผู้วิจัยได้แสดงคุณสมบัติของสารไวแสงประเภทไกลอินฟราเรดสำหรับการรักษามะเร็งแบบใช้แสงที่ใช้ประโยชน์จากการยับยั้งคาร์บอนิกแอนไฮเดรส ไอโซไซม์ 9 ทำให้สามารถหลีกเลี่ยงข้อจำกัดจากการเกิดสภาวะพร่องออกซิเจนและการกลับมาอีกครั้งของมะเร็งจากการสร้างหลอดเลือดใหม่ได้ผ่านการยับยั้งคาร์บอนิกแอนไฮเดรส ไอโซไซม์ 9

สาขาวิชาเคมี

ปีการศึกษา 2654

ลายมือชื่อนักศึกษา ฐิติมา ผิวกลาง

ลายมือชื่ออาจารย์ที่ปรึกษา Dr.



## ACKNOWLEDGMENTS

This thesis would not be completed without my advisor, Asst. Prof. Anyanee Kamkaew. She had motivated me enormously. She supplied me with great incentives as well as a big opportunity. My research perspective has broadened to create innovation for humanity in the fields of chemistry and biotherapy. I would like to express my appreciation to the best advisor for her motivation to push me to graduation, her patience in revising all paperwork, her inspiration before and after every presentation, her friendliness that alleviated all the stress, her advice and guidance from the beginning of this research, her celebration of my success, and her time. If I do not have her as my advisor, I could not imagine the way I am experiencing at this time. She is an excellent advisor, eternally.

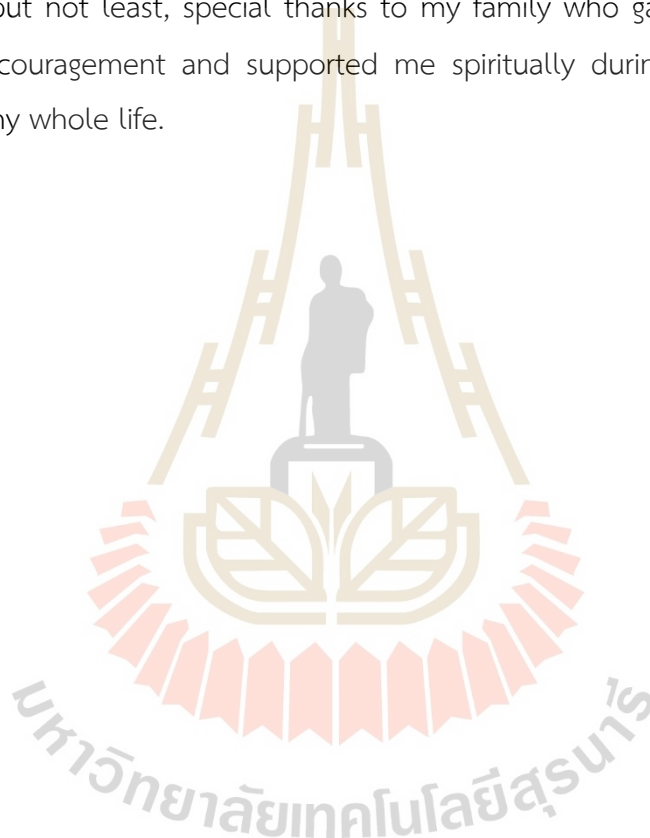
I would want to express my gratitude to AK lab members, especially my friends; Mable, Yui, and Fiat; who are my best friends and classmates since I was an undergraduate student and have supported me in everything they can. I could feel that they were willing to help me whenever I asked them, even with the research works or my stories. I might not accomplish my research if I did not obtain all their support, they are my best mentor and friends for me. Especially, I really would like to thank Dr. Kantapat Chansaenpak who support me with all photophysical property experiments and discussions. Additionally, I also received high-resolution mass spectrometry help from him.

Moreover, I also want to express my appreciation to the Development and Promotion of Science and Technology Talents Project (DPST) for tuition fees, living expenses, and a short-term internship at Texas A&M University, which was a wonderful experience. In addition to all lecturers in the School of Chemistry at Suranaree University of Technology, thanks for their good attitudes and their kindness to push me to be a good student. Also, all staff at the Center for Scientific and Technological Equipment are thanked for their assistance and suggestions for all access to instruments.

This research and innovation activity is funded by National Research Council of Thailand (NRCT) and Suranaree University of Technology (SUT) in contract number: N41D640013. I would like to show my thankfulness to it for providing funding Since receiving this grant in 2021, I have worked hard for the study, valuing all the money invested on a chemical reagent, the expense of employing various equipment to promote excellent research in cancer detection and therapy until the project was performed successfully.

Last but not least, special thanks to my family who gave me unconditional love and encouragement and supported me spiritually during my education and throughout my whole life.

Thitima Pewklang



# CONTENTS

	Page
ABSTRACT IN THAI.....	I
ABSTRACT IN ENGLISH.....	II
ACKNOWLEDGEMENTS.....	III
CONTENTS.....	V
LIST OF SCHEMATICS.....	VIII
LIST OF TABLES.....	IX
LIST OF FIGURES.....	X
LIST OF ABBREVIATIONS.....	XIII
<b>CHAPTER</b>	
<b>I INTRODUCTION.....</b>	<b>1</b>
1.1 Significance of the study.....	1
1.2 Research objectives.....	3
<b>II LITERATURE REVIEW.....</b>	<b>4</b>
2.1 Tumor Angiogenesis.....	4
2.2 Carbonic Anhydrase IX (CAIX) and Its Inhibitors.....	5
2.3 Photosensitizer and Photodynamic Therapy.....	9
2.4 CAIX inhibitor in Combination with Photosensitizer for Photodynamic Therapy.....	11
<b>III EXPERIMENTAL SECTION.....</b>	<b>16</b>
3.1 Synthesis and characterization.....	16
3.1.1 Chemicals reagents.....	16
3.1.2 Characterizations.....	17
3.1.2.1 Nuclear magnetic resonance (NMR).....	17
3.1.2.2 Mass spectrometry (MS).....	17
3.1.3 Synthesis part.....	18
3.1.4 Photophysical properties.....	23

## CONTENTS (Continued)

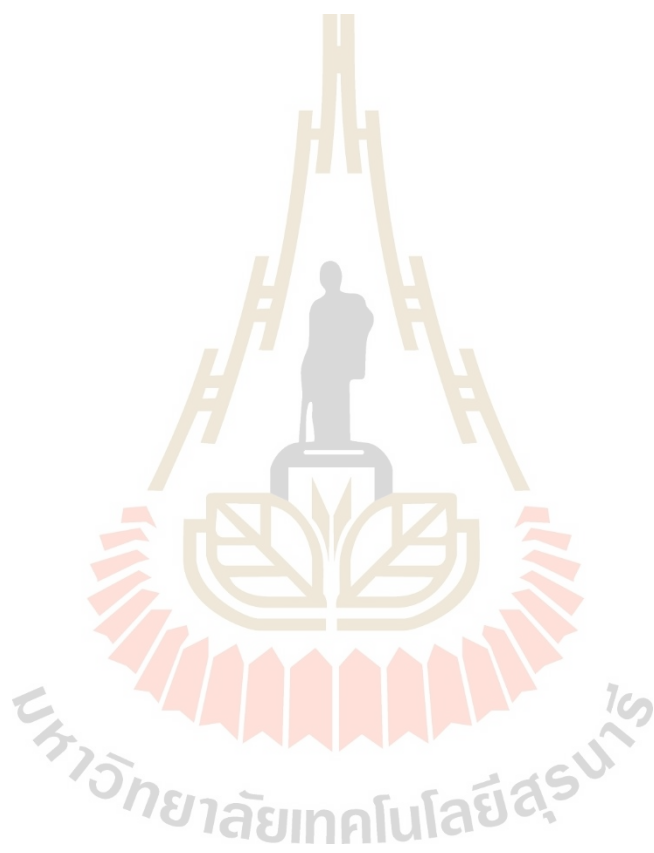
	Page
3.1.4.1 Fluorescence quantum yields ( $\Phi_f$ ).....	23
3.1.4.2 Singlet oxygen quantum yields ( $\Phi_\Delta$ ).....	24
3.2 Cell experiments.....	25
3.2.1 Media for cell culture and chemical reagents for cell experiments....	25
3.2.2 Cell culture.....	25
3.2.3 Time-dependent cellular uptake in human cell lines.....	26
3.2.4 Co-cultured between (+) and (-) CAIX expression cell lines.....	26
3.2.5 Competitive effect with CAIX ligand.....	27
3.2.6 Colocalization study.....	27
3.2.7 Light-induced cell cytotoxicity assay in human cell lines.....	27
3.2.8 Live/Dead staining.....	28
3.2.9 Intracellular Singlet Oxygen Generation.....	28
3.2.10 Murine cell internalization under hypoxia condition.....	29
3.2.11 Murine cell cytotoxicity assay under hypoxia condition.....	29
<b>IV RESULTS AND DISCUSSION.....</b>	<b>31</b>
4.1 Synthesis and characterization of <b>AZB-I-CAIX<sub>2</sub></b> and <b>AZB-I-Control</b> .....	31
4.1.1 Synthesis of <b>AZB-I-CAIX<sub>2</sub></b> and <b>AZB-I-Control</b> .....	31
4.1.2 Characterization of <b>AZB-I-CAIX<sub>2</sub></b> and <b>AZB-I-Control</b> by NMR and Mass spectrometry.....	32
4.1.3 Photophysical properties and fluorescence quantum yields of <b>AZB-I-CAIX<sub>2</sub></b> and <b>AZB-I-Control</b> .....	42
4.1.4 Singlet oxygen quantum yields of <b>AZB-I-CAIX<sub>2</sub></b> and <b>AZB-I-Control</b> .....	44
4.2 Cell experiments.....	46
4.2.1 Cell internalization and CAIX targeting in human cell lines.....	46
4.2.2 Competitive effect with CAIX ligand.....	49
4.2.3 Colocalization study.....	50
4.2.4 Light-induced cell cytotoxicity assay.....	51

## CONTENTS (Continued)

	Page
4.2.5 Live/Dead staining.....	56
4.2.6 Intracellular Singlet Oxygen Generation.....	57
4.2.7 Murine cell internalization under hypoxia condition.....	58
4.2.8 Photo-induced murine cell cytotoxicity assay under hypoxia condition.....	59
<b>V CONCLUSION.....</b>	<b>62</b>
REFERENCES.....	63
APPENDIX.....	72
CURRICULUM VITAE.....	74

## LIST OF SCHEMATIC

Scheme	Page
3.1 Synthetic scheme of AZB-I-CAIX <sub>2</sub> and AZB-I-control.....	18



## LIST OF TABLES

Table	Page
3.1	Chemicals used for the synthesis.....16
3.2	NMR solvents and molecular probes for fluorescence quantum yields and singlet oxygen quantum yields calculation.....17
3.3	Media for cell culture and chemical reagents for cell experiments.....25
4.1	Photophysical properties of <b>AZB-I-CAIX<sub>2</sub></b> and <b>AZB-I-control</b> (1 $\mu$ M).....44
4.2	IC <sub>50</sub> values of <b>AZB-I-CAIX<sub>2</sub></b> after 6 h treatment and irradiation with light in all cells.....54
4.3	IC <sub>50</sub> values of <b>AZB-I-CAIX<sub>2</sub></b> under a hypoxic environment for 12 h before treatment for 6 h and irradiation with the light in 4T1 cells.....61

## LIST OF FIGURES

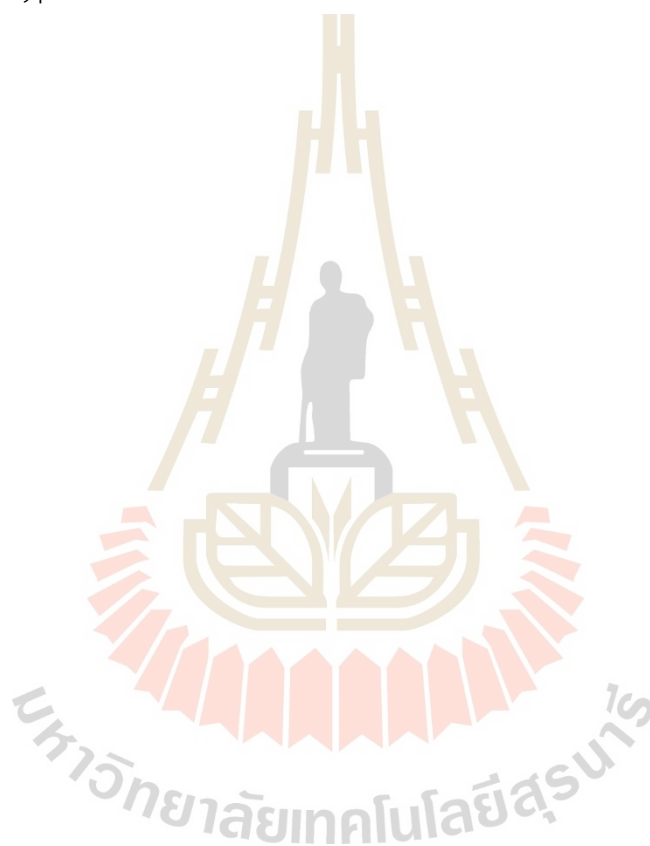
Figure	Page
1.1 Structures of targeting probe (AZB-I-CAIX <sub>2</sub> ) and control (AZB-I-control) in this study.....	3
2.1 The role of angiogenesis in tumor growth.....	5
2.2 CAIX structure and its pH regulatory function in a tumor cell.....	6
2.3 Sulfonamide and acetazolamide derivative structures.....	8
2.4 Influence of heavy atom effect from halogen atom on BODIPY to their singlet oxygen quantum yields.....	9
2.5 Jablonski's diagram of PDT.....	10
2.6 CAIX inhibitor (acetazolamide) in combination with NIR dye and Photosensitizer.....	12
2.7 Illustration of the penetration depth of different types of light and their scattering in tissues.....	14
2.8 Comparing structure and absorption and emission of BODIPY and aza-BODIPY.....	15
4.1 <sup>1</sup> H NMR of compound 1.....	32
4.2 <sup>13</sup> C NMR of compound 1.....	33
4.3 High-resolution ESI <sup>+</sup> MS of compound 1.....	33
4.4 <sup>1</sup> H NMR of compound 2.....	34
4.5 <sup>13</sup> C NMR of compound 2.....	34
4.6 High-resolution ESI <sup>+</sup> MS of compound 2.....	35
4.7 <sup>1</sup> H NMR of compound 3.....	35
4.8 <sup>13</sup> C NMR of compound 3.....	36
4.9 High-resolution ESI <sup>+</sup> MS of compound 3.....	36
4.10 <sup>1</sup> H NMR of compound 4.....	37
4.11 <sup>13</sup> C NMR of compound 4.....	37
4.12 <sup>19</sup> F NMR of compound 4.....	38

## LIST OF FIGURES (Continued)

Figure	Page
4.13 High-resolution ESI <sup>+</sup> MS of compound <b>4</b> .....	38
4.14 <sup>1</sup> H NMR of compound <b>AZB-Control-I</b> .....	39
4.15 <sup>13</sup> C NMR of compound <b>AZB-Control-I</b> .....	39
4.16 <sup>19</sup> F NMR of compound <b>AZB-Control-I</b> .....	40
4.17 High-resolution ESI <sup>+</sup> MS of compound <b>AZB-Control-I</b> .....	40
4.18 <sup>1</sup> H NMR of compound <b>AZB-CAIX<sub>2</sub>-I</b> .....	41
4.19 <sup>13</sup> C NMR of compound <b>AZB-CAIX<sub>2</sub>-I</b> .....	41
4.20 High-resolution ESI <sup>+</sup> MS of compound <b>AZB-CAIX<sub>2</sub>-I</b> .....	42
4.21 Normalized Vis-NIR absorption and emission spectra of <b>AZB-I-CAIX<sub>2</sub></b> and <b>AZB-I-Control</b> (1 μM) in various solvents.....	43
4.22 Reduction absorbance of DPBF at 408 nm by photo-oxidation due to the singlet oxygen formation.....	45
4.23 Relative DPBF absorbance at 408 nm changes of 0.5 μM solutions of <b>AZB-I-CAIX<sub>2</sub></b> , <b>AZB-I-control</b> , and methylene blue at initial rate.....	46
4.24 Time-dependent cell internalization of <b>AZB-I-CAIX<sub>2</sub></b> (5 μM) in (+) CAIX and (-) CAIX level cells.....	47
4.25 Confocal image time-dependent cellular uptake of <b>AZB-I-control</b> compared with <b>AZB-I-CAIX<sub>2</sub></b> (5 μM) in MDA-MB-231 and MCF-7.....	48
4.26 The confocal image displays the 5 μM of <b>AZB-I-CAIX<sub>2</sub></b> for 6 h treatment in co-cultured between MDA-MB-231 and MCF-7.....	49
4.27 CAIX competitive effect. MDA-MB-231 were incubated <b>AZB-I-CAIX<sub>2</sub></b> (5 μM) and CAIX inhibitor (acetazolamide, 100x and 200x) for 6 h.....	50
4.28 Colocalization confocal images and Pearson's coefficients.....	51
4.29 Light-induced cell cytotoxicity of <b>AZB-I-CAIX<sub>2</sub></b> in human cell lines.....	53
4.30 Light-induced cell cytotoxicity of <b>AZB-I-Control</b> in human cell lines.....	55
4.31 The cell viability of all cells after irradiation with light.....	55
4.32 Live/dead cell staining in (+) CAIX cells and (-) CAIX cells.....	57
4.33 Detection of intracellular reactive oxygen species generation.....	58

## LIST OF FIGURES (Continued)

Figure	Page
4.34 Confocal image of murine cell lines (4T1 and 67NR) under normoxia and hypoxia.....	59
4.35 Light-induced cell cytotoxicity of <b>AZB-I-CAIX<sub>2</sub></b> in murine cell lines under hypoxia condition.....	60



## LIST OF ABBREVIATIONS

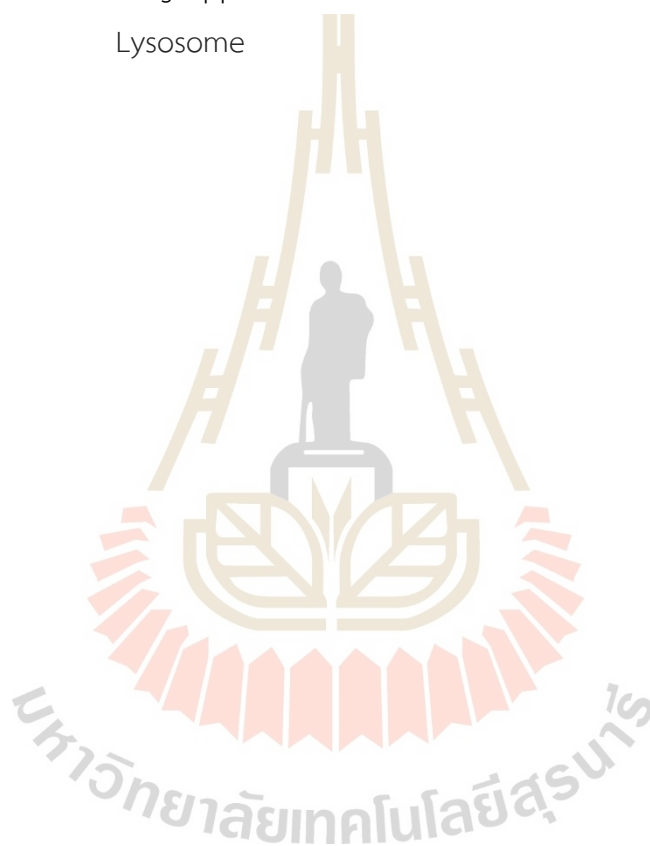
PDT	Photodynamic therapy
PS	Photosensitizer
ROS	Reactive Oxygen Species
$^1\text{O}_2$	Singlet oxygen
HIF	Hypoxia-inducible factor
HIF-1 $\alpha$	Hypoxia-inducible factor 1-alpha
HIF-1 $\beta$	Hypoxia-inducible factor 1-beta
VEGF	Vascular Endothelial Growth Factor
EGF	Epidermal Growth Factor
ANGPT	Angiopoietin
pVHL	Von Hippel-Lindau tumor suppressor protein
PHD2	Prolyl Hydroxylase Domain protein 2
PDGF-B	Platelet-Derived Growth Factor B
ccRCC	Renal cell carcinomas of the clear cell subtype
CA	Carbonic Anhydrase
CAI	Carbonic Anhydrase I
CAII	Carbonic Anhydrase II
CAIX	Carbonic Anhydrase IX
CAXII	Carbonic Anhydrase XII
pH <sub>e</sub>	pH of extracellular
BODIPY	Borondipyrromethene
Aza-BODIPY	Aza-borondipyrromethene
PEG	Polyethylene glycol
NIR	Near-IR
UV	Ultraviolet
SPR	Surface Plasmon Resonance
TLC	Thin-Layer Chromatography

## LIST OF ABBREVIATIONS (Continued)

NMR	Nuclear Magnetic Resonance
MS	Mass Spectrometry
$\lambda_{\max}$	Maximum absorption wavelength
$\lambda_{\text{ex}}$	Excitation wavelength
$\lambda_{\text{em}}$	Emission wavelength
$\delta$	Chemical shift
$J$	Coupling constants
ppm	Parts per million
m/z	Mass-to-charge ratio
$\mu\text{M}$	Micro molar
$K_i$	Inhibitor constant
$\text{IC}_{50}$	Half-maximal inhibitory concentration
$\text{S}_{\text{N}}2$	Substitution Nucleophilic Bimolecular
$\epsilon$	Extinction coefficient
$\Delta\lambda$	Stoke shift wavelength
$\Phi_{\text{f}}$	Fluorescence quantum yields
$\Phi_{\Delta}$	Singlet oxygen quantum yields
$\Phi_{\text{std}}$	Quantum yield of standard
$A_{\text{sample/std}}$	Peak area fluorescence emission of sample or standard
$I_{\text{sample/std}}$	Absorbance at an excitation wavelength of sample or standard
$\eta_{\text{sample/std}}$	Solvent reflective index of sample or standard
$\text{grad}_{\text{sample/std}}$	Slope of the linear fit of sample or standard
<b>F</b>	Absorption correction factor
SD	Standard Deviation
DPBF	1,3-diphenylisobenzofuran
DBB	1,2-dibenzoylbenzene
PI	Propidium iodine
DCFH-DA	2',7'-Dichloro- dihydro-fluorescein diacetate

## LIST OF ABBREVIATIONS (Continued)

DCF	2',7'-dicholorofluorescein
MTT	Methylthiazolyldiphenyl- tetrazolium bromide
ER	Endoplasmic Reticulum
Mito	Mitochondrion
Golgi	Golgi apparatus
Lyso	Lysosome



# CHAPTER I

## INTRODUCTION

### 1.1 Significance of the study

Cancer is a significant cause of illness and death worldwide. There are many treatments to reduce the cancer growth rate and methods have been developed to dramatically harm malignant cells including cancer surgery, radiation therapy, and chemotherapy. However, there are also many severe side effects on normal cells. Photodynamic therapy (PDT) is an attractive cancer treatment, because it is non-invasive and repeatable without significant side effects in clinical areas (Dolmans, Fukumura, and Jain, 2003; Jung et al., 2017; Lucky, Soo, and Zhang, 2015). In PDT, a photosensitizer (PS) is activated by a specific wavelength of light to produce reactive oxygen species (ROS) or singlet oxygen ( $^1\text{O}_2$ ) to harm cells directly by inducing apoptosis. However, in the PDT mechanism, most PDT agents predominantly operate through the type II pathway and consume high oxygen to generate  $^1\text{O}_2$ , which can lead to severe inner hypoxic tumor region ( $< 20$  mmHg  $\text{O}_2$  pressure) due to insufficient blood vessel supply (Ding et al., 2011; Krzykawska-Serda et al., 2014; Song, Feng, Liang, Yang, and Liu, 2016; Wenzl and Wilkens, 2011). PDT-induced hypoxia activates the hypoxia-inducing factor (HIF) signaling pathways, resulting in the production of pro-angiogenic growth factors, such as vascular endothelial growth factor (VEGF), epidermal growth factor (EGF), and angiopoietin (ANGPT), which promote tumor proliferation and angiogenesis. (V. Rapozzi, 2015). Therefore, PDT-induced hypoxia can restrict the therapeutic effects of PDT and reduce its efficiency in tumor destruction.

Carbonic Anhydrase (CA) is an enzyme on the cell surface which have two isoforms namely CAIX and CAXII. The HIF-pathway selectively upregulates CAIX genes to regulate intracellular and extracellular pH, which increases invasive tumor survival in hypoxic environments. (Kaluz, Kaluzová, Liao, Lerman, and Stanbridge, 2009; McDonald, Winum, Supuran, and Dedhar, 2012). Furthermore, CAIX has recently been

identified as a promising target of cancer diagnostic and therapeutic drugs. (Mahalingam, Chu, Liu, Leamon, & Low, 2018; Claudiu T. Supuran, 2008). Recently, an angiogenesis inhibitor in combination with PDT has been realized as a promising approach to enhance PDT and overcome PDT-induced hypoxia by blocking the angiogenic factor (Kalinin et al., 2021). Acetazolamide, CAIX targeted and anti-angiogenesis inhibitor (Vaeteewoottacharn et al., 2016), is a low molecular weight ligand that was considered the potential of anti-angiogenic therapy coupling with PDT.

Aza-BODIPY dye is one of the potential selected PDT agents with  $\lambda_{\max} > 700$  nm in the near-IR (NIR) region, which has less biomolecular scattering resulting in more effective PDT treatment in deep-seated tissues. (Grosjean, Wagnieres, Fontollet, van den Bergh, and Monnier, 1998). Moreover, their structures can be conjugated with many targeting ligands (Kamkaew and Burgess, 2015; Kamkaew et al., 2013; Kue et al., 2018).

In this study, acetazolamide-aza-BODIPY conjugated as a CAIX targeting probe was developed to be a CAIX inhibitor and overcome the hypoxia limitation in PDT. However, most small molecule-drug conjugates in industrial development are based on monovalent targeting moieties (Tavares, Pechar, Chytil, and Etrych, 2021; van der Meel, Vehmeijer, Kok, Storm, and van Gaal, 2013). While some recent studies with small-molecule ligands have suggested that bivalent conjugates provide a better targeting (Brahimi, Ko, Malakhov, Burgess, and Saragovi, 2014; Carlson, Mowery, Owen, Dykhuizen, and Kiessling, 2007; Krall, Pretto, Decurtins, et al., 2014; Staderini, Legname, Bolognesi, and Menéndez, 2013). Aza-BODIPY was conjugated with bivalent acetazolamide to perform cancer-targeting (**AZB-I-CAIX<sub>2</sub>**) and without acetazolamide as control which gives only the PDT effect without any targeting ability (**AZB-I-control**). In general, aza-BODIPY core structures are quite hydrophobic, thus, triethylene glycol is chosen to be a linker in this study, because it can help improve the solubility. Their chemical structures are shown in Figure 1.1.

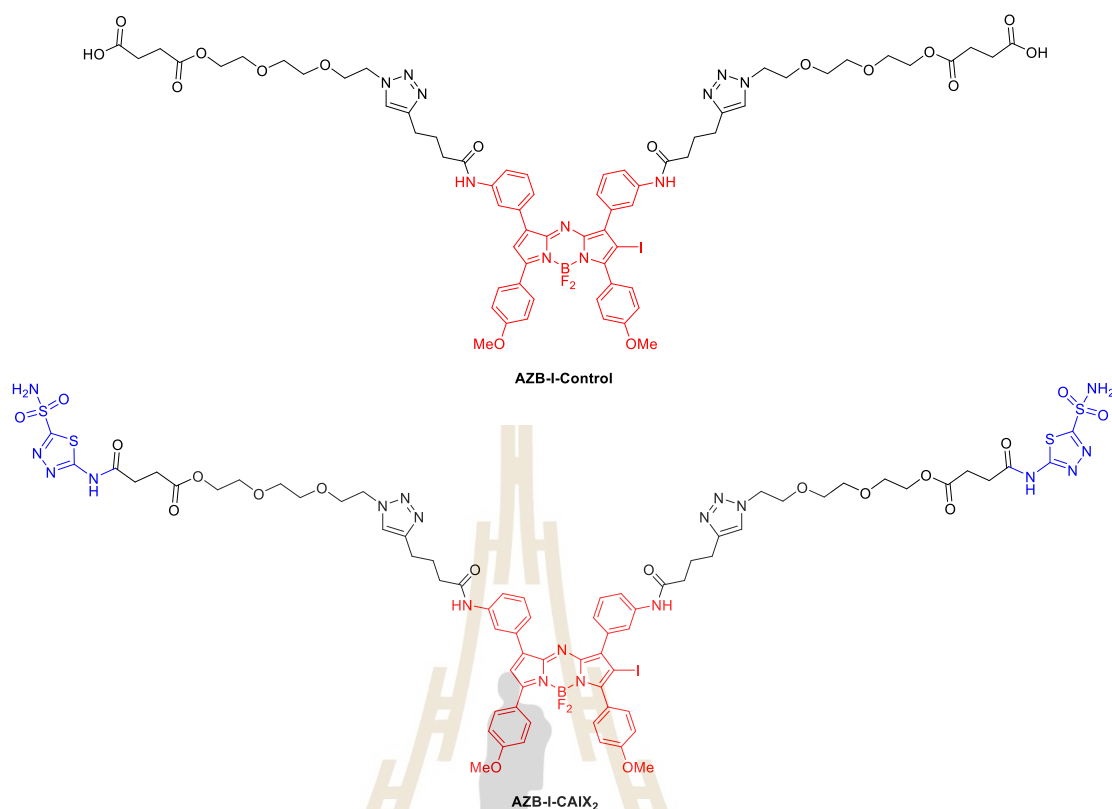


**Figure 1.1** Structures of targeting probe (AZB-I-CAIX<sub>2</sub>) and control (AZB-I-control) in this study.

## 1.2 Research objectives

There are four goals to be developed for the bivalent acetazolamide-aza-BODIPY probes based on CAIX targeting that overcome hypoxia limitation for PDT.

1.2.1 Synthesis and characterization of bivalent acetazolamide conjugated aza-BODIPY and the control probe for CAIX expression cancer-targeting and test for their PDT property (singlet oxygen quantum yields).

1.2.2 To investigate CAIX-dependent specificity of the targeted and control probes using human cell lines with endogenous CAIX expression.

1.2.3 To determine the photocytotoxicity of the PDT effect of the probe (AZB-I-CAIX<sub>2</sub>) in cancer and normal human cell lines.

1.2.4 To evaluate CAIX targeting to overcome the hypoxia limitation for PDT, using PDT to eradicate murine cancer cells with increased CAIX expression due to hypoxia. This goal examines murine cells *in vitro* as a mouse model.

## CHAPTER II

### LITERATURE REVIEW

#### 2.1 Tumor Angiogenesis

Angiogenesis is the process of a new blood vessel building which is controlled by chemical signals. In all tissues, capillaries are necessary for the diffusion exchange of nutrients and oxygen, which is a key to cell growth. Tumor cells feed on the new blood vessels by producing vascular endothelial growth factor (VEGF) which is a signal protein to stimulate the formation of blood vessels for the tumor survival (Nishida, Yano, Nishida, Kamura, and Kojiro, 2006). Angiogenesis has been suggested as a significant factor in cancer regrowth by scientists. Because in the absence of vascular support, tumors could become necrotic or even apoptotic, tumors need a blood supply to grow beyond a few millimeters in size and to send chemical signals that stimulate angiogenesis (Figure 2.1). Furthermore, they can induce the production of angiogenesis signaling molecules in surrounding normal cells. The resulting new blood vessels feed growing tumors with oxygen and nutrients, allowing the tumor cells to invade nearby tissue, to move throughout the body in the process, called metastases. The development of anti-angiogenesis strategies was mannered by knowing that tumors cannot up-regulate angiogenic activity and cannot grow beyond a certain size or spread without a blood supply. There are four main approaches that are used based on the idea that blocking tumor vasculature could be a potential anticancer therapy alternative: suppression of endogenous elements that stimulate the development of blood vessels, the discovery and use of natural inhibitors of angiogenesis, the suppression of chemicals that promote tumor blood vessel penetration into surrounding tissue, and the incapacitation of endothelial cells that are actively growing (Teleanu, Chircov, Grumezescu, and Teleanu, 2019). Additionally, currently, anti-angiogenic drugs including bevacizumab, sunitinib, and pazopanib, are the most applied for various cancer-type treatments (Kikuchi, Stevens, Harada, Oltean, and

Murohara, 2019; Teleanu et al., 2019; Wang, Zorn, and Kuriyan, 2014). However, the drugs have been associated with numerous side effects and relapses owing to invasion and resistance, requiring a combination of other therapies for enhanced outcomes (Mahfouz et al., 2017). Merging therapeutic techniques (e.g., chemotherapy, radiation, immunotherapy, and photodynamic therapy) with anti-angiogenic therapy has considerable synergistic benefits and has started a new frontier in the cancer treatment (Liang et al., 2021).

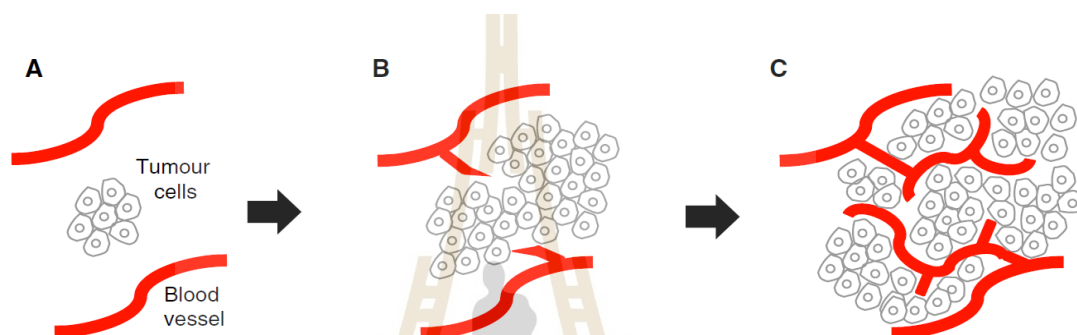


**Figure 2.1** The role of angiogenesis in tumor growth. **A)** When a tumor mass is modest, local blood vessels can provide oxygen and nutrients. **B)** As the tumor expands beyond the ability of local blood vessels, soluble pro-angiogenic factors are generated, encouraging the sprouting of new vessels from existing local blood vessels (sprouting angiogenesis). **C)** These vessels provide a blood supply for the tumor, which is essential for a tumor to develop bigger beyond 2–3 mm in size (Ferrara and Kerbel, 2005).

## 2.2 Carbonic Anhydrase IX (CAIX) and Its Inhibitors

Carbonic anhydrase isozyme IX (CAIX) is a membrane-associated enzyme with a zinc-containing extracellular catalytic active site in reversible hydration of carbon dioxide to hydrogen carbonate and  $H^+$  ( $CO_2 + H_2O \rightarrow H^+ + HCO_3^-$ ) that builds up the acidity in the extracellular in many type of tumors (C. T. Supuran and J. Y. Winum, 2015) (Figure 2.2A). Therefore, CAIX has a key role in the pH balances of both intra- and extracellular environments. The hypoxia regulates the expression of the encoding CAIX through binding the transcription factor HIF-1 $\alpha$  to a hypoxia-responsive element in the gene via the HIF-1 signaling cascade, leading to increased overexpression of CAIX in many tumors as a result of decreasing pH in ( $pH_e = 6.5 - 7.0$ ), while normal tissues

are neutral ( $\text{pH} = 7.4$ ), as shown in Figure 2.2B. Moreover, CAIX exists as a disulfide-linked dimer in its natural state and is expressed in only a small number of healthy tissues. CAIX levels are dramatically raised in many solid tumors in response to hypoxia or mutations in the Von Hippel-Lindau tumor suppressor protein (pVHL), a tumor suppressor, resulting from its role as a master regulator of hypoxia-inducible factor (HIF) activity (Bui et al., 2003).

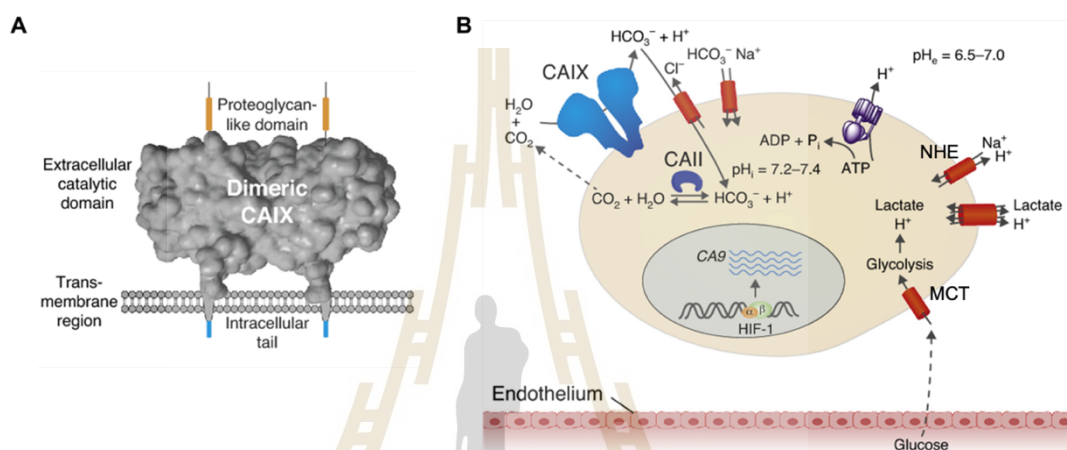


**Figure 2.2** CAIX structure and its pH regulatory function in a tumor cell. **A)** Dimeric CAIX structure from PDB: 3IAI, cofactor zinc is containing transmembrane protein with an extracellular active site, with four domains: an N-terminal proteoglycan-like domain (orange), a catalytic domain (grey), a single-pass helical transmembrane region, and a short intracellular tail (blue). **B)** In cancer cells, molecular systems are involved in pH control and ion transport. Glycolysis produces lactic acid from glucose. (i) The monocarboxylate transporter (MCT) imports lactate and  $\text{H}^+$  ions from the extracellular fluid. (ii) The  $\text{Na}^+-\text{H}^+$  exchanger (NHE), which is active in transformed cells, exports  $\text{H}^+$  and imports  $\text{Na}^+$ , resulting in high intracellular  $\text{Na}^+$  levels, which are prevalent in tumor cells. (iii) The  $\text{H}^+-\text{ATPase}$  pump transports  $\text{H}^+$  to the extracellular space, resulting in low  $\text{pH}_e$ . (iv) Carbonic anhydrase isozyme II (CAII) provides  $\text{H}_2\text{O}$  and  $\text{CO}_2$ , which are exported via aquaporins and utilized by cell-surface CAs to create  $\text{HCO}_3^-$ . (v) Extracellular, CAIX and CAII create  $\text{HCO}_3^-$  ions, which are transferred inside via  $\text{HCO}_3^- - \text{Cl}^-$  anion exchangers. Copyright © 2015 Current Opinion in Chemical Biology (Wichert and Krall, 2015).

According to several preclinical investigations, CAIX induction has been considered one of the crucial pathways in cancer that leads to the development of therapy resistance to poorly basic anticancer drugs. (Becker, 2020; C. T. Supuran, 2017; C. T. Supuran et al., 2018). CAIX inhibitors have been validated as an imaging and therapy target for hypoxia tumors, angiogenic tumors, and metastases of hypoxic tumors, based on the reduction of CAIX catalytic activity can lower the proliferation and metastatic potential of several types of tumor cells. Two types of CAIX inhibitors bind to the active site: first, coordinate with the zinc ion (sulfonamide, sulfamate, sulfamide, dithiocarbamates, xanthate, inorganic anions), and second, do not interact with the metal ion (phenols, polyamines, coumarins). Sulfonamides are the most common class of CAIX inhibitors (Figure 2.3). However, many of them exhibit strong inhibitory activity but less selectivity for the tumor-associated CAIX versus the ubiquitous isoform human CAII (C. T. Supuran, 2012; J. Y. Winum, Rami, Scozzafava, Montero, and Supuran, 2008). Modification of chemical properties of the CAIX inhibitors can be more selective to CAIX via the attachment of different side chains. These side chains can bind to the reach to the active site of CAIX, the area with the most diversity, and selectivity flexible to bind CA isoforms, depending on their size or surface topology. Furthermore, the side chain composition can improve membrane permeability, allowing the inhibitor to bind to extracellular isoforms exclusively or mostly. (Stiti et al., 2008; J.-Y. Winum, 2005; J. Y. Winum, Colinas, and Supuran, 2013). The sulfonamides for CAIX-directed imaging have been published by the Lambin research group (Dubois et al., 2009), with the fluorescent containing sulfonamide group **1**, the experiments revealed that the fluorescent sulfonamide binding to CAIX was reliant on the enzyme production and activation and that it only happened under hypoxic situations. One of the most important findings in the development of sulfonamides for CAIX-directed therapeutics was disclosed in 2011 by the Supuran research group for ureido-substituted benzenesulfonamides inhibitors. (Ahlskog, Dumelin, Trüssel, Mårlind, and Neri, 2009). The researchers discovered a large CAIX-targeted series that had excellent antimetastatic properties *in vivo* in breast cancer xenograft models. When compared to the off-target isoforms of human CAI and CAII, all the reported compounds showed a substantial affinity and selectivity for CAIX. In

other studies, compound **2** was able to significantly block human breast cancer invasion and diminish the cancer cell population *in vivo* (Lock et al., 2013). SignalChem Lifesciences (Vancouver, Canada) is developing an intriguing family of CAIX inhibitors **2**, it is currently in clinical Phase 1a and pharmacokinetics in patients with advanced solid tumors. In addition, the Neri research group reported CAIX targeted based diuretic **3** in 2009 (Ahlskog et al., 2009). It contained an acetazolamide derivative which has a sulfonamide part that is linked with a long side chain. Compound **3** can bind serum albumin, preventing it from internalizing and allowing membrane CAs to be targeted. In the absence of serum albumin, this compound was able to block the enzymatic activity of CAIX and disturb pH regulation in cancer cells. In two human tumor models, *in vivo*, the therapeutic action of **3**, alone or in combination with 5-fluorouracil, resulted in significant tumor growth retardation, but no significant improvement over treatment alone. Moreover, acetazolamide is a clinically used CA inhibitor and shows high selectivity ratio (CAIX/CAI and CAII) by inhibition assay against CAIX, CAI, and CAII *in vitro* (Liu et al., 2018). However, acetazolamide also can suppress tumor metastasis and inhibit the angiogenesis (Abd-El Fattah, Darwish, Fathy, and Shouman, 2017; Jung et al., 2017).

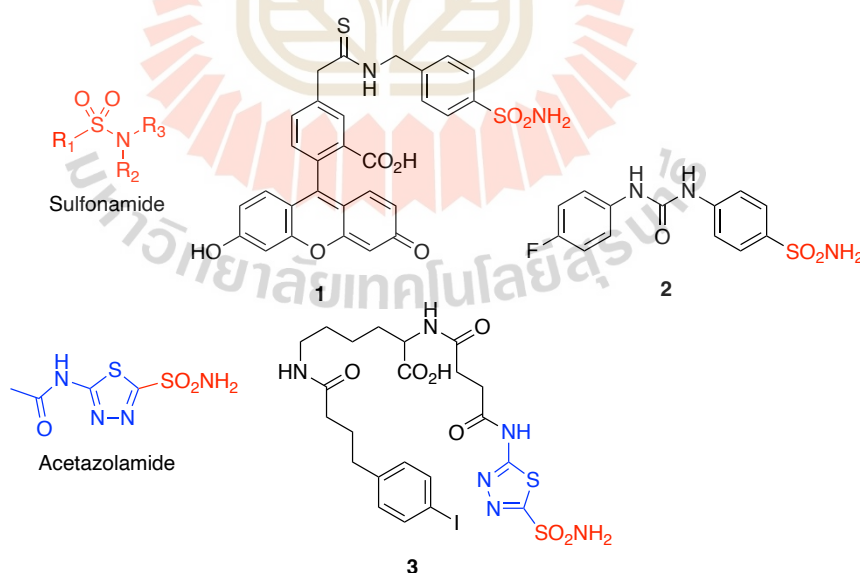
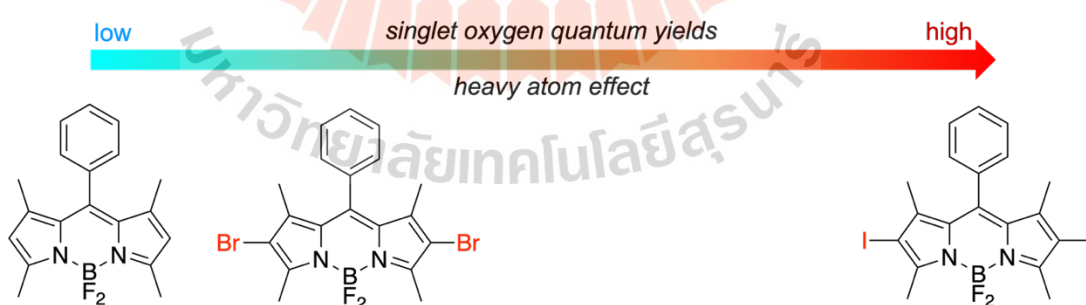


Figure 2.3 Sulfonamide and acetazolamide derivative structures.

### 2.3 Photosensitizer and Photodynamic Therapy

A new class of photodynamic therapy (PDT) agents is based on the boron-dipyrromethene (BODIPY) core containing  $\text{BF}_2$  bridging unit and constitutes a popular class of fluorophores. BODIPYs have many desirable photosensitizer properties, such as high extinction coefficients, strongly singlet oxygen production, and resistance to photobleaching (Yogo, Urano, Ishitsuka, Maniwa, and Nagano, 2005). However, BODIPY as photosensitizer must be modified by heavy atom effect on the core structure of BODIPYs such as halogen atom (H, Br, I) to depress fluorescence to enhance singlet-to-triplet intersystem crossing and make the exciting electron stay longer time in the excited triplet state, long enough to interact with the oxygen to generate reactive oxygen species and singlet oxygen to harm cancer cells. This heavy atom effect from halogen atoms can serve as an electron acceptor to conjugate with the BODIPY core and correspond to a red shift resulting in an upper excited triplet state level which makes slower relaxation energy, so the oxygen has enough time to react with exciting electron. While the heavier iodine atom shows a strongest electron-accepting ability than the bromine and hydrogen atoms respectively. Therefore, iodinated BODIPY has a higher singlet oxygen quantum yield than bromine and hydrogen, as shown in the example in Figure 2.4 (Zou et al., 2017).



**Figure 2.4** Influence of heavy atom effect from halogen atom on BODIPY to their singlet oxygen quantum yields.

PDT (Figure 2.5) uses photochemical reactions to destroy the tumor and has two main mechanisms (type I and II). Photosensitizer (PS) was excited by a suitable wavelength of light. It will be in an excited singlet state. And then, it will go intersystem

crossing and stay longer time in the excited triplet state, long enough to interact with the biomolecule to produce radicals and reactive oxygen species (ROS) in the “Type I” mechanism. In addition, it can interact with oxygen molecules to generate singlet oxygen ( $^1O_2$ ) in the “Type II” mechanism. Both types of mechanisms occur simultaneously, making matters extremely reactive and cytotoxic to destroy the cells directly by inducing apoptosis. The balance between these two mechanism types depends on the concentrations of oxygen and the affinity of the PS as substrates. PDT has three key characteristics of being highly cancer-killing effective: first, the photosensitizer only kills cells in the region that is accumulated and irradiated with the light which generated  $^1O_2$  has a half-life of about 1 ns, and second, deep tissue targeting requires agents that have longer wavelengths of absorption and emission in near-IR (ideally,  $>700$  nm), and third, PDT is highly selective and non-invasive to normal cells after irradiated with the light and no toxic to the cells without the light irradiation because it can affect biological substrates within a 20 nm radius of the area where the PS accumulated. Consequently, PS localization is a critical feature in drug delivery studies to target tissues. (Baldea and Filip, 2012; Huang, 2005). However, the PDT process can lead to secondary effects besides ischemia, hypoxic tissue, and inflammation cells, as well as changes in the expression of chemical molecules that are involved in growth factor receptors, matrix metalloproteinases, cytokines, and proteins of apoptosis, and/or survival pathways.

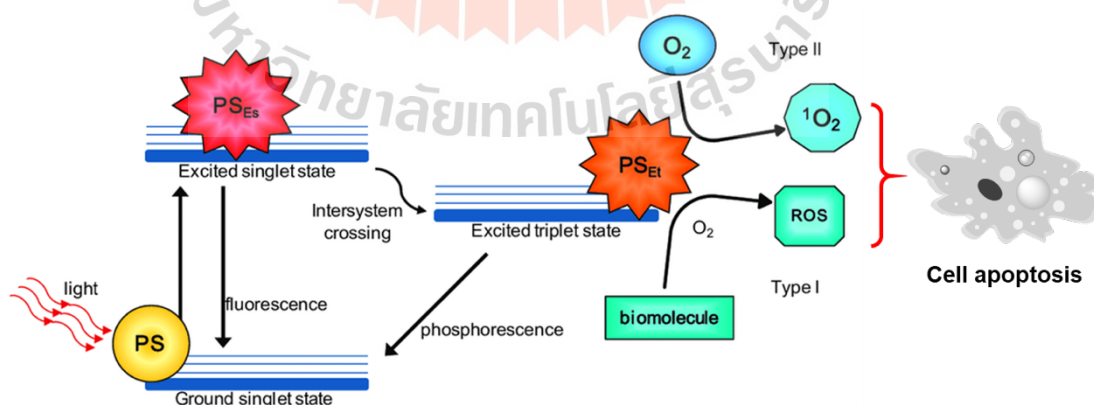


**Figure 2.5** Jablonski's diagram of PDT. The diagram shows a mechanism following a specific light absorption wavelength of photosensitizer (PS) reaching an excited singlet state. Then, After the excited PS (PS<sub>Es</sub>) was an intersystem crossing to triplet excited

state and  $PS_{et}$  can react in two ways, Type I: react with biomolecules through a hydrogen atom (electron) transfer to form radicals, which react with molecular oxygen to generate reactive oxygen species (ROS); or Type II:  $PS_{et}$  on triplet state can react directly with oxygen through energy transfer, generating singlet oxygen ( $^1O_2$ ) that kills the cells directly through inducing apoptosis. Copyright © 2016 Molecules (Calixto, Bernegossi, De Freitas, Fontana, & Chorilli, 2016)

After PDT, the Type II mechanism is considered the principal mechanism (Macdonald and Dougherty, 2001) that causes hypoxia by oxygen depletion and local vascular injury, which can effectively cut off blood flow to the tumor. Hypoxia generated by PDT can improve stability and, as a result, HIF-1 $\alpha$  protein production. (Ferrario and Gomer, 2010; Ferrario et al., 2000; Mitra et al., 2006). Because the prolyl hydroxylase domain protein 2 (PHD2) catalyzes the fast hydroxylation of HIF-1 $\alpha$  resulting in its ubiquitination and proteasomal target in normoxia situations. However, this reaction is blocked in the absence of oxygen or in hypoxia through the stabilization of HIF-1 $\alpha$ . Once stabilized, HIF-1 $\alpha$  can bind to its partner, HIF-1 $\beta$ , which is constitutively expressed, forming the functional transcription factor. Dependent binding of HIF-1 $\alpha$  to HIF-1 $\beta$  is a transcription factor that can translocate to the nucleus and mediates the cellular response to hypoxia by inducing the transcription of a variety of proangiogenic molecules, such as VEGF, platelet-derived growth factor B (PDGF-B), epidermal growth factor (EGF), and angiopoietin (ANGPT), all of which trigger angiogenesis and promote tumor regrowth. (Galbán and Gorospe, 2009; Gallagher-Colombo, Maas, Yuan, and Busch, 2012; Semenza, 2010). Therefore, hypoxia can limit the therapeutic efficacy of PDT.

## 2.4 CAIX inhibitor in Combination with Photosensitizer for Photodynamic Therapy

CAIX has recently been validated as an antitumor/antimetastatic imaging and therapy target. Currently, many sulfonamides of the benzenesulfonamide type, as well as acetazolamide, have been discovered as incredibly potent and specific CAIX inhibitors. CAIX-based solid tumor treatment using small molecule CAIX inhibitors has

already advanced in clinical studies (Phase 1a) (C. T. Supuran and J.-Y. Winum, 2015). However, as shown in Figure 2.6, recently several studies have connected acetazolamide to a fluorescent dye or photosensitizer to offer visualization and therapy in cancer cells.

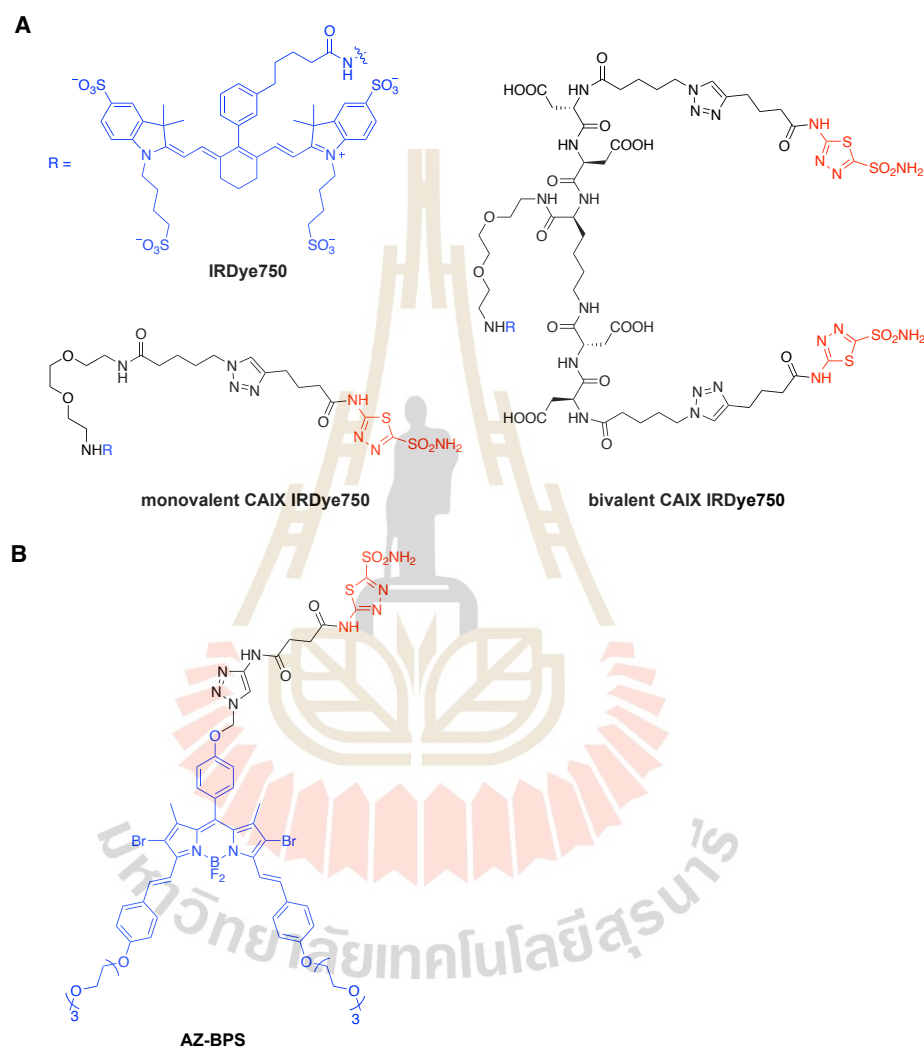


**Figure 2.6** CAIX inhibitor (acetazolamide) in combination with NIR dye and photosensitizer. **A)** IRDyes750 was conjugated with mono- and bi-valent of CAIX inhibitor using peptide linkage. **B)** Dibromo-BODIPY conjugated with monovalent of CAIX inhibitor.

The number equivalent of CAIX inhibitor to near-infrared (NIR) fluorescence dyes was studied by Neri and coworkers (Krall, Pretto, and Neri, 2014). Because bivalent

targeting molecule is more strongly than monovalent one, bivalent antibody formats should be favored for antibody-based pharmaceutical delivery techniques, so this research compared bivalent and monovalent small molecule-drug (acetazolamide) conjugates against CAIX constitute to see an effective chemical method for delivering therapeutic medicines into neoplastic masses (Figure 2.6A). From flow cytometry, the fluorescence intensity for **bivalent CAIX IRDye750** was more shifted than the one observed for **monovalent CAIX IRDye750**, consistent with surface plasmon resonance characterization (SPR) that indicates the bivalent molecule is more selective to CAIX. *In vivo*, the bivalent one showed strongly accumulated in the renal tumor and exhibited significantly longer stay than monovalent on tumor after 24 h injection. Therefore, they suggest that using bivalent small molecule ligand-drug conjugates against CAIX could be a promising therapy option for cancers that are CAIX-positive.

In another literature review, Jung and coworkers have studied newly emerging strategies for cancer treatment with PDT agent-based BODIPY conjugated with monovalent angiogenesis inhibitor, acetazolamide, **AZ-BPS** (Figure 2.6B) to hypoxia tumor via CAIX overexpression (Hyo Sung Jung et al., 2017). They found that with this conjugation, the compound is specifically bound to CAIX overexpressing cancer cells more than CAIX negative cells. This can enhance photocytotoxicity through mitochondrial dysfunction and inhibit tumor angiogenesis through CAIX by generating singlet oxygen. **AZ-BPS** can improve PDT efficiency by combining PDT actions with anti-angiogenesis, delivering a benefit that neither alone can provide. In overcoming the consequences of hypoxia, the strategy incorporating BODIPY targeting CAIX based photo-killing is projected to offer up new opportunities in the field of PDT, while advancing those related to anti-angiogenesis treatment. It is so expected to result in significant new advancements in cancer detection and therapy. However, BODIPY has a maximum absorption of ~500 nm and emission of ~520 nm of the light in the visible region. Because visible regions can be reflected, scattered, and absorbed by biomolecules, such as H<sub>2</sub>O, hemoglobin, and lipid, when entering tissues as shown in Figure 2.7B (Chinen et al., 2015), the image from that UV-vis region permits the real-time capture of wide-field images with a little signal-to-noise ratio and temporal resolution. In comparison to fluorescence imaging, the NIR window offers benefits in

terms of less photon scattering, lower absorption, and minimal interference from biomolecules or autofluorescence. So NIR imaging allows high resolution and a higher signal-to-noise ratio which could be used for diagnostic and therapeutic purposes. Therefore, the NIR window is a suitable region for deeper tissue imaging and treatments (Figure 2.7A).

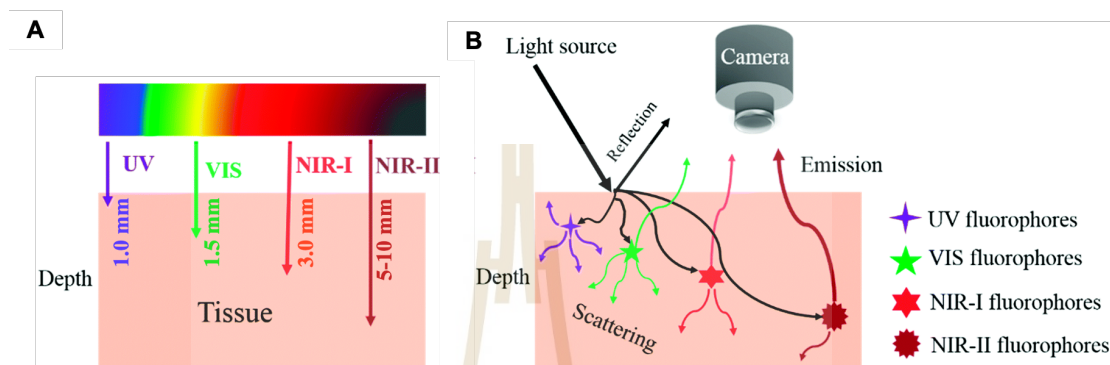


**Figure 2.7** Illustration of the penetration depth of different types of light and their scattering in tissues. A) Tissue penetration depth of light with different wavelengths (UV to NIR regions). B) Light can be reflected or absorbed by biomolecules within the tissue or excite fluorophores to emit light at a different wavelength when irradiating a tissue. Copyright © 2018 Chemical Society Reviews (He, Song, Qu, and Cheng, 2018).

Here, **AZB-I-CAIX<sub>2</sub>** was designed based on aza-BODIPY, which has longer wavelength absorption and shows more red-shift fluorescence emission to the NIR region compared to BODIPY (Figure 2.8) conjugated with the bivalent ligand (acetazolamide) that is better binding and more selective than monovalent. Aza-BODIPY is a NIR dye so the NIR light can irradiate to a deeper issue to the accumulated targeted compound and show less light scattering from biomolecule. In addition, one iodine stayed on the  $\beta$  position of aza-BODIPY to give a heavier atom effect and provide better singlet oxygen quantum yields and fluorescence quantum yields to improve photophysical properties from the visible region into NIR regions. Moreover, polyethylene glycol (PEG) was linked between the ligands and aza-BODIPY to enhance biocompatibility. **AZB-I-CAIX<sub>2</sub>** can selectively target CAIX overexpression cells using the acetazolamide part and overcome the PDT-induced hypoxia limitation thereby making PDT more efficient in hypoxic tumors, which is the initial reason for angiogenesis.

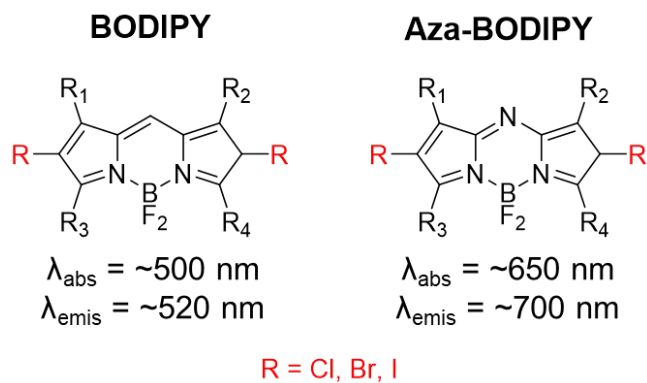
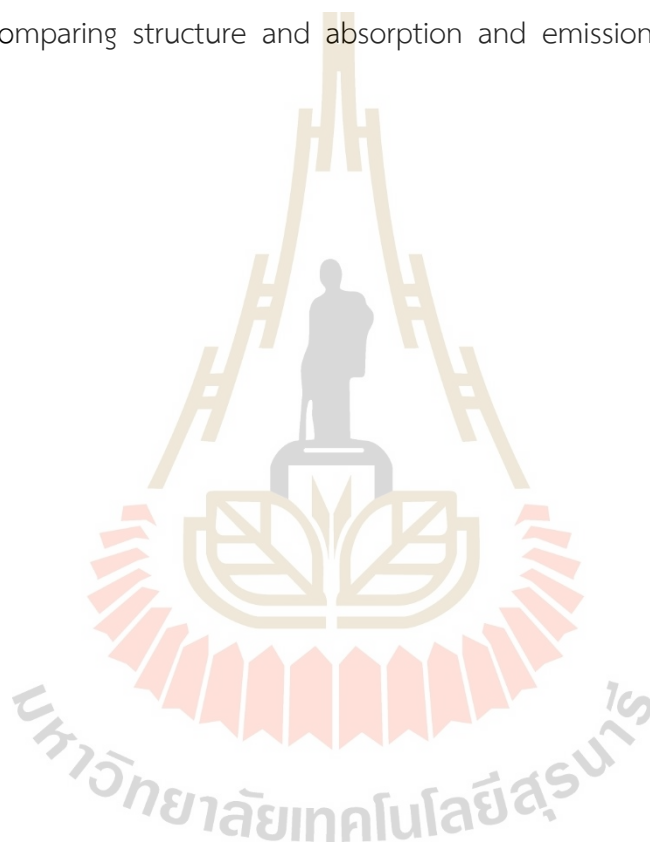


Figure 2.8 Comparing structure and absorption and emission of BODIPY and aza-BODIPY.



## CHAPTER III

### EXPERIMENTAL SECTION

#### 3.1 Synthesis and characterization

##### 3.1.1 Chemicals reagents

Prior to usage, all glassware was oven-dried. All the chemicals and solvents were acquired commercially and utilized without additional purification (Table 3.1 and 3.2).

**Table 3.1** Chemicals used for the synthesis.

Chemicals	Formula	Supplier
Azido-PEG	$C_6H_{13}N_3O_3$	reference <sup>1</sup>
Succinic anhydride	$C_4H_4O_3$	Sigma-Aldrich
Hydrolyzed acetazolamide	$C_2H_4N_4O_2S_2$	reference <sup>2</sup>
1-Ethyl-3-(dimethylaminopropyl) carbodiimide (EDC)	$C_8H_{17}N_3$	Tokyo Chemical Industry
4-Dimethylaminopyridine (DMAP)	$C_7H_{10}N_2$	Tokyo Chemical Industry
Aza-BODIPY (Aza-NH <sub>2</sub> )	$C_{34}H_{28}BF_2N_5O_2$	reference <sup>3</sup>
5-Hexynoic acid	$C_6H_8O_2$	Tokyo Chemical Industry
<i>N</i> -Iodosuccinimide (NIS)	$C_4H_4INO_2$	Tokyo Chemical Industry
Sodium ascorbate (Na ascorbate)	$C_6H_7NaO_6$	Tokyo Chemical Industry
Copper(II) sulfate pentahydrate	$CuSO_4 \cdot 5H_2O$	Carlo Erba

<sup>1</sup> (Pewklang, Chansaenpak, Lai, Noisa, and Kamkaew, 2019)

<sup>2</sup> (More et al., 2018)

<sup>3</sup> (Kamkaew and Burgess, 2015)

**Table 3.2** NMR solvents and molecular probes for fluorescence quantum yields and singlet oxygen quantum yields calculation.

Chemicals	Formula	Supplier
Chloroform-d	CDCl <sub>3</sub>	Sigma-Aldrich
Methanol-d <sub>4</sub>	CD <sub>3</sub> OD	Sigma-Aldrich
Dimethyl sulfoxide-d <sub>6</sub>	(CD <sub>3</sub> ) <sub>2</sub> SO	Sigma-Aldrich
Zinc phthalocyanine (ZnPc)	C <sub>32</sub> H <sub>11</sub> N <sub>8</sub> Zn	Sigma-Aldrich
1,3-Diphenylisobenzofuran (DPBF)	C <sub>20</sub> H <sub>14</sub> O	Tokyo Chemical Industry
Methylthioninium chloride (methylene blue)	C <sub>16</sub> H <sub>18</sub> ClN <sub>3</sub> S	Carlo Erba

### 3.1.2 Characterizations

#### 3.1.2.1 Nuclear magnetic resonance (NMR)

NMR is the instrument that allows being analyzed and identification of molecular structure by monitoring the interaction of nuclear spins once placed in a powerful magnetic field. Therefore, all new compounds were analyzed by <sup>1</sup>H, <sup>13</sup>C, and <sup>19</sup>F NMR spectra on a Bruker-500 MHz spectrometer at room temperature. Chemical shifts of <sup>1</sup>H NMR (500 MHz) spectra were reported in ppm and calibrated from the residue solvent peak, CDCl<sub>3</sub> (7.24 ppm), MeOD-d<sub>4</sub> (3.31 ppm), and DMSO-d<sub>6</sub> (2.50 ppm). <sup>1</sup>H NMR data are reported as follows: chemical shift ( $\delta$ ), resonance splitting (s = singlet, d = doublet, t = triplet, m = multiplet, dd = doublet of doublet), coupling constants (*J*), and a number of protons. <sup>13</sup>C NMR (125 MHz) spectra were also recorded in ppm from the solvent resonance, CDCl<sub>3</sub> (77.23 ppm), MeOD-d<sub>4</sub> (49.00 ppm), and DMSO-d<sub>6</sub> (39.50 ppm).

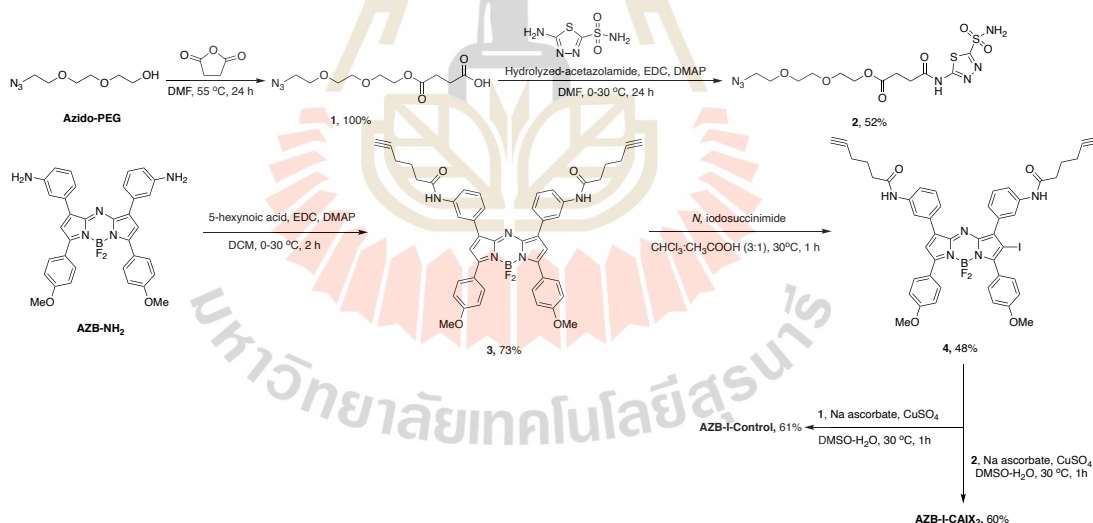
#### 3.1.2.2 Mass spectrometry (MS)

Mass spectrometry is another technique that can identify the molecular weight properties of new compounds. By determining the mass-to-charge ratio (*m/z*) of one or more molecules in a sample can investigate the exact molecular weight of the compound. For this research, all new compounds were analyzed mass by high-

resolution Electrospray Ionization Time of Flight mass spectroscopy (high-resolution ESI-TOF-MS) with positive or negative mode (microTOF-Q, Bruker Daltonics).

### 3.1.3 Synthesis part

AZB-I-CAIX<sub>2</sub> was synthesized via the azide-alkyne Huisgen cycloaddition or click chemistry reaction between the azido group of two acetazolamide moieties (**2**) and the alkynes on iodo-aza-BODIPY derivative (**4**). For the preparation of **4**, amino aza-BODIPY (AZB-NH<sub>2</sub>) was amide coupling with 5-hexynoic acids followed by mono-iodination via electrophilic aromatic substitution reaction. A similar reaction setting was employed to synthesize **AZB-I-control**, except that no acetazolamide (**1**) was used in the linker (Scheme 1). Their purifications were performed by column chromatography employing silica gel (Carlo Erba) as a normal stationary phase. The reactions were followed using analytical thin-layer chromatography (TLC) (Silica gel 60 F254, Merck) and were visualized using a UV cabinet.



Scheme 3.1 Synthetic scheme of AZB-I-CAIX<sub>2</sub> and AZB-I-control

#### 4-(2-(2-(2-azidoethoxy)ethoxy)ethoxy)-4-oxobutanoic acid (**1**).

Azido-PEG (1.1848 g, 6.7666 mmol) and succinic anhydride (3.0340 g, 30.319 mmol) were dissolved in dry DMF (5 mL). Then, the mixture was stirred at 55 °C for 24 h. After that, the reaction mixture was extracted with dichloromethane and DI water (100 mL x 1), and followed by brine (100 mL x 1). The organic layer was dried by

anhydrous  $\text{Na}_2\text{SO}_4$  and the solvent was removed under vacuum pressure. The product was obtained without purification to yield 1.8616 g (100%) of **1** as a pale-yellow oil.  $^1\text{H}$  NMR (500 MHz,  $\text{DMSO-d}_6$ ):  $\delta$  = 12.20 (s, 1H), 4.21 (t,  $J$  = 5.0 Hz, 2H), 3.69 (t,  $J$  = 5.0 Hz, 2H), 3.64 (m, 2H), 3.46 (t,  $J$  = 5.0 Hz, 2H), 2.97 (s, 2H), 2.81 (s, 2H), 2.58 (m, 2H), 2.55 (m, 2H).  $^{13}\text{C}$  NMR (125 MHz,  $\text{DMSO-d}_6$ ):  $\delta$  = 174.0, 172.6, 70.3, 70.1, 69.4, 68.8, 63.8, 50.5, 31.2, 29.2 ppm. MS (high resolution  $\text{ESI}^+$ )  $m/z$ : the calculated value (calcd) for  $\text{C}_{10}\text{H}_{17}\text{N}_3\text{NaO}_6$  ( $[\text{M}+\text{Na}]^+$ ) : 298.1015, found 298.1010.

**2- (2- (2- azidoethoxy)ethoxy)ethyl 4-oxo-4- ((5-sulfamoyl- 1,3,4-thiadiazol-2-yl) amino)butanoate (2).**

**1** (1.5611 g, 5.6744 mmol) and hydrolyzed acetazolamide (1.1235 g, 6.2417 mmol) were dissolved in dry DMF (5 mL). The reaction mixture was then cooled to 0 °C in water bath. 1-Ethyl-3-(3-dimethylaminopropyl)carbodiimide (EDC, 1.6317 g, 8.5117 mmol) and 4-dimethylaminopyridine (DMAP, 0.1386, 1.134 mmol) were added into the mixture at 0 °C. The reaction mixture was stirred in 30 °C for 24 h. After that, the reaction was extracted with DCM and 0.2 M HCl (100 mL x 1), DI water (100 mL x 2) and brine (100 mL x 1), respectively. The organic layer was then dried over anhydrous  $\text{Na}_2\text{SO}_4$  and the solvent was removed by evaporator. The obtained residue was purified by silica chromatography eluting with hexane: ethyl acetate (3: 1 to 2:1) to yield 1.2897 g (52%) of **2** as a pale-yellow oil.  $^1\text{H}$  NMR (500 MHz,  $\text{DMSO-d}_6$ ):  $\delta$  = 8.09 (s, 2H), 7.00 (s, 1H), 4.32 (t,  $J$  = 5.0 Hz, 2H), 3.78 (t,  $J$  = 5.0 Hz, 2H), 3.74 (m, 2H), 3.47 (t,  $J$  = 5.0 Hz, 2H), 3.04 (s, 1H), 3.00 (t,  $J$  = 7.0 Hz, 2H), 2.95 (s, 1H), 2.86 (t,  $J$  = 7.0 Hz, 2H).  $^{13}\text{C}$  NMR (125 MHz,  $\text{DMSO-d}_6$ ):  $\delta$  = 172.8, 171.0, 164.4, 162.9, 70.5, 70.4, 69.9, 69.0, 64.2, 50.7 ppm. MS (high resolution  $\text{ESI}^+$ )  $m/z$ : the calculated value (calcd) for  $\text{C}_{12}\text{H}_{19}\text{N}_7\text{NaO}_7\text{S}_2$  ( $[\text{M}+\text{Na}]^+$ ) : 460.0685, found 460.0680.

**N,N'-((5,5-difluoro-3,7-bis(4-methoxyphenyl)-5H-4l4,5l4-dipyrrolo[1,2-c:2',1'-f][1,3,5,2]triazaborinine-1,9-diy)bis(3,1-phenylene))bis(hex-5-ynamide) (3).**

**AZB-amine** (0.2040 g, 0.3468 mmol) and **5-hexynoic acid** (0.20 mL,  $\rho$  = 1.03, 1.8 mmol) were dissolved in dry dichloromethane (6 mL). The reaction mixture was then cooled to 0 °C 1-Ethyl-3-(3-dimethylaminopropyl)carbodiimide (EDC, 0.2600 g,

1.3563 mmol) and 4-dimethylaminopyridine (DMAP, 0.0350 g, 0.0286 mmol) were added into the mixture at 0 °C. The reaction mixture was stirred in 30 °C for 2 h. After that, the reaction was extracted with DI water (100 mL x 3) and brine (100 mL x 1), respectively. The organic layer was then dried over anhydrous Na<sub>2</sub>SO<sub>4</sub> and the solvent was removed by evaporator. The obtained residue was purified by silica chromatography eluting with dichloromethane: MeOH (100:0 to 98: 2) to yield 0.1972 g (73%) of **3** as a red metallic solid. <sup>1</sup>H NMR (500 MHz, CDCl<sub>3</sub> + 3 drops of MeOD-d<sub>4</sub>): δ = 7.97 (d, *J* = 9.0 Hz, 2H), 7.95 (s, 1H), 7.67 (s, 1H), 7.66 (s, 1H), 7.28 (t, *J* = 6.0 Hz, 1H), 6.95 (s, 1H), 6.92 (d, *J* = 9.0 Hz, 2H), 3.82 (s, 1H), 2.39 (t, *J* = 7.5 Hz, 2H), 2.25 (t, *J* = 7.5 Hz, 2H), 1.97 (s, 1H), 1.85 (t, *J* = 7.5 Hz, 2H). <sup>13</sup>C NMR (125 MHz, CDCl<sub>3</sub> + 3 drops of MeOD-d<sub>4</sub>): δ = 171.4, 162.0, 145.2, 142.3, 138.4, 133.0, 131.7, 129.0, 125.0, 123.9, 120.7, 119.0, 114.9, 83.6, 69.3, 55.4, 35.7, 24.0, 17.9 ppm. MS (high resolution ESI<sup>+</sup>) *m/z*: the calculated value (calcd) for C<sub>46</sub>H<sub>40</sub>BF<sub>2</sub>N<sub>5</sub>NaO<sub>4</sub> ([M+Na]<sup>+</sup>) : 798.3039, found 798.3041.

**N,N'-((5,5-difluoro-2-iodo-3,7-bis(4-methoxyphenyl)-5H-5l4,6l4-dipyrrolo[1,2-c:2',1'-f][1,3,5,2]triazaborinine-1,9-diyl)bis(3,1-phenylene))bis(hex-5-ynamide) (4).**

**3** (97.7 mg, 0.1260 mmol) was dissolved in 6 mL of CHCl<sub>3</sub>: CH<sub>3</sub>COOH (3:1). *N*-iodosuccinimide (NIS, 63.2 mg, 0.281 mmol) was then added to the solution and stirred at 30 °C for 1 h. After that, the reaction was stopped by adding DI water (20 mL) and extracted with sat. Na<sub>2</sub>SO<sub>3</sub> (2 x 20 mL), sat. NaHCO<sub>3</sub> (2 x 20 mL) and brine (1 x 100 mL), respectively. The organic layer was then dried over anhydrous Na<sub>2</sub>SO<sub>4</sub> and the solvent was removed by evaporator. The obtained residue was purified by silica chromatography eluting with 100% dichloromethane to yield 54.5 mg (48%) of **4** as a red metallic solid. <sup>1</sup>H NMR (500 MHz, DMSO-d<sub>6</sub>): δ = 10.21 (s, 1H), 10.07 (s, 1H), 8.27 (d, *J* = 9.0 Hz, 2H), 8.24 (s, 1H), 8.17 (s, 1H), 7.93 (d, *J* = 8.0 Hz, 1H), 7.80 (d, *J* = 7.5 Hz, 1H), 7.72 (m, 2H), 7.69 (s, 1H), 7.67 (s, 1H), 7.53 (m, 1H), 7.51 (m, 1H), 7.38 (t, *J* = 7.5 Hz, 1H), 7.21 (d, *J* = 9.0 Hz, 2H), 7.18 (d, *J* = 9.0 Hz, 2H), 3.95 (s, 3H), 3.94 (s, 3H), 2.91 (d, *J* = 8.5 Hz, 2H), 2.55 (m, 2H), 2.33 (d, *J* = 7.5 Hz, 2H), 1.87 (dd, *J* = 7.0, 5.0 Hz, 2H). <sup>13</sup>C NMR (125 MHz, DMSO-d<sub>6</sub>): δ = 207.3, 171.2, 163.7, 162.4, 161.0, 155.8, 146.8, 145.6, 143.8, 142.9, 139.9, 139.6, 133.3, 133.2, 132.7, 131.8, 129.3, 128.8, 126.1, 125.2, 124.2, 122.6, 122.1, 121.9, 121.1, 120.4, 119.9, 115.2, 113.8, 84.5, 72.1, 56.2, 55.8, 35.5, 24.4, 17.9 ppm, <sup>19</sup>F

NMR (470 MHz, DMSO- $d_6$ ):  $\delta$  = -131.23 (q,  $J$  = 33.0 Hz,  $\text{BF}_2$ ) ppm. MS (high resolution ESI<sup>+</sup>)  $m/z$ : the calculated value (calcd) for  $\text{C}_{46}\text{H}_{39}\text{BF}_2\text{IN}_5\text{NaO}_4$  ( $[\text{M}+\text{Na}]^+$ ): 924.2006, found 924.2008.

**4,4'-((((((((((5,5-difluoro-2-iodo-3,7-bis(4-methoxyphenyl)-5H-5l4,6l4-dipyrrolo [1,2-c:2',1'-f][1,3,5,2]triazaborinine-1,9-diyl)bis(3,1-phenylene))bis(azanediyl)) bis(4-oxobutane-4,1-diyl))bis(1H-1,2,3-triazole-4,1-diyl))bis(ethane-2,1-diyl)) bis(oxy))bis(ethane-2,1-diyl))bis(oxy))bis(ethane-2,1-diyl))bis(oxy))bis(4-oxobutanoic acid) (AZB-I-Control)**

**4** (28.7 mg, 0.0318 mmol) and **1** (38.4 mg, 0.140 mmol) were dissolved in DMSO (0.5 mL). To the reaction mixture was added freshly prepared Na ascorbate solution (1.5 mg in 20  $\mu\text{L}$  of DI water, 7.6  $\mu\text{mol}$ ) and freshly prepared  $\text{CuSO}_4 \cdot 5\text{H}_2\text{O}$  solution (1.0 mg in 20  $\mu\text{L}$  of DI water, 4.0  $\mu\text{mol}$ ), respectively. The resulting mixture was stirred vigorously at 30  $^\circ\text{C}$  for 1 h. After that, the reaction was stopped and precipitated by adding DI water (20 mL). Then, the product was obtained by centrifugation (5000 rpm for 10 min) and washed with DI water (20 mL) for 5 times. The product was obtained without purification to yield 28.1 mg (61%) of **AZB-I-Control** as a dark green solid.  $^1\text{H}$  NMR (500 MHz, DMSO- $d_6$ ):  $\delta$  = 12.28 (s, 2H), 10.18 (s, 1H), 10.04 (s, 1H), 8.27 (d,  $J$  = 8.5 Hz, 2H), 8.25 (s, 1H), 8.17 (s, 1H), 7.94 (s, 1H), 7.92 (s, 1H), 7.89 (s, 1H), 7.79 (d,  $J$  = 8.0 Hz, 1H), 7.71 (s, 1H), 7.68 (d,  $J$  = 8.5 Hz, 2H), 7.53 (m, 1H), 7.50 (m, 1H), 7.36 (t,  $J$  = 7.5 Hz, 1H), 7.21 (d,  $J$  = 8.5 Hz, 2H), 7.18 (d,  $J$  = 8.5 Hz, 2H), 4.54 (m, 4H), 4.17 (m, 4H), 3.96 (s, 3H), 3.95 (s, 3H), 3.87 (m, 4H), 3.62 (m, 4H), 3.59 (m, 4H), 3.57 (m, 4H), 2.77 (m, 4H), 2.54 (m, 4H), 2.53 (m, 4H), 2.51 (m, 4H), 2.00 (m, 4H).  $^{13}\text{C}$  NMR (125 MHz, DMSO- $d_6$ ):  $\delta$  = 173.8, 172.6, 171.6, 163.7, 162.4, 161.0, 155.8, 146.8, 145.6, 143.9, 142.9, 140.0, 139.7, 133.3, 133.2, 132.7, 131.8, 129.3, 128.8, 126.1, 125.2, 124.2, 122.8, 122.6, 122.1, 121.8, 121.1, 120.4, 119.8, 115.4, 115.2, 113.8, 70.1, 70.0, 69.2, 68.7, 63.8, 56.2, 55.8, 49.9, 36.3, 36.2, 29.1, 25.4, 25.3, 25.1 ppm,  $^{19}\text{F}$  NMR (470 MHz, DMSO- $d_6$ ):  $\delta$  = -131.23 (q,  $J$  = 33.0 Hz,  $\text{BF}_2$ ) ppm. MS (high resolution ESI<sup>+</sup>)  $m/z$ : the calculated value (calcd) for  $\text{C}_{66}\text{H}_{73}\text{BF}_2\text{IN}_{11}\text{O}_{16}$  ( $[\text{M}]^+$ ): 1451.4343, found 1451.4348.

2-(2-(2-(4-(4-((3-(5,5-difluoro-2-iodo-3,7-bis(4-methoxyphenyl)-9-(3-(4-(1-(2-(2-(2-(4-oxo-4-((5-sulfamoyl-1,3,4-thiadiazol-2-yl)amino)butanoyl)oxy)ethoxy)ethoxy)ethyl)-1H-1,2,3-triazol-4-yl)butanamido)phenyl)-5H-5l4,6l4-dipyrrolo[1,2-c:2',1'-f][1,3,5,2]triazaborinin-1-yl)phenyl)amino)-4-oxobutyl)-1H-1,2,3-triazol-1-yl)ethoxy)ethoxy)ethyl4-oxo-4-((5-sulfamoyl-1,3,4-thiadiazol-2-yl)amino)butanoate (AZB-I-CAIX<sub>2</sub>)

**4** (40.0 mg, 0.0444 mmol) and **2** (60.8 mg, 0.139 mmol) were dissolved in DMSO (0.5 mL). To the reaction mixture was added freshly prepared Na ascorbate solution (3.0 mg in 20  $\mu$ L of DI water, 15  $\mu$ mol) and freshly prepared CuSO<sub>4</sub>•5H<sub>2</sub>O solution (2.0 mg in 20  $\mu$ L of DI water, 8.0  $\mu$ mol), respectively. The resulting mixture was stirred vigorously at 30 °C for 1 h. After that, the reaction was stopped and precipitated by adding DI water (20 mL). Then, the product was obtained by centrifugation (5000 rpm for 10 min) and washed with DI water (20 mL) for 5 times. The product was obtained without purification to yield 48.4 mg (61%) of **AZB-I-CAIX<sub>2</sub>** as a dark green solid. <sup>1</sup>H NMR (500 MHz, DMSO-d<sub>6</sub>):  $\delta$  = 10.07 (s, 1H), 9.93 (s, 1H), 8.30 (s, 4H), 8.19 (d, *J* = 8.5 Hz, 2H), 8.16 (s, 1H), 8.09 (s, 1H), 7.86 (m, 1H), 7.85 (m, 1H), 7.84 (m, 1H), 7.70 (d, *J* = 7.5 Hz, 2H), 7.62 (s, 1H), 7.60 (d, *J* = 8.5 Hz, 2H), 7.45 (m, 1H), 7.42 (m, 1H), 7.29 (t, *J* = 7.5 Hz, 1H), 7.13 (d, *J* = 8.5 Hz, 2H), 7.10 (d, *J* = 8.5 Hz, 2H), 4.46 (t, *J* = 6.0 Hz, 4H), 4.09 (t, *J* = 4.0 Hz, 4H), 3.88 (s, 3H), 3.87 (s, 3H), 3.79 (t, *J* = 6.0 Hz, 4H), 3.54 (t, *J* = 4.0 Hz, 4H), 3.49 (m, 4H), 3.48 (m, 4H), 2.80 (m, 4H), 2.69 (m, 4H), 2.68 (t, *J* = 6.5 Hz, 4H), 2.42 (m, 4H), 1.94 (m, 4H). <sup>13</sup>C NMR (125 MHz, DMSO-d<sub>6</sub>):  $\delta$  = 171.6, 171.5, 171.4, 171.2, 171.1, 163.7, 152.4, 161.0, 155.9, 146.8, 145.6, 142.9, 140.0, 139.6, 133.3, 133.2, 132.7, 131.8, 129.3, 128.8, 126.1, 125.2, 124.3, 122.7, 122.6, 122.1, 121.9, 121.1, 120.4, 120.0, 115.2, 114.9, 113.8, 72.8, 72.1, 70.1, 69.2, 60.7, 56.2, 55.8, 49.7, 36.3, 35.6, 25.4, 25.1, 24.4, 17.9 ppm. MS (high resolution ESI<sup>+</sup>) *m/z*: the calculated value (calcd) for C<sub>70</sub>H<sub>76</sub>BF<sub>2</sub>IN<sub>19</sub>O<sub>18</sub>S<sub>4</sub> ([M-H]<sup>+</sup>): 1774.3599, found 1774.3587.

### 3.1.4 Photophysical properties

#### 3.1.4.1 Fluorescence quantum yields ( $\Phi_f$ )

The UV-vis-NIR absorption and fluorescence spectra were recorded on UV-vis Spectrophotometer (Agilent Technologies Cary 300) and Spectrofluorometer (PerkinElmer LS55), respectively. Briefly, **AZB-I-CAIX<sub>2</sub>** and **AZB-I-Control** were prepared as solutions in DMSO. The stock solutions of **AZB-I-CAIX<sub>2</sub>** and **AZB-I-Control** were added to a quartz cell with a 1 cm path length in various solvents (CHCl<sub>3</sub>, DMSO, MeOH, and PBS 3% tween 80) to a final concentration of 1  $\mu$ M. The fluorescence spectra used the following parameters of excitation wavelengths = 670 nm, excitation slit widths = 10 nm, and emission slit widths = 10 nm. The fluorescence quantum yields were calculated using equation (1) as the ratio of the number of photons released to the number of photons absorbed and related to the fluorescence quantum yield standard reagent (Zn-pthalocyanine in pyridine,  $\Phi_{\text{std}} = 0.30$ ) (Zhang, Li, Niu, Sun, and Liu, 2009).

$$\Phi_f = \Phi_{\text{std}} \left( \frac{A_{\text{sample}}}{A_{\text{std}}} \right) \left( \frac{I_{\text{std}}}{I_{\text{sample}}} \right) \left( \frac{\eta_{\text{sample}}}{\eta_{\text{std}}} \right)^2 \quad (1)$$

Where  $\Phi_f$  = Fluorescence quantum yield of **AZB-I-CAIX<sub>2</sub>** and **AZB-I-Control**

$\Phi_{\text{std}}$  = Fluorescence quantum yield of Zn-pthalocyanine (0.30)

$A_{\text{sample}}$  = Peak area fluorescence emission of **AZB-I-CAIX<sub>2</sub>** and **AZB-I-Control**

$A_{\text{std}}$  = Peak area fluorescence emission of Zn-pthalocyanine

$I_{\text{sample}}$  = Absorbance at an excitation wavelength of **AZB-I-CAIX<sub>2</sub>** and **AZB-I-Control**

$I_{\text{std}}$  = Absorbance at an excitation wavelength of Zn-pthalocyanine

$\eta_{\text{sample}}$  = Solvent reflective index of **AZB-I-CAIX<sub>2</sub>** and **AZB-I-Control**

$\eta_{\text{std}}$  = Solvent reflective index of Zn-pthalocyanine

### 3.1.4.2 Singlet oxygen quantum yields ( $\Phi_{\Delta}$ )

Singlet oxygen generation of **AZB-I-CAIX<sub>2</sub>** and **AZB-I-Control** was determined by the reaction of singlet oxygen (<sup>1</sup>O<sub>2</sub>) with 1,3-diphenylisobenzofuran (DPBF) as a standard singlet oxygen scavenger. The singlet oxygen amount was quantified by absorbance reduction of DPBF at 408 nm. **AZB-I-CAIX<sub>2</sub>** and **AZB-I-Control** were exposed with the light using a red LED lamp (660 nm, power density of 8.7 mW cm<sup>-2</sup>) in DMSO at 25 °C compared to a standard singlet oxygen generating dye (methylene blue). A solution of DMSO containing 50 μM of DPBF as a singlet oxygen scavenger and 0.5 μM of **AZB-I-CAIX<sub>2</sub>** in a quartz cell with 1 cm path length. The DPBF solution in DMSO (negative control), a solution containing 0.5 μM of **AZB-I-Control**, and the solution containing 0.5 μM methylene blue, comparative control,  $\Phi_{\Delta} = 0.52$  (Jung et al., 2017) were also examined. After being exposed to the light, the absorbance reduction of DPBF at 408 nm was measured during 0-60 s by an Agilent UV-Vis spectrophotometer (Carry 300). The changing of absorbance at the initial rate is plotted against irradiation time. The singlet oxygen quantum yield was calculated according to equation (2).

$$\Phi_{\Delta} = \Phi_{\text{std}} \left( \frac{\text{grad}_{\text{sample}}}{\text{grad}_{\text{std}}} \right) \left( \frac{F_{\text{std}}}{F_{\text{sample}}} \right) \quad (2)$$

Where  $\Phi_{\Delta}$  = Singlet oxygen quantum yield of **AZB-I-CAIX<sub>2</sub>** and **AZB-I-Control**

$\Phi_{\text{std}}$  = Singlet oxygen quantum yield of methylene blue (0.52)

$\text{grad}_{\text{sample}}$  = Slope of the linear fit of **AZB-I-CAIX<sub>2</sub>** and **AZB-I-Control**

$\text{grad}_{\text{std}}$  = Slope of the linear fit of methylene blue

$F$  = Absorption correction factor ( $F=1-10^{-\text{abs}}$ ; abs represent absorbance at 660 nm of **AZB-I-CAIX<sub>2</sub>** and **AZB-I-Control**)

## 3.2 Cell experiments

### 3.2.1 Media for cell culture and chemical reagents for cell experiments

All media and chemical reagents for all cell experiments were purchased from commercial companies which are listed in Table 3.3.

**Table 3.3** Media for cell cultures and chemical reagents for cell experiments.

Chemicals	Supplier
Dulbecco's Modified Eagle Medium (DMEM)	Gibco
Kaighn's Modification of Ham's F-12 (F-12K)	ATCC
Roswell Park Memorial Institute (RPMI)	Gibco
Fetal Bovine Serum (FBS)	Hyclone
Penicillin Streptomycin (P/S)	Corning
Hoechst 33342	Thermo Fisher Scientific
Acetazolamide	Tokyo Chemical Industry
MitoTracker™ Green FM	Thermo Fisher Scientific
LysoTracker™ Green DND-26	Thermo Fisher Scientific
C6-NBD Ceramide (Golgi tracker)	Avanti Polar Lipids
ER-Tracker™ Green (BODIPY™ FL Glibenclamide)	Thermo Fisher Scientific
Methylthiazolyldiphenyl-tetrazolium bromide (MTT)	Sigma-Aldrich
Calcein AM	Thermo Fisher Scientific
Propidium iodide (PI)	Thermo Fisher Scientific
2'-7'dichlorofluorescein diacetate (DCFH-DA)	Sigma-Aldrich

### 3.2.2 Cell culture

For human cell lines, CAIX expression in MDA-MB-231 (human breast cancer) is significantly higher than in other cell lines, including MCF-7 (human breast cancer), HeLa (human cervical cancer), A549 (human lung cancer), and HEK-293 (human embryonic kidney) lines. Therefore, those cell lines were analyzed for different

endogenous CAIX expression levels. MDA-MB-231, MCF-7, HeLa, and Hek293 were cultured in Dulbecco's Modified Eagle's Media (DMEM) and A549 was cultured in F-12K Medium. For murine cell lines, 4T1 (murine mammary carcinoma) is higher CAIX expression than 67NR (mouse breast cancer). Two murine cell lines were cultured in RPMI media. All cell lines were cultured on 75 cm<sup>3</sup> cell culture flasks (NEST) supplemented with 10% Fetal Bovine Serum (FBS) and 1% Penicillin Streptomycin (P/S) under a humidified 95% air, 5% CO<sub>2</sub> atmosphere at 37 °C.

### 3.2.3 Time-dependent cellular uptake in human cell lines

All human cell lines (MDA-MB-231, MCF-7, HeLa, A549, and Hek293) were seeded on a sterile 8-well (Chamber Slide x /Cover RS Glass Slides, LabTek II) at 1 x 10<sup>4</sup> cells/well and incubated at 37 °C for 24 h. After that, the cells were incubated with 5 µM of **AZB-I-CAIX<sub>2</sub>** (all cells) and **AZB-I-Control** (MDA-MB-231 and MCF-7) for 0, 1, 3, 6, and 24 h. Then, the cells were washed three times with 0.01 M of PBS buffer (pH 7.4) and treated with media containing 1.0 µM Hoechst 33342 (DNA fluorescent staining) for 10 min. The cells were visualized under 60X oil immersion objective lens by Laser Scanning Confocal Microscope (Nikon A1Rsi) with 561 nm laser (**AZB-I-CAIX<sub>2</sub>** and **AZB-I-Control**) and 405 nm laser (Hoechst33342). Quantitative corrected total cell fluorescence data was quantified using ImageJ and represented the mean ± SD (n = 50). Statistical analysis: One-way ANOVA followed by Tukey's analysis was used by GraphPad Prism9 software.

### 3.2.4 Co-cultured between (+) and (-) CAIX expression cell lines

Positive CAIX expression cells (MDA-MB-231) and negative CAIX expression cells (MCF-7) were seeded on 35-mm glass-bottom confocal dishes (NEST) at 2 x 10<sup>5</sup>/well in single media and incubated at 37 °C for 24 h. After that, the cells were incubated with 5 µM of **AZB-I-CAIX<sub>2</sub>** for 6 h. Then, the cells were washed three times with 0.01 M of PBS buffer (pH 7.4) and treated with media containing 1.0 µM Hoechst33342 for 10 min. The cells were visualized under 60X oil immersion objective lens by Laser Scanning Confocal Microscope (Nikon A1Rsi) with 561 nm laser (**AZB-I-CAIX<sub>2</sub>**) and 405 nm laser (Hoechst33342).

### 3.2.5 Competitive effect with CAIX ligand

Positive CAIX expression cell lines (MDA-MB-231) were seeded on a sterile 8-well (Chamber Slide x /Cover RS Glass Slides, LabTek II) at  $1 \times 10^4$  cells/well and incubated at 37 °C for 24 h. After that, the cells were incubated with 5  $\mu$ M of **AZB-I-CAIX<sub>2</sub>** and 0, 500, and 1000  $\mu$ M of acetazolamide (CAIX ligand) for 6 h. Then, the cells were washed three times with 0.01 M of PBS buffer (pH 7.4) and treated with media containing 1.0  $\mu$ M Hoechst33342 for 10 min. The cells were visualized under 60X oil immersion objective lens by Laser Scanning Confocal Microscope (Nikon A1Rsi) with 561 nm laser (**AZB-I-CAIX<sub>2</sub>**) and 405 nm laser (Hoechst33342). Quantitative corrected total cell fluorescence data was quantified using ImageJ and represented the mean  $\pm$  SD (n = 50). Statistical analysis: t-test followed by Tukey's analysis was used by GraphPad Prism9 software.

### 3.2.6 Colocalization study

Positive CAIX expression cell lines (MDA-MB-231) were seeded on a sterile 8-well (Chamber Slide x /Cover RS Glass Slides, LabTek II) at  $1 \times 10^4$  cells/well and incubated at 37 °C for 24 h. After that, the cells were incubated with 5  $\mu$ M of **AZB-I-CAIX<sub>2</sub>** for 6 h. Then, the cells were washed three times with 0.01 M of PBS buffer (pH 7.4) and treated with 1.0  $\mu$ M Hoechst33342 in media containing MitoTracker™ Green FM, LysoTracker™ Green DND-26, C6-NBD Ceramide (Golgi tracker), and ER-Tracker™ Green (BODIPY™ FL Glibenclamide) for 20 min. The cells were visualized under 60X oil immersion objective lens by Laser Scanning Confocal Microscope (Nikon A1Rsi) with 641 nm laser (**AZB-I-CAIX<sub>2</sub>**), 488 nm laser (Mitotracker, LysoTracker, Golgitracker, and ERtracker), and 405 nm laser (Hoechst33342). Pearson's correlation coefficient for colocalization of **AZB-I-CAIX<sub>2</sub>** and organelles trackers were obtained from ImageJ for 30 each organelle.

### 3.2.7 Light-induced cell cytotoxicity assay in human cell lines

All human cell lines (MDA-MB-231, MCF-7, HeLa, A549, and Hek293) were seeded in a 96-well cell culture plate at approximately  $7 \times 10^3$  cells/well for 24 h. After that, the cells were incubated with 0, 0.125, 0.25, 0.5, 1, 2, 5, and 10  $\mu$ M of **AZB-**

**I-CAIX<sub>2</sub>** (all cells) and **AZB-I-Control** (MDA-MB-231 and MCF-7) for 6 h. After incubation, the cells were washed with 0.01 M of PBS pH 7.4 (3 times) before being irradiated by a red LED lamp (660 nm, power density of 8.7 mW cm<sup>-2</sup>) for 0, 5, 10, and 15 min, and then re-incubated in dark for another 24 h. Then, the cells were added with 0.5 mg mL<sup>-1</sup>/well of MTT reagent (Methylthiazolyldiphenyl-tetrazolium bromide) in 0.01 M PBS (pH 7.4) solution for 2.5 h. After the removal of the MTT reagent, the formazan product was dissolved by adding DMSO. The cell cytotoxicity was detected through UV-vis absorption of formazan at wavelength 560 nm using a microplate reader (BMG Labtech/SPECTROstar Nano). IC<sub>50</sub> values of cell viability were evaluated by GrapPad Prism9 software. Statistical analysis: One-way ANOVA followed by Tukey's analysis was used by GrapPad Prism9 software.

### 3.2.8 Live/Dead staining

Positive CAIX expression cells (MDA-MB-231) were seeded on a 6-well cell culture plate at 2 × 10<sup>5</sup>/well and incubated at 37 °C for 24 h. After that, the cells were incubated with 0.5 μM of **AZB-I-CAIX<sub>2</sub>** for 6 h. Then, the cells were washed three times with 0.01 M of PBS buffer (pH 7.4) After incubation, the cells were irradiated by a red LED lamp (660 nm, power density of 8.7 mW cm<sup>-2</sup>) for 5 min before re-incubation for another 24 h in dark. Thereafter, the cells were stained with 4 μM calcein AM and propidium iodide (PI) for 5 min, and then imaged on a Fluorescence microscope (BioRad/Zoe) using λ<sub>ex</sub> = 490 nm and λ<sub>em</sub> = 515 nm for calcein AM and λ<sub>ex</sub> = 535 nm and λ<sub>em</sub> = 615 nm for PI.

### 3.2.9 Intracellular Singlet Oxygen Generation

A positive CAIX expression cell line (MDA-MB-231) was seeded on a sterile 8-well (Chamber Slide x /Cover RS Glass Slides, LabTek II) at 1 × 10<sup>4</sup> cells/well and incubated at 37 °C for 24 h. After that, the cells were incubated with 0.125 and 0.25 μM of **AZB-I-CAIX<sub>2</sub>** for 6 h. Then, the cells were washed three times with 0.01 M of PBS buffer (pH 7.4). Thereafter, 20 μM of 2,7-dichloro-dihydro-fluorescein diacetate (DCFH-DA, reactive oxygen species probe) was incubated in the cells for 1 h. The cells were washed three times with 0.01 M of PBS buffer (pH 7.4) and irradiated with a red

LED lamp (660 nm, power density of  $8.7 \text{ mW cm}^{-2}$ ) for 10 min. Before imaging, the cells were treated with media containing  $1.0 \mu\text{M}$  Hoechst33342 for 10 min. The cells were visualized under 60X oil immersion objective lens by Laser Scanning Confocal Microscope (Nikon A1Rsi) with 561 nm laser (**AZB-I-CAIX<sub>2</sub>**) and 405 nm laser (Hoechst33342).

### 3.2.10 Murine cell internalization under hypoxia condition

Murine cell lines (4T1 and 67NR) were seeded on a sterile 8-well (Chamber Slide x /Cover RS Glass Slides, LabTek II) at  $1 \times 10^4$  cells/well and incubated at  $37 \text{ }^\circ\text{C}$  for 24 h. After that, the cells were incubated under normoxia (humidified 95% air, 5%  $\text{CO}_2$  atmosphere) and hypoxia (5%  $\text{pO}_2$ ) conditions for 12 h. Then, the cells were treated with  $5 \mu\text{M}$  of **AZB-I-CAIX<sub>2</sub>** in DMEM for 0, 1, 3, and 6 h. Thereafter, the cells were washed three times with 0.01 M PBS buffer (pH 7.4) and treated with media containing  $1.0 \mu\text{M}$  Hoechst33342 for 10 min. Confocal images were visualized under 60X oil immersion objective lens by Laser Scanning Confocal Microscope (Nikon A1Rsi) with 561 nm laser (**AZB-I-CAIX<sub>2</sub>**) and 405 nm laser (Hoechst33342).

### 3.2.11 Murine cell cytotoxicity assay under hypoxia condition

4T1 has seeded on a 96-well plate approximately  $7 \times 10^3$  cells per well and incubated in complete media for 24 h. Thereafter, the cells were incubated under normoxic (humidified 95% air, 5%  $\text{CO}_2$  atmosphere) and hypoxic (5%  $\text{pO}_2$ ) conditions at  $37 \text{ }^\circ\text{C}$  for 12 h before being treated with 0, 0.125, 0.25, 0.5, 5, 10  $\mu\text{M}$  of **AZB-I-CAIX<sub>2</sub>** for 6 h under the hypoxia. After incubation, the cells were washed twice with 0.01 M of PBS buffer (pH 7.4) to remove excess probes and the complete media was added before the cells were irradiated with a red LED lamp ( $660 \text{ nm}$ , power density of  $8.7 \text{ mW cm}^{-2}$ ) for 0, 5, 10, and 15 min and continued culturing for 24 h under the hypoxia. Cell viability was detected by  $0.5 \text{ mg mL}^{-1}$ /well of methylthiazolyldiphenyl-tetrazolium bromide (MTT) reagent in 0.01 M of PBS buffer (pH 7.4) solution for 2.5 h incubation time. After media removal, DMSO was added to dissolve the formazan product and detected through UV-vis absorption of formazan at wavelength  $560 \text{ nm}$  (BMG Labtech/SPECTROstar Nano microplate reader).  $\text{IC}_{50}$  values of cell viability were

evaluated by GrapPad Prism9 software. Statistical analysis: t-test followed using GrapPad Prism9 software.



## CHAPTER IV

### RESULTS AND DISCUSSION

#### 4.1 Synthesis and characterization of AZB-I-CAIX<sub>2</sub> and AZB-I-Control

##### 4.1.1 Synthesis of AZB-I-CAIX<sub>2</sub> and AZB-I-Control

AZB-I-CAIX<sub>2</sub> and AZB-I-Control were synthesized according to scheme 1. The reaction started from the S<sub>N</sub>2 reaction between azido-PEG that was synthesized according to our previous paper (Pewklang et al., 2019) and succinic anhydride to form an ester bond and leave a free terminal carboxylic acid and azide groups linked by polyethylene glycol (PEG) (**1**). After then, the amide coupling of (**1**) and hydrolyzed acetazolamide (More et al., 2018) gave the linker containing CAIX ligand (**2**). This linker can provide a biocompatibility part on the molecules and provide more access of the ligand to the active site of CAIX. Aza-BODIPY containing two terminals of the alkyne (**3**) was obtained from an amide coupling reaction of two equivalent of 5-hexynoic acid and aza-BODIPY (AZB-NH<sub>2</sub>) that was synthesized following the reference (Kamkaew and Burgess, 2015). AZB-I-CAIX<sub>2</sub> was synthesized via the azide-alkyne Huisgen cycloaddition between two acetazolamide-linkage moieties (**2**) and terminal alkynes of mono-iodo-aza-BODIPY derivative (**4**), prepared by an electrophilic aromatic substitution reaction between (**3**) and *N*-iodosuccinimide (NIS). AZB-I-control was produced by a similar reaction condition, except for the linker without acetazolamide (**1**) was used. In general, when heavy atoms are present in the dye structure, *i.e.* aza-BODIPY, the fluorescent emission is usually quenched due to an increase in the rate of triplet formation that affects orbital spin interaction, so-called heavy atom effect (De Simone, Mazzone, Pirillo, Russo, and Sicilia, 2017) However, this feature increases singlet oxygen generation that is beneficial for PDT (Kamkaew et al., 2013). As a result, in this design, aza-BODIPY was mono iodinated to guarantee that the fluorescent signal is preserved while the singlet oxygen generation is sufficient for PDT efficiency.

#### 4.1.2 Characterization of AZB-I-CAIX<sub>2</sub> and AZB-I-Control by NMR and Mass spectrometry

All compounds were confirmed chemical structure by <sup>1</sup>H, <sup>13</sup>C, and <sup>19</sup>F NMR and interpreted in a chemical shift ( $\delta$ , ppm), resonance splitting, coupling constants ( $J$ ), and a number of protons. Moreover, the compounds have confirmed their mass-to-charge ratio ( $m/z$ ) to see the exact molecular weight by high-resolution Electrospray Ionization Time of Flight mass spectrometry (high-resolution ESI-TOF-MS). The results from both techniques are corresponding to ensure the chemical structure of **AZB-I-CAIX<sub>2</sub>** and **AZB-I-Control**. All spectra are shown in Figure 4.1-4.20.

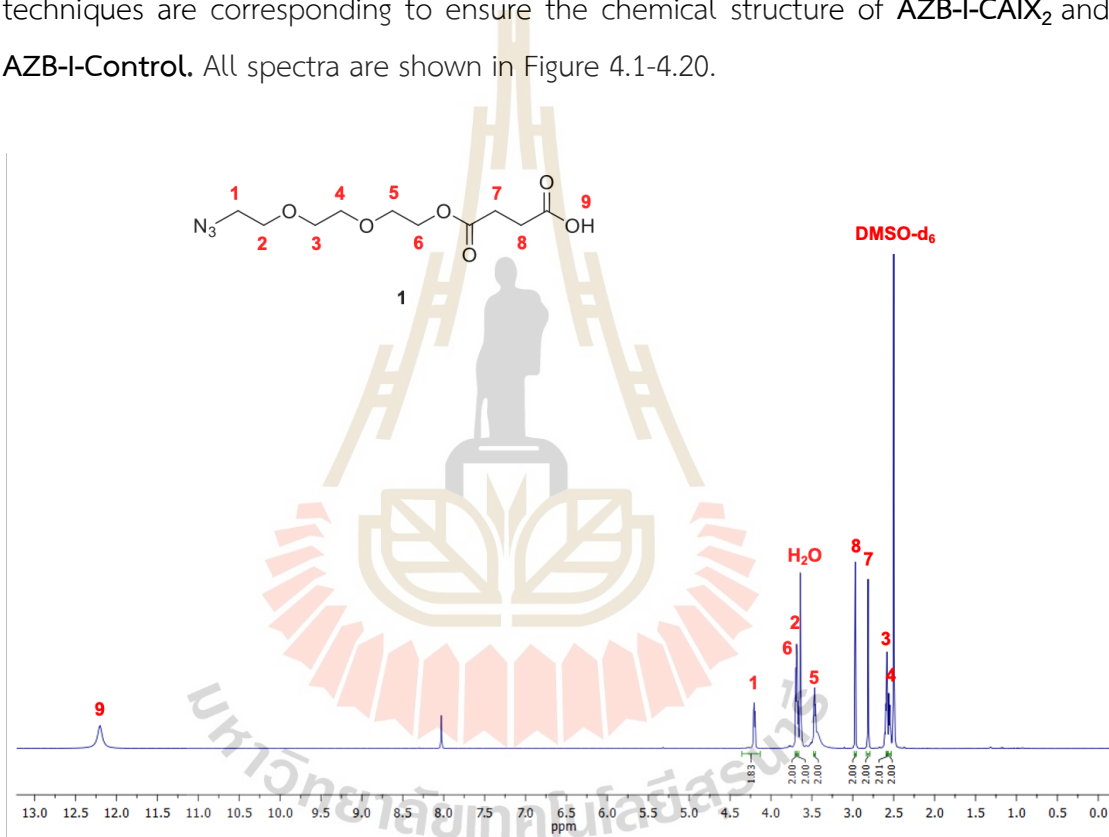
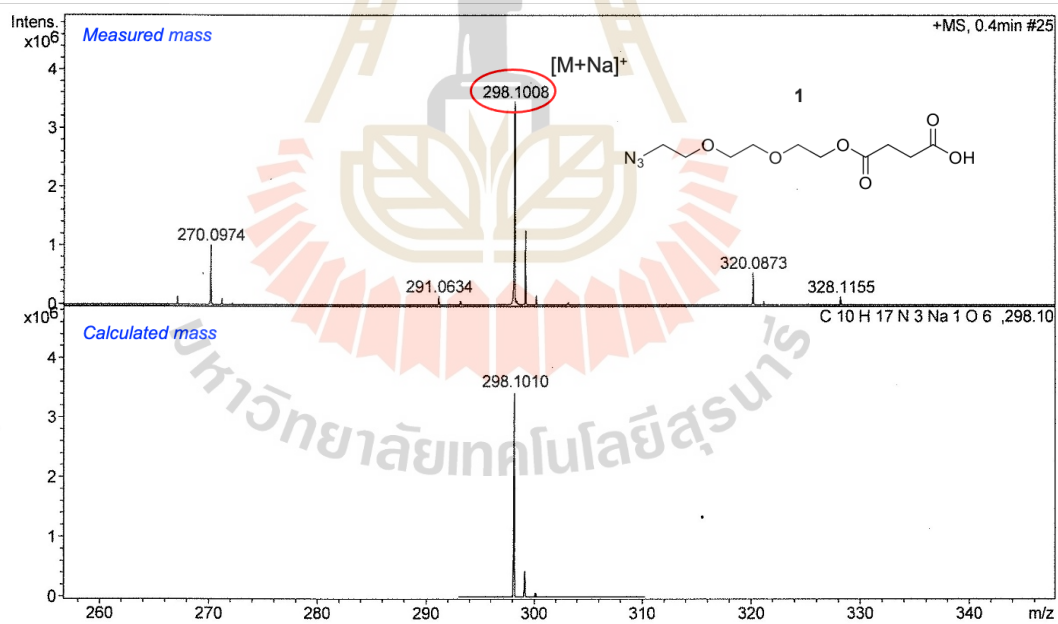
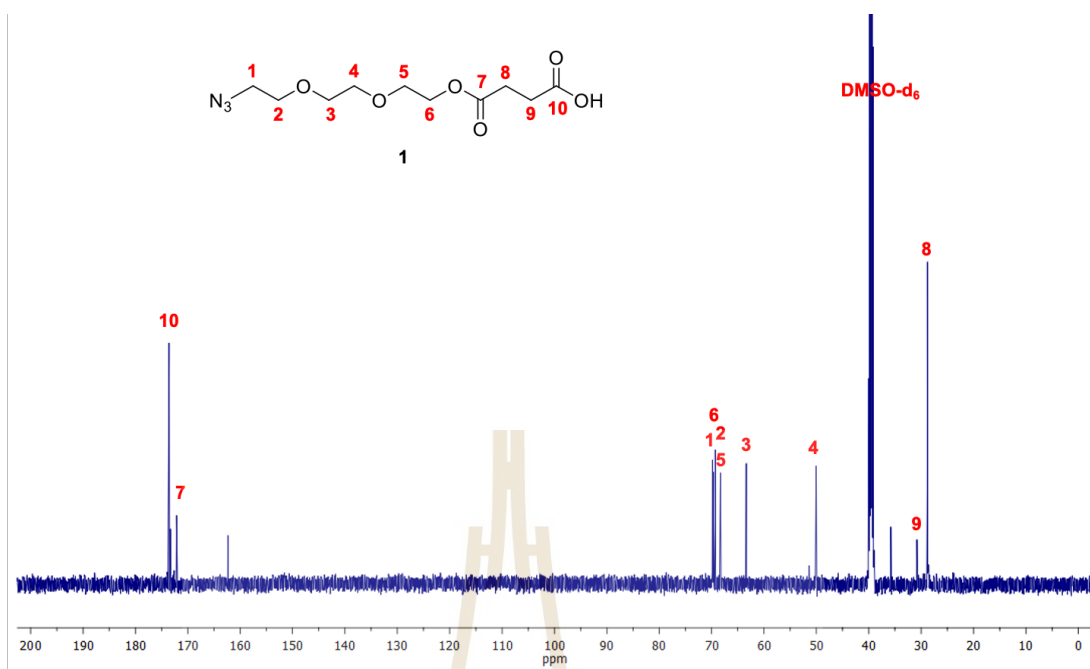
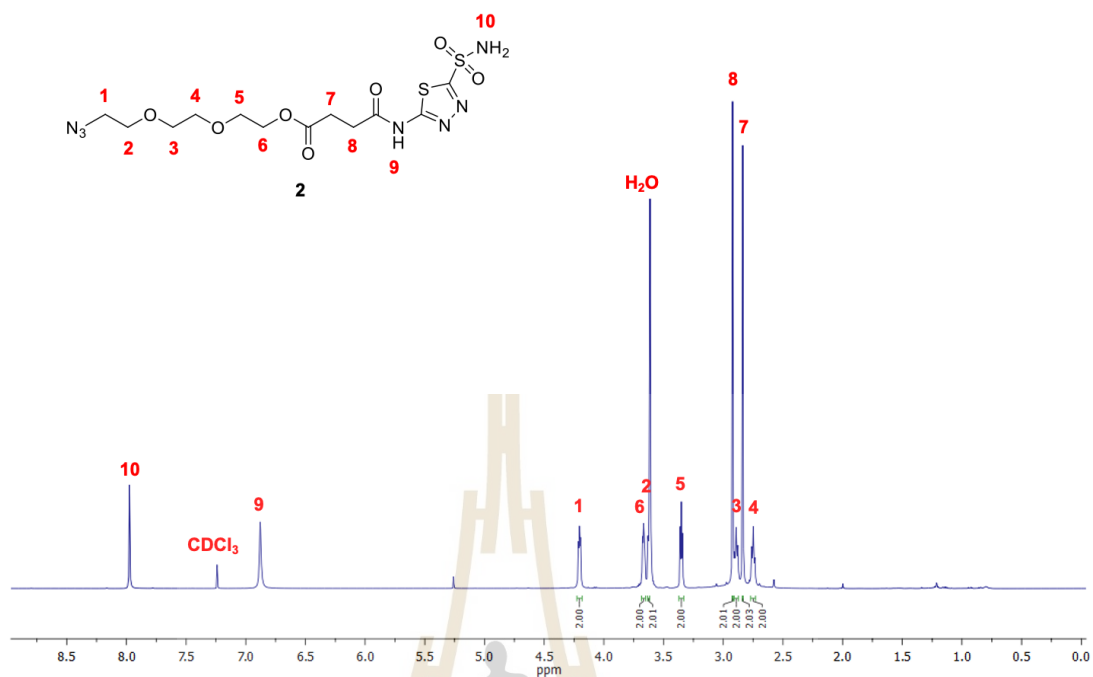
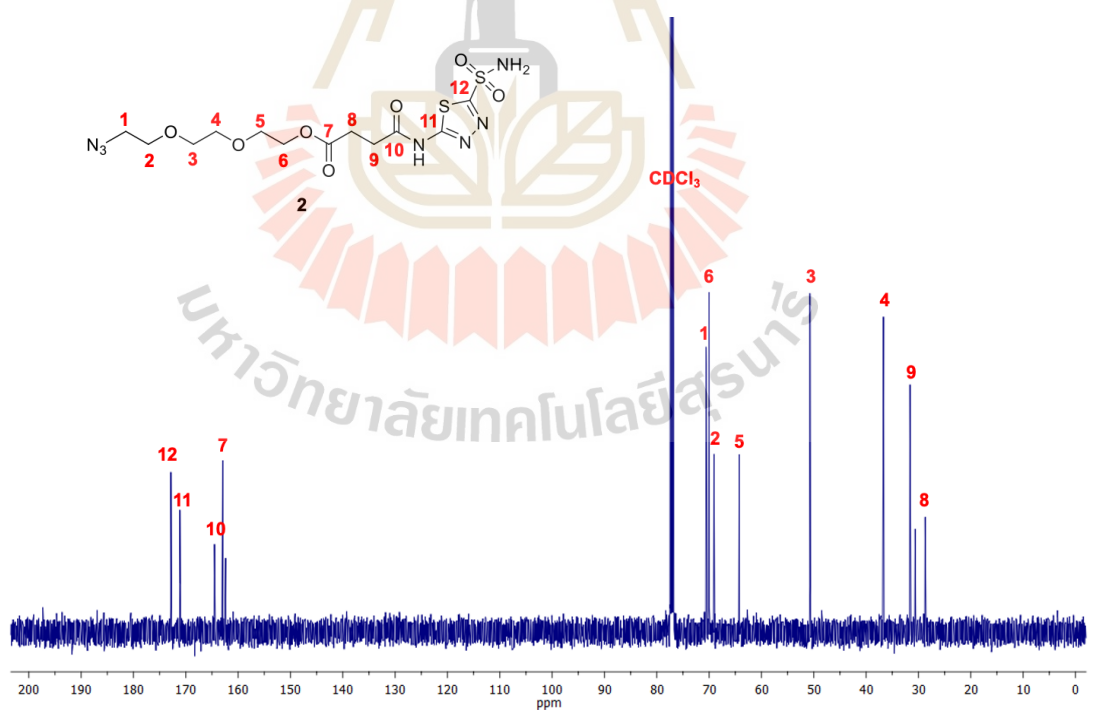
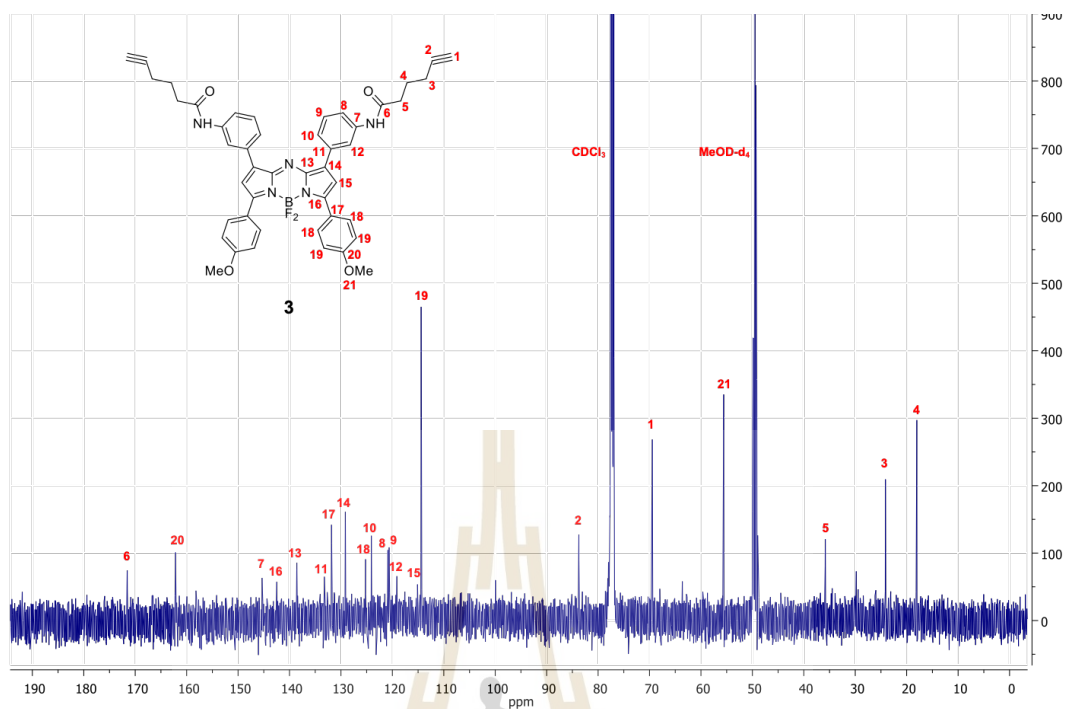
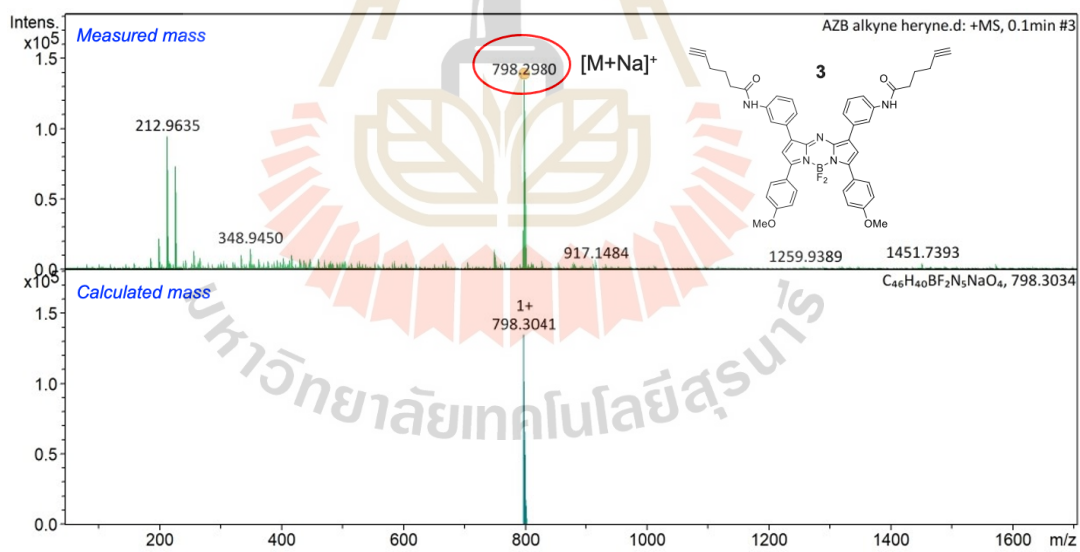


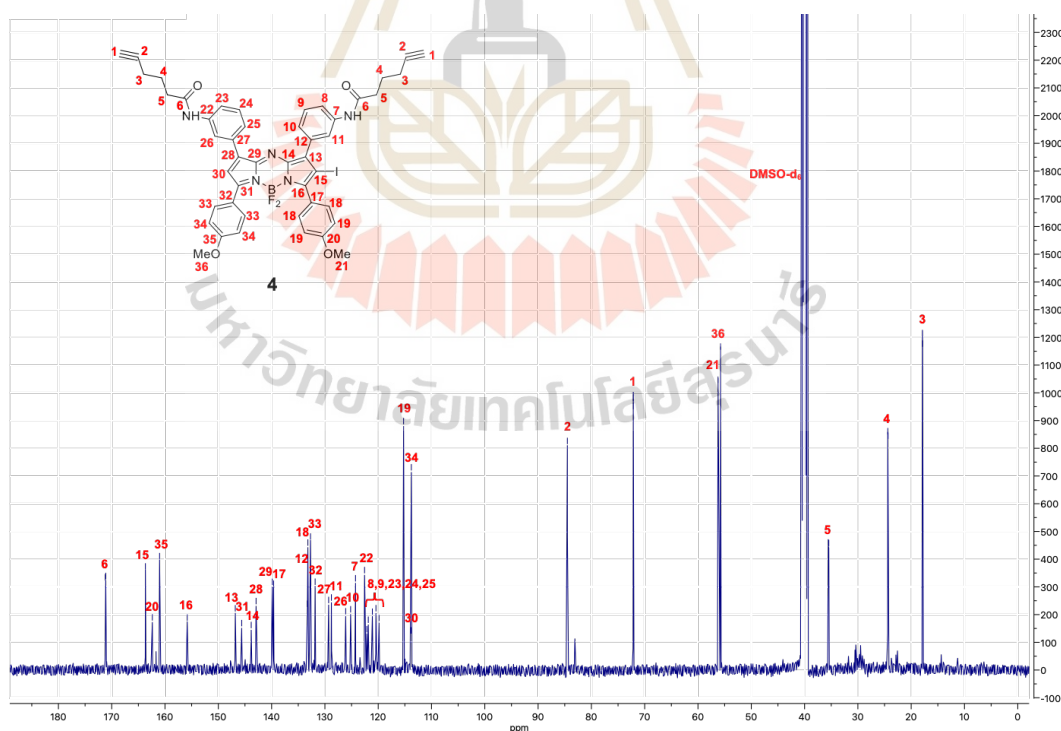
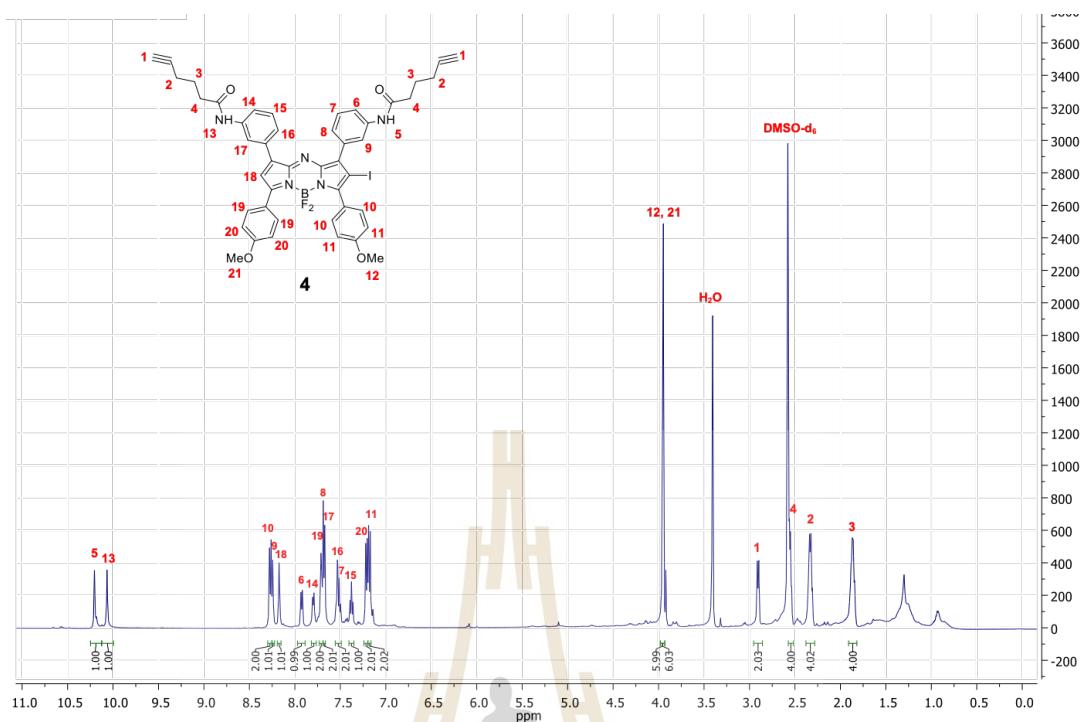
Figure 4.1 <sup>1</sup>H NMR of compound 1

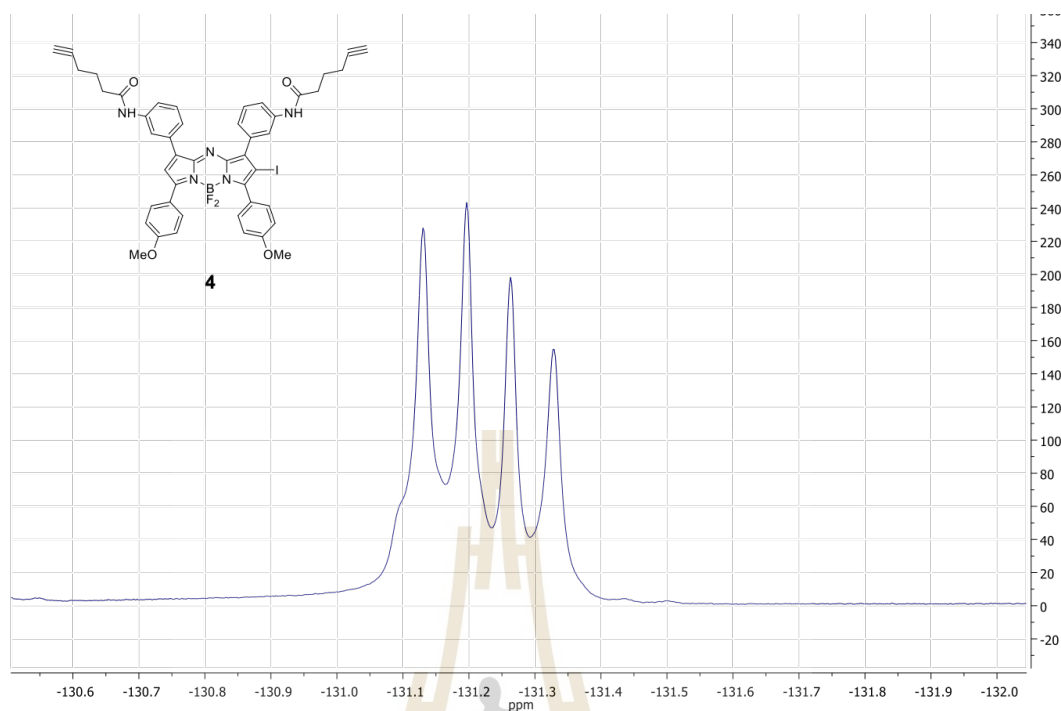
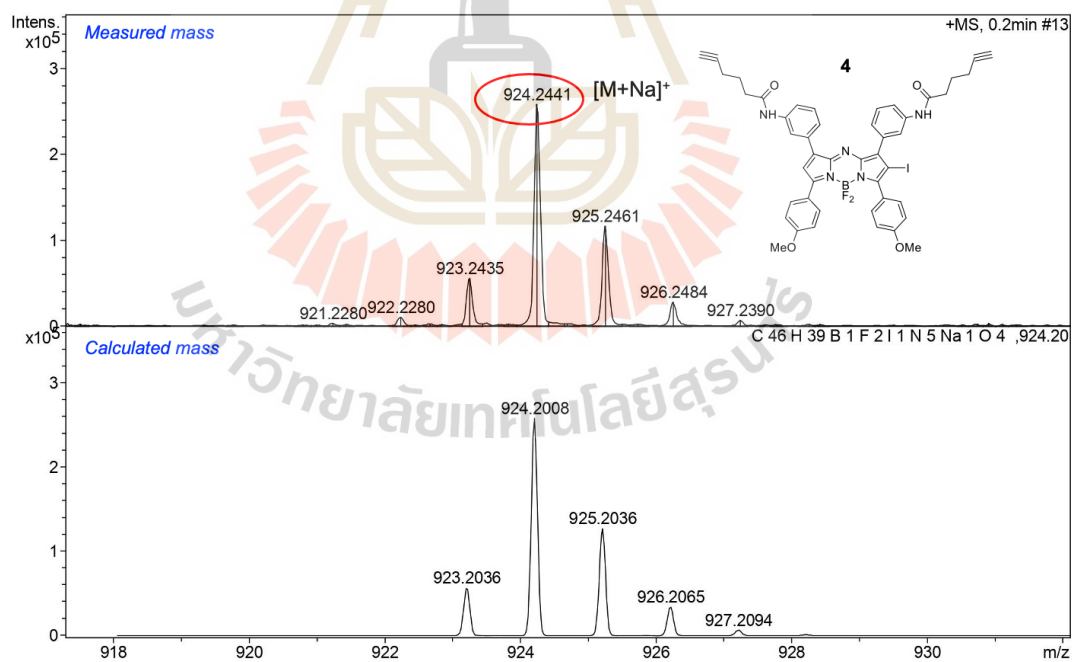


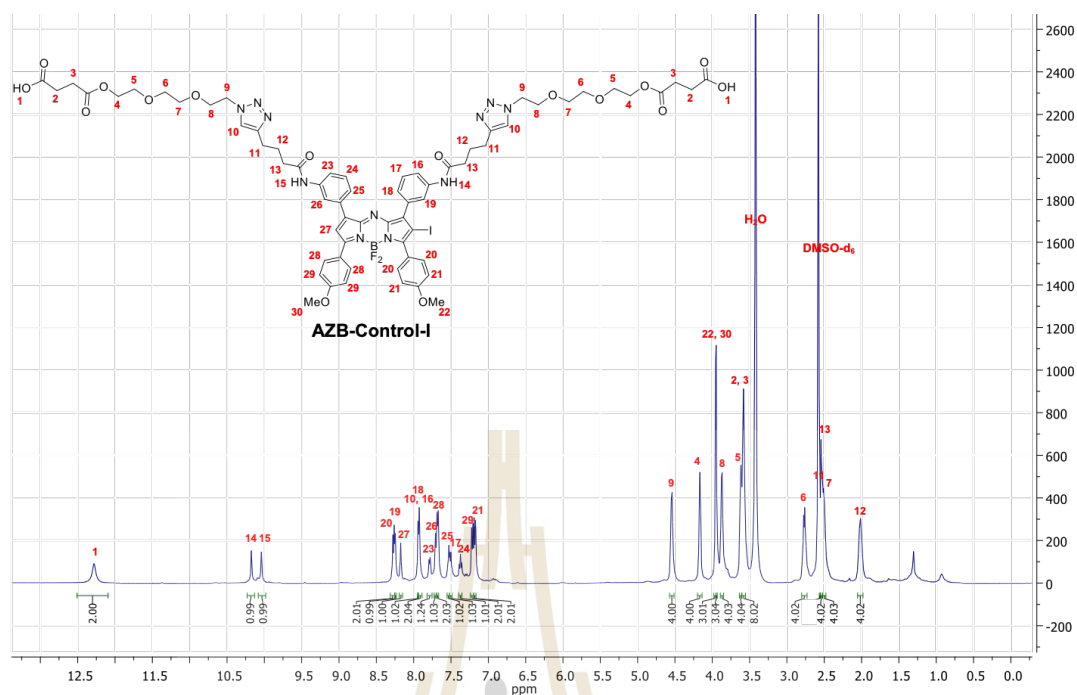
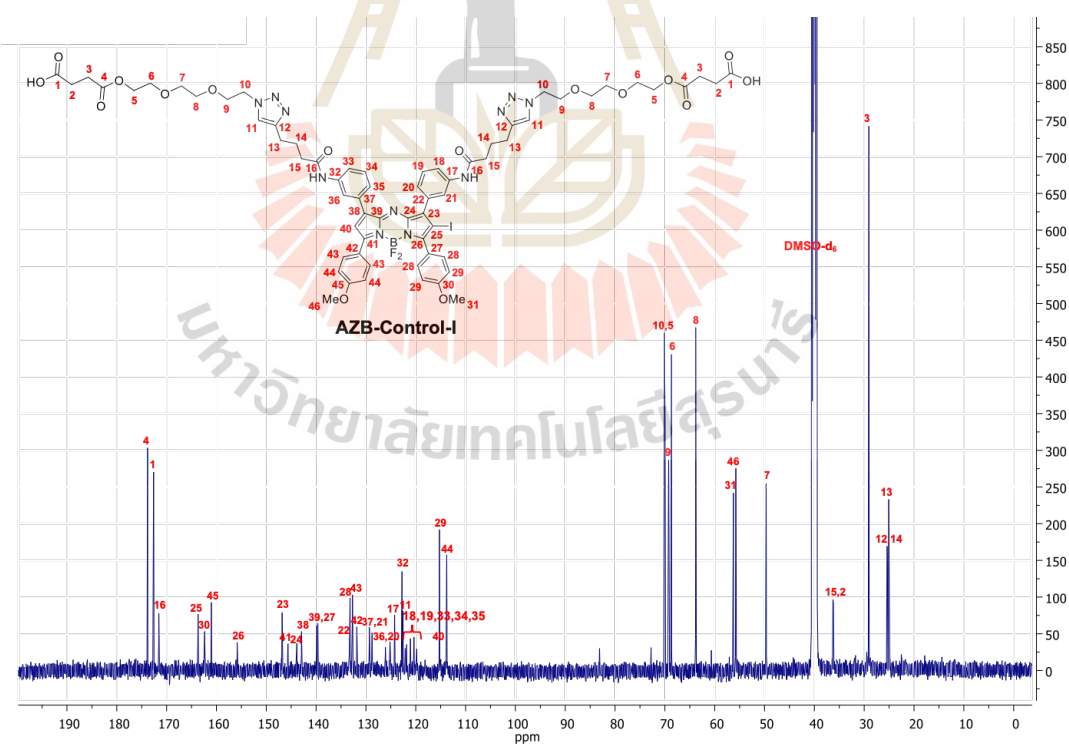
Figure 4.4 <sup>1</sup>H NMR of compound 2Figure 4.5 <sup>13</sup>C NMR of compound 2

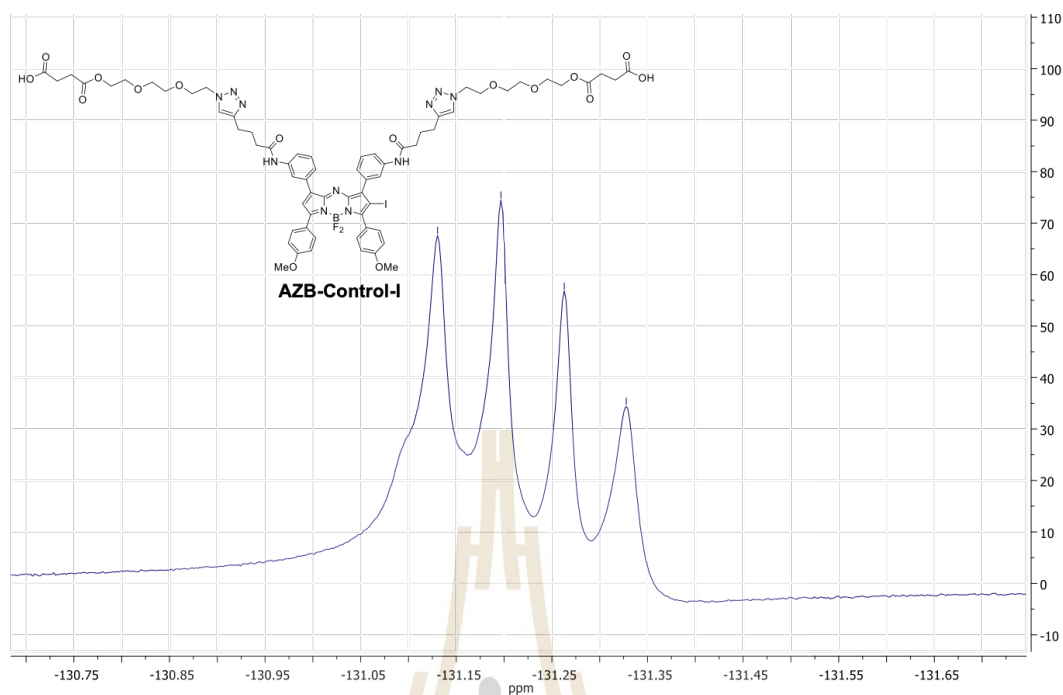
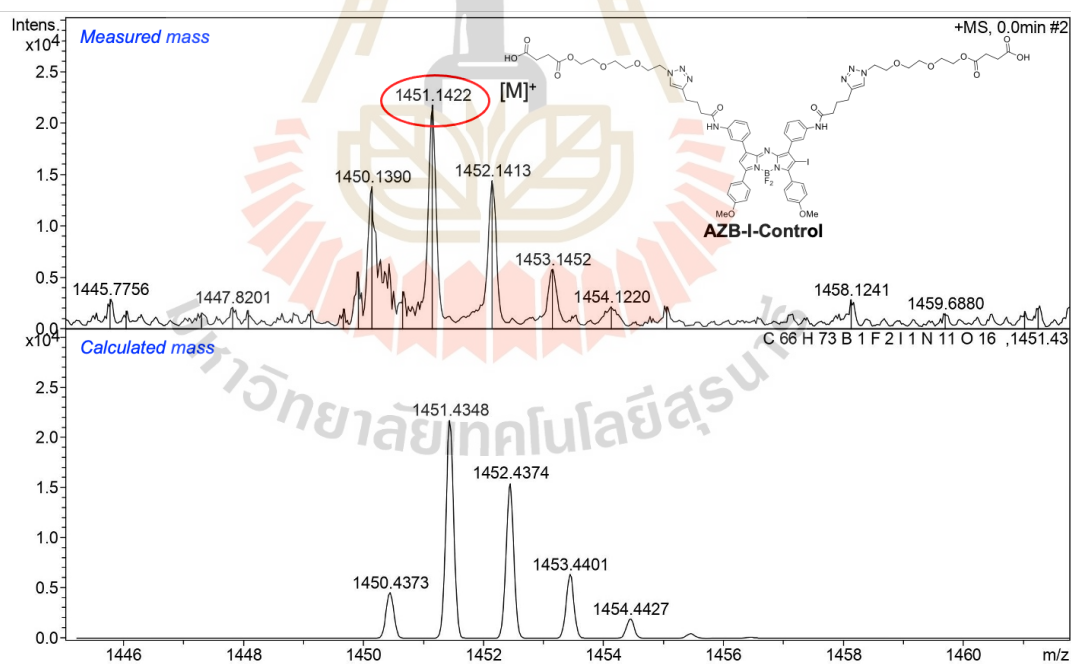


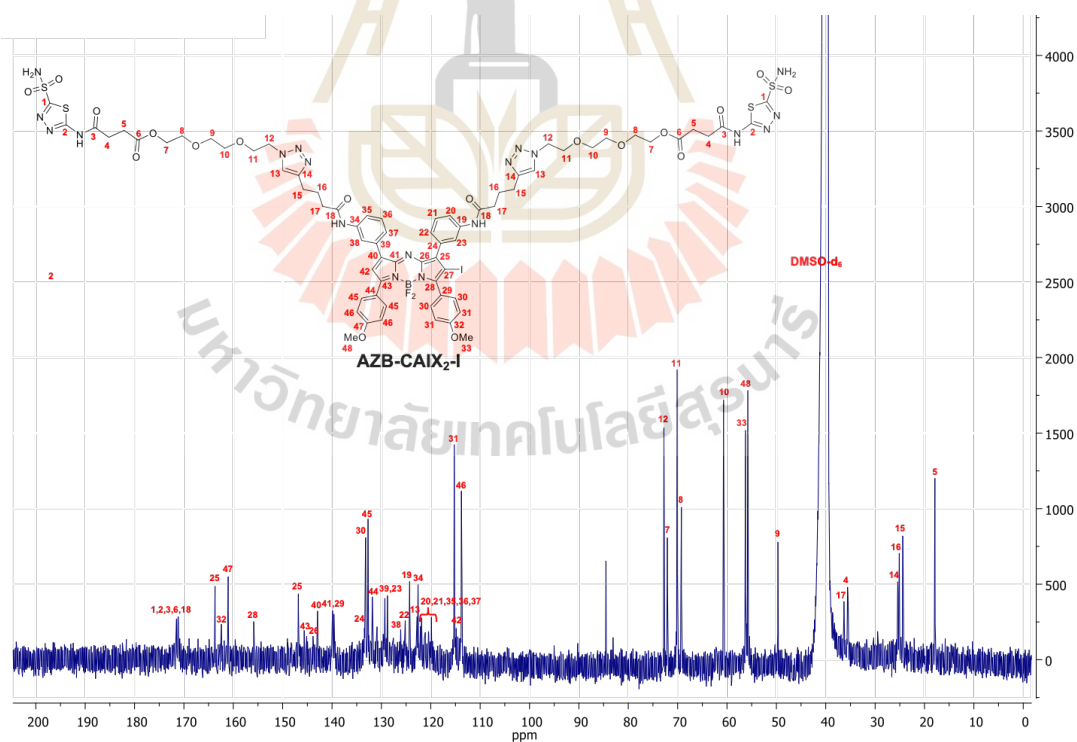
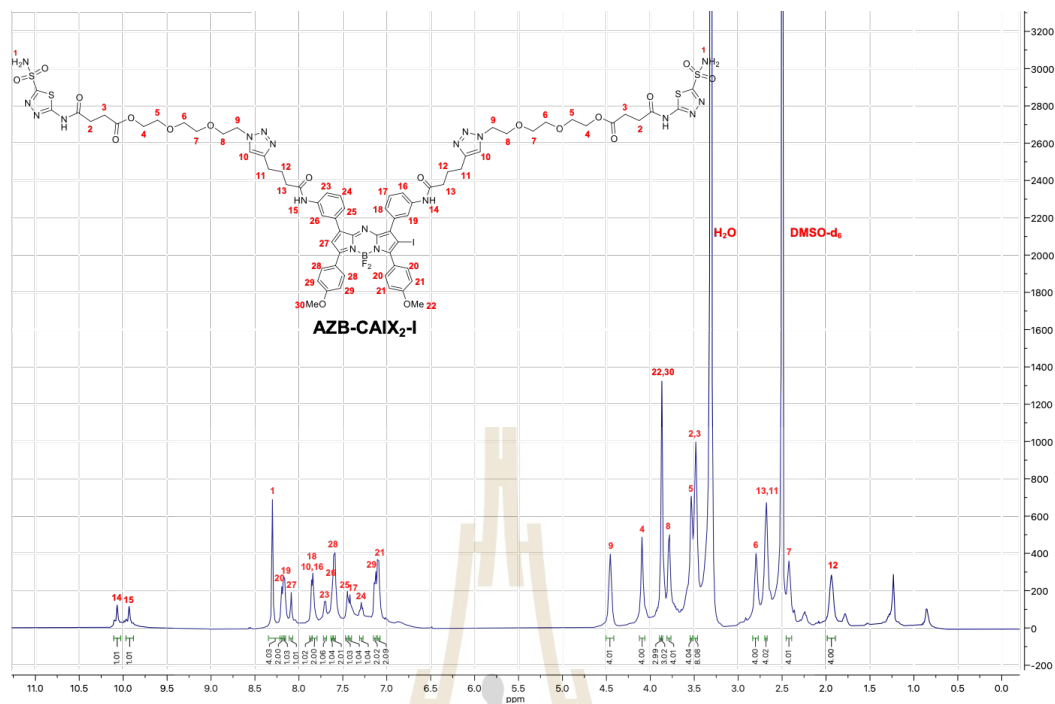
Figure 4.8  $^{13}\text{C}$  NMR of compound 3Figure 4.9 High-resolution ESI<sup>+</sup> MS of compound 3



Figure 4.12  $^{19}\text{F}$  NMR of compound 4Figure 4.13 High-resolution ESI<sup>+</sup> MS of compound 4

Figure 4.14  $^1\text{H}$  NMR of compound AZB-Control-IFigure 4.15  $^{13}\text{C}$  NMR of compound AZB-Control-I

Figure 4.16  $^{19}\text{F}$  NMR of compound AZB-Control-IFigure 4.17 High-resolution ESI<sup>+</sup> MS of compound AZB-Control-I



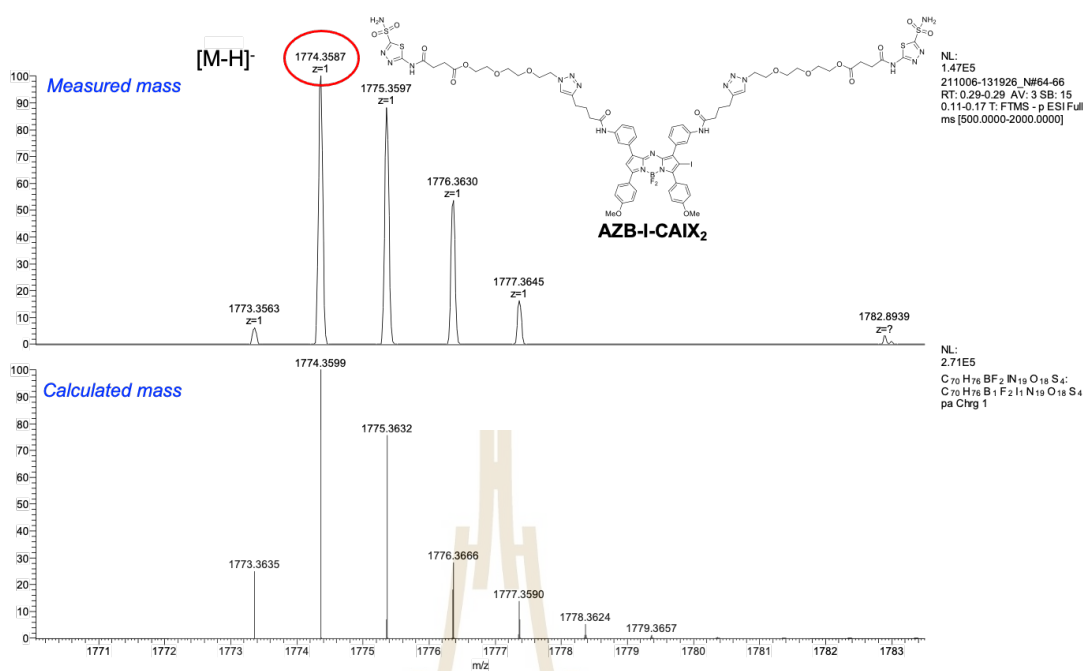


Figure 4.20 High-resolution ESI<sup>-</sup> MS of compound AZB-CAIX<sub>2</sub>-I

#### 4.1.3 Photophysical properties and fluorescence quantum yields of AZB-I-CAIX<sub>2</sub> and AZB-I-Control

The photophysical properties of AZB-I-CAIX<sub>2</sub> and AZB-I-control were investigated by UV-VIS-NIR and fluorescence spectrophotometry in different solvents, chloroform, DMSO, methanol, and phosphate buffer saline (PBS), (Figure 4.21A-B). According to the absorbance spectra, AZB-I-CAIX<sub>2</sub> and AZB-I-control show similar absorption maxima from 675 to 686 nm. The emission maxima are around the NIR region in a range of 713-728 nm in the tested solvents. The fluorescence quantum yield calculation from the photophysical properties, AZB-I-CAIX<sub>2</sub> has a fluorescent quantum yield ranging from 0.02-0.09 which is close to AZB-I-control (0.09-0.14), as shown in Table 4.1. In the literature (Treekoon et al., 2021), Kamkaew's lab reported about AZB-Glc and AZB-Glc-I that contained methoxy (OMe) and amide group on meta-position substituted aza-BODIPY. Their aza-BODIPY structure is identical to AZB-I-CAIX<sub>2</sub> and AZB-I-control. While AZB-Glc has a fluorescence quantum yield of 0.40, 0.62, and 0.45 in DMSO, MeOH, and PBS 3% tween80 respectively but AZB-Glc-I contains two iodine atoms on aza-BODIPY showed very less fluorescence quantum yield. In comparison, AZB-I-CAIX<sub>2</sub> and AZB-I-control have less fluorescence quantum yields

than AZB-Glc (no iodine on its structure) around 4 times, but they still show some fluorescence signal while AZB-Glc-I (containing two iodine atoms on its structure) cannot show any fluorescence signal, because of heavy atom effect from one iodine atom on the aza-BODIPY structure of **AZB-I-CAIX<sub>2</sub>** and **AZB-I-control**. These photophysical properties of **AZB-I-CAIX<sub>2</sub>** and **AZB-I-control** can be beneficial for fluorescence images in deep tissues.

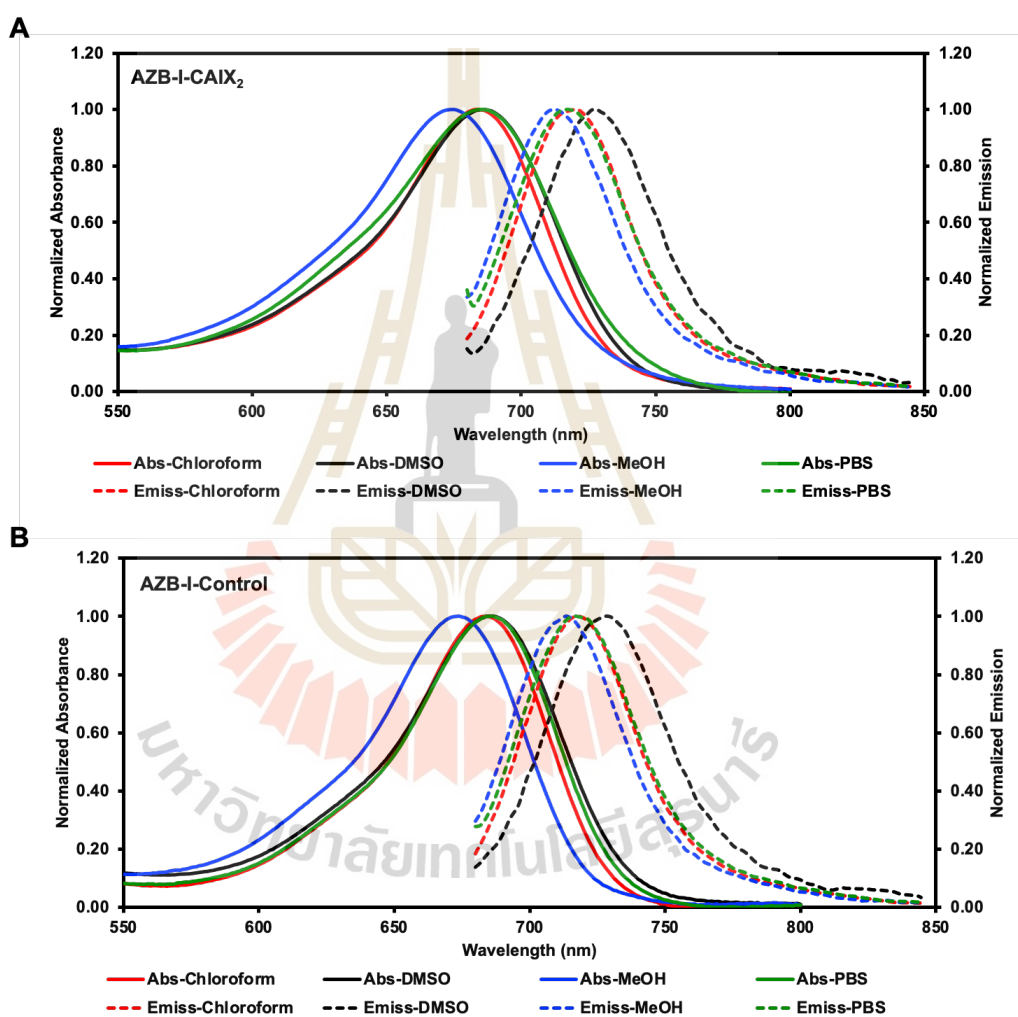


Figure 4.21 Normalized Vis-NIR absorption and emission spectra of **AZB-I-CAIX<sub>2</sub>** and **AZB-I-Control** (1  $\mu$ M) in various solvents. The fluorescence spectra were reported of A) **AZB-I-CAIX<sub>2</sub>** and B) **AZB-I-Control** at 670 nm excitation wavelength.

**Table 4.1** Photophysical properties of **AZB-I-CAIX<sub>2</sub>** and **AZB-I-control** (1  $\mu$ M).

Compound	Solvent	$\lambda_{\max}$ (nm)	$\epsilon$ (M <sup>-1</sup> cm <sup>-1</sup> )	$\lambda_{\text{em}}^{\text{a}}$ (nm)	$\Delta\lambda$ (nm)	$\Phi_{\text{f}}^{\text{b}}$
<b>AZB-I-CAIX<sub>2</sub></b>	CHCl <sub>3</sub>	683	11.2 × 10 <sup>4</sup>	720	37	0.09
	DMSO	686	11.6 × 10 <sup>4</sup>	728	42	0.02
	MeOH	675	9.6 × 10 <sup>4</sup>	713	38	0.03
	PBS <sup>c</sup>	685	8.9 × 10 <sup>4</sup>	718	33	0.05
<b>AZB-I-Control</b>	CHCl <sub>3</sub>	683	6.0 × 10 <sup>4</sup>	720	34	0.14
	DMSO	686	6.5 × 10 <sup>4</sup>	728	42	0.04
	MeOH	675	6.6 × 10 <sup>4</sup>	714	40	0.05
	PBS <sup>c</sup>	686	6.4 × 10 <sup>4</sup>	717	31	0.09

<sup>a</sup> Samples were excited at 670 nm.

<sup>b</sup> Relative to Zn-pthalocyanine in pyridine ( $\Phi_{\text{f}} = 0.30$ ).

<sup>c</sup> Contained 3% tween80.

#### 4.1.4 Singlet oxygen quantum yields of **AZB-I-CAIX<sub>2</sub>** and **AZB-I-Control**

As the data show that **AZB-I-CAIX<sub>2</sub>** and **AZB-I-control** have low fluorescence quantum yields, this might be due to the heavy atom effect. Therefore, the singlet oxygen quantum yields of both probes were also investigated. Singlet oxygen generation efficiency of **AZB-I-CAIX<sub>2</sub>**, **AZB-I-control**, and methylene blue (standard photosensitizer) was measured using 1,3-diphenylisobenzofuran (DPBF) as singlet oxygen (<sup>1</sup>O<sub>2</sub>) scavenger. After all compounds were exposed to the light (660 nm, power density 8.7 mW cm<sup>-2</sup>), <sup>1</sup>O<sub>2</sub> was produced at initial rate in a few seconds and more <sup>1</sup>O<sub>2</sub> production with light irradiation time-dependent manner, as indicated by the decreasing DPBF absorbance at 408 nm because DPBF reacts with <sup>1</sup>O<sub>2</sub> and produces an endoperoxide via a [4+2] cycloaddition and product of 1,2-dibenzoylbenzene (DBB) resulting in the loss of an extended  $\pi$ -electron system and its characteristic spectroscopic properties (Ercin, Aribas, Tefon Aribas, Bilgihan, & Bilgihan, 2021) (Figure 4.22). Moreover, **AZB-I-CAIX<sub>2</sub>** and **AZB-I-control** could generate <sup>1</sup>O<sub>2</sub> at a faster rate

than methylene blue in DMSO solution. The calculated singlet oxygen quantum yields ( $\Phi_{\Delta}$ ) of AZB-I-CAIX<sub>2</sub> and AZB-I-control were 0.88 and 0.83, respectively, relative to methylene blue (calculated from initial rate about first ten seconds with 1 s intervals, Figure 4.23). Therefore, both probes could be good for PDT agents with moderate fluorescence imaging properties.

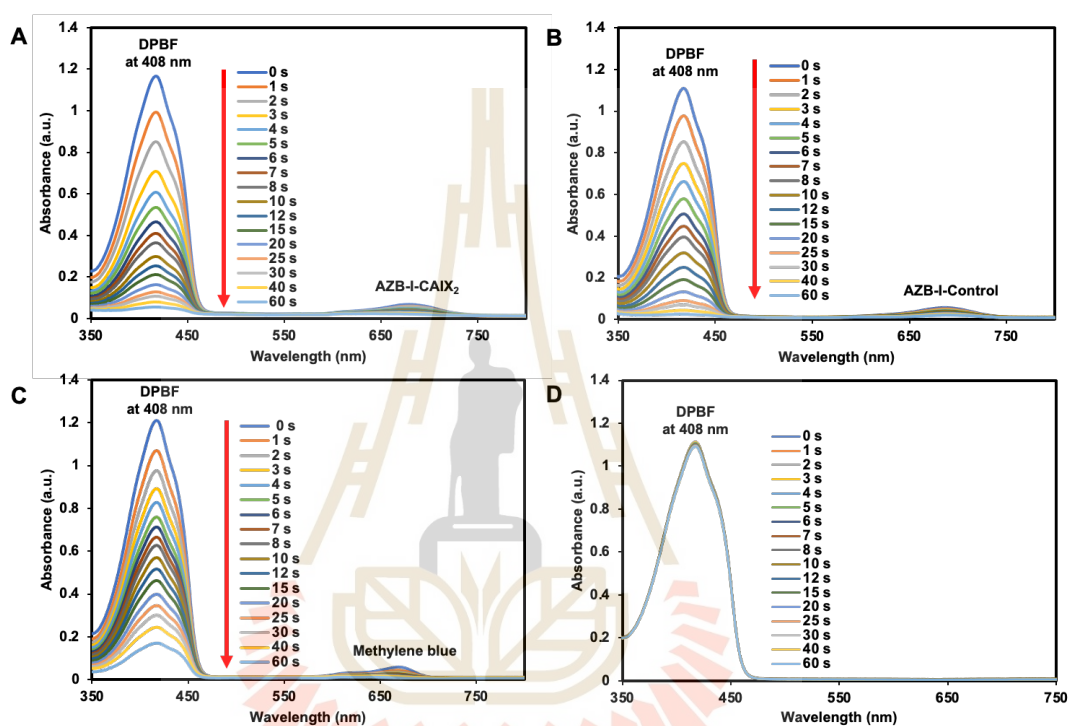


**Figure 4.22** Reduction absorbance of DPBF at 408 nm by photo-oxidation due to the singlet oxygen formation. The concentration of 0.5  $\mu$ M of **A)** AZB-I-CAIX<sub>2</sub>, **B)** AZB-I-Control, **C)** Methylene blue, and **D)** Control (DPBF only) in DMSO were exposed with lamp (660 nm, power density of 8.7 mW cm<sup>-2</sup>).

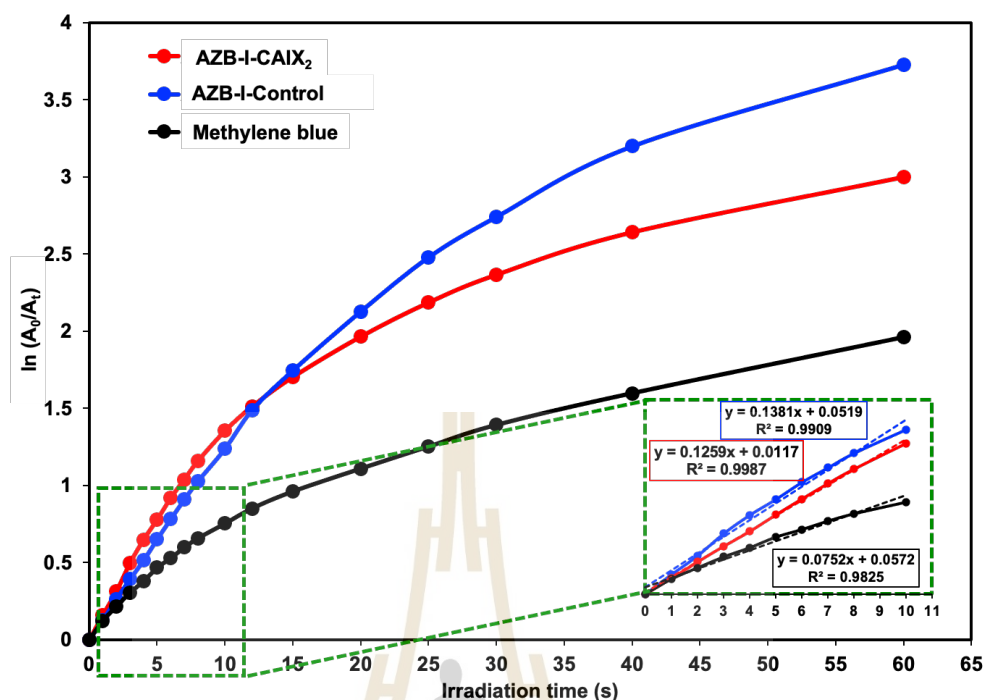
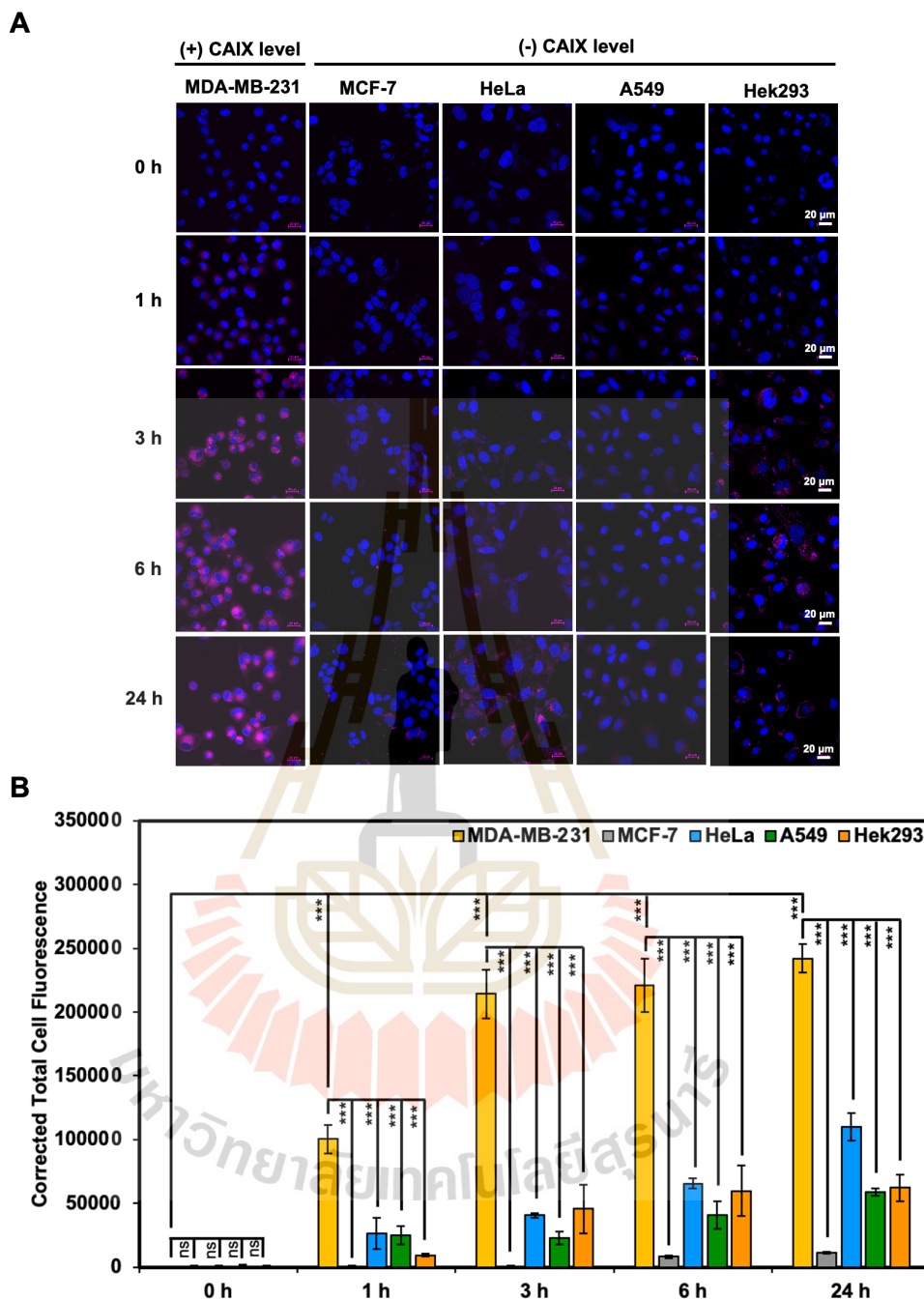


Figure 4.23 Relative DPBF absorbance changes at 408 nm of 0.5  $\mu\text{M}$  solutions of AZB-I-CAIX<sub>2</sub>, AZB-I-control, and methylene blue at the initial rate.

## 4.2 Cell experiments

### 4.2.1 Cell internalization and CAIX targeting in human cell lines

In the previous report, western blotting was used to validate the endogenous expression of CAIX in multiple cell lines (MDA-MB-231, MCF-7, HeLa, and A549). CAIX expression in MDA-MB-231 cells was considerably greater than in other cell lines (Jung et al., 2017; Li et al., 2009). To evaluate cancer cell targetability of AZB-I-CAIX<sub>2</sub>, human cancer cell lines with high expression levels of CAIX (MDA-MB-231) and low CAIX levels (MCF-7, HeLa, and A549) were selected for comparison. Moreover, human embryonic kidney cells (HEK293) were also used as normal cell control. As shown in Figure 4.24, time-dependent cellular internalization revealed that MDA-MB-231 took up AZB-I-CAIX<sub>2</sub> faster and accumulated a higher amount from 1 to 24 h incubation time, whereas low fluorescent signals were observed from other cell lines even at the longest exposure time, 24 h (Figure 4.24A). Quantitation fluorescence signals from all cell lines by ImageJ are presented in Figure 4.24B. The results indicated that AZB-I-CAIX<sub>2</sub> could be selective to CAIX expression cells.



**Figure 4.24** Time-dependent cell internalization of AZB-I-CAIX<sub>2</sub> (5  $\mu$ M) in (+) CAIX and (-) CAIX level cells. **A**) confocal image observed in excitation at 643 nm. **B**) Quantitative of the fluorescence signals by ImageJ. The data represent the mean  $\pm$  SD (n = 50) and statistical analysis by One-way ANOVA (Tukey's analysis) using GrapPad Prism9 software. P values of less than 0.05 (95% confidence interval) are considered significant (ns  $p < 0.12$  and \*\*\*  $p < 0.001$ ).

Additionally, **AZB-I-control** was produced by a similar structure to **AZB-I-CAIX<sub>2</sub>**, except for the linker without acetazolamide. When **AZB-I-control** was used in the same experiment, no observable fluorescent signals were detected from both CAIX positive (MDA-MB-231) and negative cell lines (MCF-7) (Figure 4.25). The results showed that **AZB-I-CAIX<sub>2</sub>** can select the CAIX positive cell line for cellular uptake via acetazolamide (CAIX ligand).

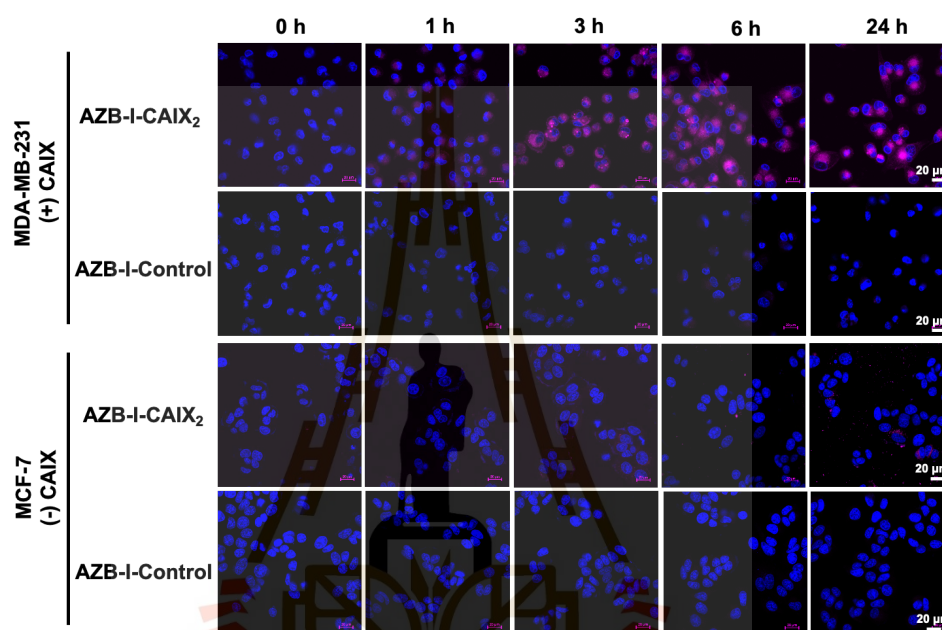


**Figure 4.25** Confocal image time-dependent cellular uptake of **AZB-I-control** compared with **AZB-I-CAIX<sub>2</sub>** (5  $\mu$ M) in MDA-MB-231 and MCF-7.

Furthermore, when two breast cancer lines, (+) CAIX (MDA-MB-231) and (-) CAIX (MCF-7) were co-cultured in the same place and then treated with **AZB-I-CAIX<sub>2</sub>**, the NIR fluorescent signals were solely observed from the positive CAIX cells (Figure 4.26). These results suggested that **AZB-I-CAIX<sub>2</sub>** is internalized cancer cells with strong selectivity for those expressing CAIX.

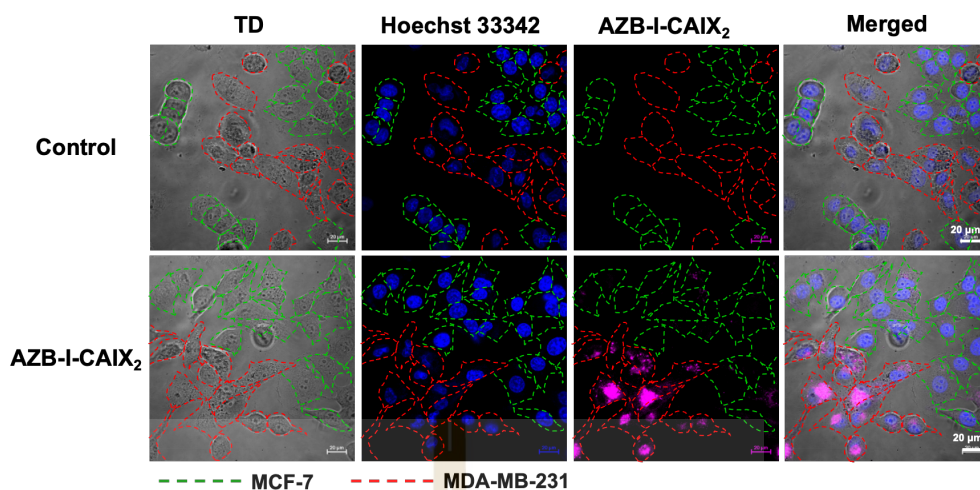


**Figure 4.26** The confocal images display the 5  $\mu\text{M}$  of AZB-I-CAIX<sub>2</sub> for 6 h treatment in co-cultured between MDA-MB-231 and MCF-7.

#### 4.2.2 Competitive effect with CAIX ligand

A competition experiment was done to validate the CAIX-mediated uptake of AZB-I-CAIX<sub>2</sub> in cancer cells to further demonstrate the selectivity of AZB-I-CAIX<sub>2</sub>. At 6 h, MDA-MB-231 cells were treated with AZB-I-CAIX<sub>2</sub> (5  $\mu\text{M}$ ) in the presence of different doses (0, 0.5, and 1.0 mM) of the CAIX inhibitor, acetazolamide. CAIX inhibitor decreased cellular uptake of AZB-I-CAIX<sub>2</sub> in a dose-dependent. (Figure 4.27A). Quantitation of the fluorescence signals (Figure 4.27B) shows clearly decreasing fluorescence intensity as the concentration of acetazolamide increases, which confirms that acetazolamide moieties play a key role in cellular internalization.

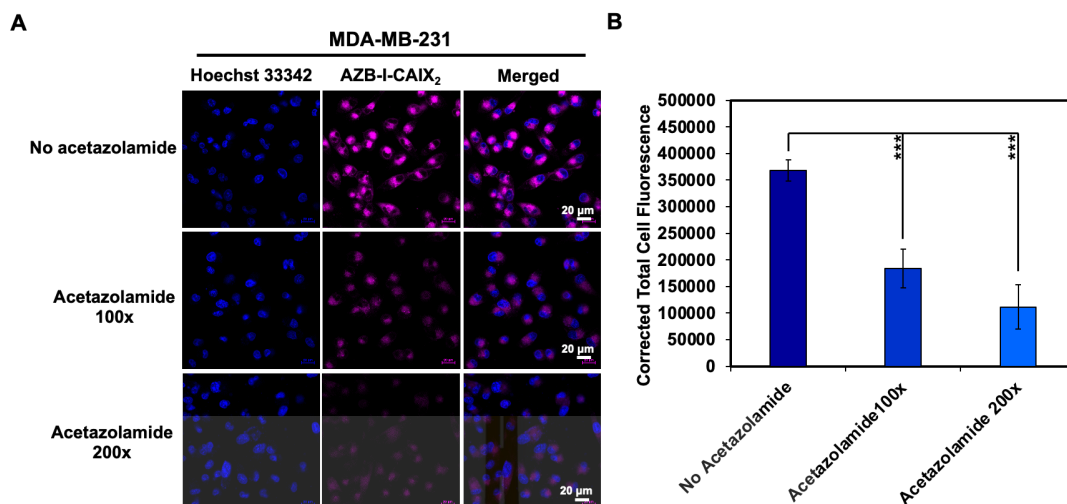


**Figure 4.27** CAIX competitive effect. MDA-MB-231 were incubated **AZB-I-CAIX<sub>2</sub>** (5  $\mu$ M) and CAIX inhibitor (acetazolamide, 100x and 200x) for 6 h. **A)** Confocal images of the effect. **B)** Quantitative of the fluorescence signals by ImageJ. The data represent the mean  $\pm$  SD (n = 50) and statistical analysis by t-test (Tukey's analysis) using GrapPad Prism9 software. P values of less than 0.05 (95% confidence interval) are considered significant (\*\*\*)  $p < 0.001$ ).

### 4.2.3 Colocalization study

In addition to cellular uptake, the cell localization of detected fluorescence signals of **AZB-I-CAIX<sub>2</sub>** from MDA-MB-231 cells were studied. However, CAIX is an integral plasma membrane protein that regulates intra- and extracellular pH. From the literature (Hulikova et al., 2009), the domain-deletion strategy used in their research helped to explain the functional significance of the extracellular portion of CAIX. As an outcome, CAIX transfected cells were employed (transfected with a pSG5C-DIC plasmid encoding the CAIX protein lacking intracellular 24 amino acids from the C-terminus). The confocal image revealed that fluorescent carbonic anhydrase sulfonamide (FITC-CA) is not present at the cell surface but is localized intracellularly, overlapping with the endoplasmic reticulum (ER), in contrast to wild-type CAIX cells in which it was almost completely localized in the plasma membrane. Because in the C-terminally truncated CAIX cells lost the pH control function, this may lead to cell internalization of CAIX. Accordingly, **AZB-I-CAIX<sub>2</sub>** was not visible on the membrane

(Figure 4.28). Nevertheless, **AZB-I-CAIX<sub>2</sub>** was found to be colocalized to some degree with ER, Mito, Golgi, and Lyso trackers in MDA-MB-231 with Pearson's coefficients of 0.74, 0.47, 0.28, and 0.22 respectively. This confirms that **AZB-I-CAIX<sub>2</sub>** can be mostly localized in ER. However, MDA-MB-231 we used does not transfect with a special plasmid encode but **AZB-I-CAIX<sub>2</sub>** may lose some function of CAIX resulting in internalization of CAIX in response to **AZB-I-CAIX<sub>2</sub>** binding in the cancer cells.

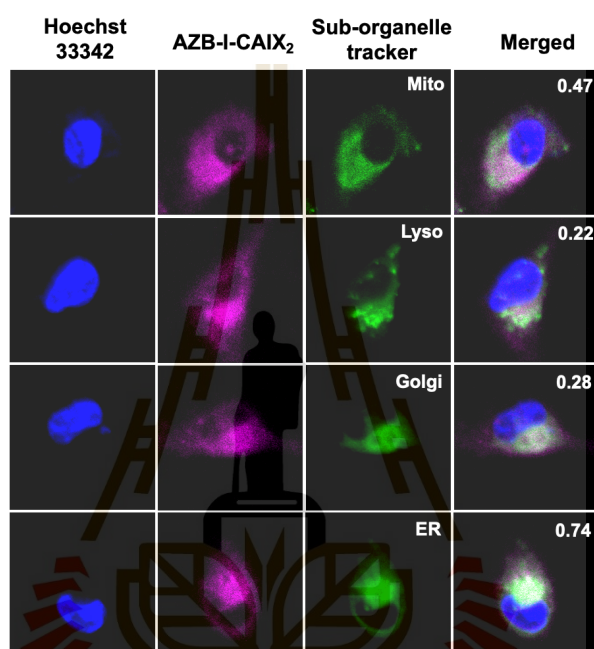
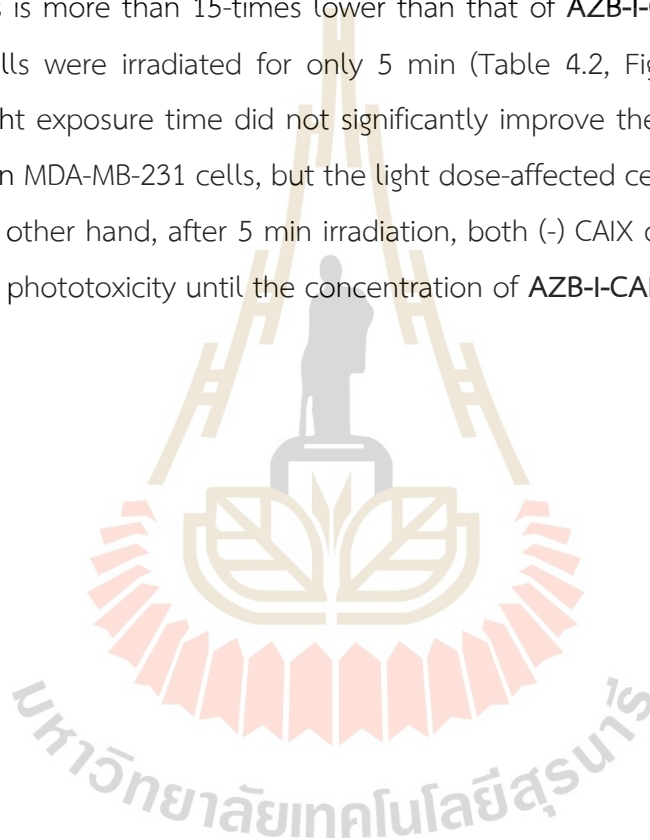


**Figure 4.28** Colocalization confocal images and Pearson's coefficients. MDA-MB-231 cells were incubated with 5  $\mu\text{M}$  of **AZB-I-CAIX<sub>2</sub>** for 6 h and treated with Lyso, Mito, Golgi, and ER trackers. Pearson's coefficients investigated for 30 each organelle by ImageJ.

#### 4.2.4 Light-induced cell cytotoxicity assay

To evaluate the effect of CAIX inhibitor on PDT, assays to measure photocytotoxicity of **AZB-I-CAIX<sub>2</sub>** in all cell lines including (+) CAIX, (-) CAIX, and normal cells were performed. All cells were treated with various doses (0 - 10  $\mu\text{M}$ ) of **AZB-I-CAIX<sub>2</sub>** for 6 h before light irradiation (660 nm, power density of 8.7  $\text{mW cm}^{-2}$ ) with different durations (0, 5, 10, and 15 min) and then the cells were cultured in the dark for another 24 h. As shown in Figure 4.29A, **AZB-I-CAIX<sub>2</sub>** did not cause cytotoxicity to

any cells that were not illuminated (0 min). However, once the irradiation was on, the cell viability of all cells was decreasing as the dose of **AZB-I-CAIX<sub>2</sub>** was increased. Remarkably, (+) CAIX cells (MDA-MB-231) are the most sensitive cells to **AZB-I-CAIX<sub>2</sub>**. After the cells were irradiated for 5 min, the viability of MDA-MB-231 was reduced to 50% at a very low concentration (0.25  $\mu\text{M}$ ) and the probe even caused more photocytotoxicity when the irradiation time was longer (10 and 15 min) in a dose-dependent manner. The half-maximal inhibitory concentration ( $\text{IC}_{50}$ ) of **AZB-I-CAIX<sub>2</sub>** in (+) CAIX cells is more than 15-times lower than that of **AZB-I-CAIX<sub>2</sub>** in (-) CAIX cells when the cells were irradiated for only 5 min (Table 4.2, Figure 4.29B). However, prolonged light exposure time did not significantly improve the therapeutic index of **AZB-I-CAIX<sub>2</sub>** in MDA-MB-231 cells, but the light dose-affected cell viabilities of (-) CAIX cells. On the other hand, after 5 min irradiation, both (-) CAIX cells and normal cells did not show phototoxicity until the concentration of **AZB-I-CAIX<sub>2</sub>** was up to 5  $\mu\text{M}$ .



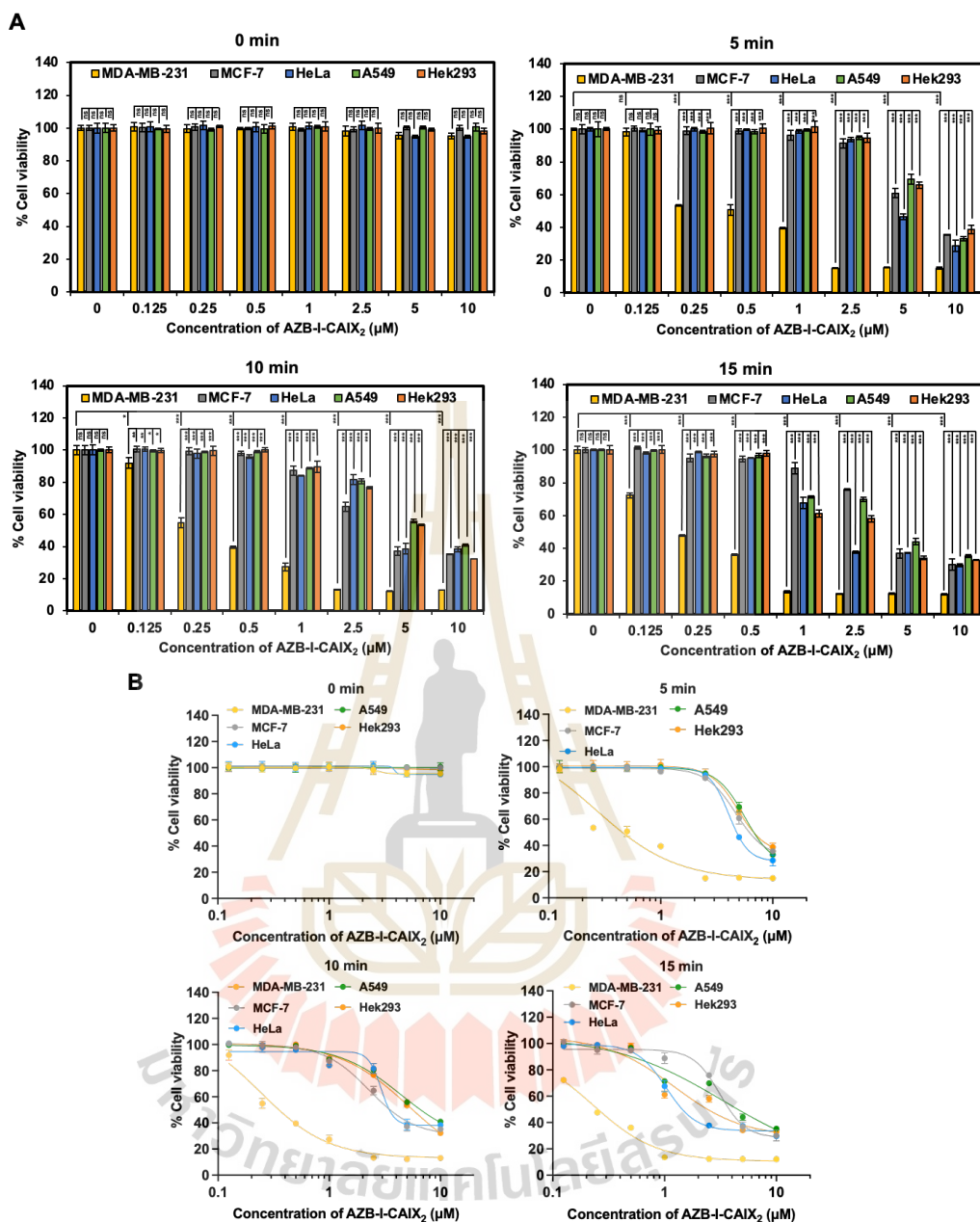


**Figure 4.29** Light-induced cell cytotoxicity of **AZB-I-CAIX<sub>2</sub>** in human cell lines. **A)** Cell viability when all human cells were incubated with various concentrations of **AZB-I-CAIX<sub>2</sub>** for 6 h and irradiated with lamp (660 nm, power density of 8.7 mW cm<sup>-2</sup>) in a different time. The data statistical analysis by One-way ANOVA (Tukey's analysis) using GrapPad Prism9 software. P values of less than 0.05 (95% confidence interval) are considered significant (ns  $p < 0.12$ , \*  $p < 0.033$ , \*\* $p < 0.002$ , \*\*\* $p < 0.001$ ). **B)** Dose-response curve of **AZB-I-CAIX<sub>2</sub>** under the light exposure used to generate IC<sub>50</sub> by GrapPad Prism9 software.

**Table 4.2** IC<sub>50</sub> values of **AZB-I-CAIX<sub>2</sub>** after 6 h treatment and irradiation with light in all cells.

Irradiation time (min)	IC <sub>50</sub> (μM)				
	MDA-MB-231	MCF-7	HeLa	A549	Hek293
0	>10	>10	>10	>10	>10
5	0.27	4.68	4.06	5.64	4.88
10	0.24	2.28	2.92	4.44	4.22
15	0.23	3.11	1.03	3.33	1.23

Moreover, photo-induced cell toxicity was performed on breast cancer lines (MDA-MD-231 and MCF-7) using **AZB-I-control**. No dramatic change in cell viability was observed from both (+) CAIX and (-) CAIX cell lines even with light irradiation for up to 15 min and compound concentration was up to 10 μM (Figure 4.30). These results confirm the selectivity of **AZB-I-CAIX<sub>2</sub>** towards CAIX overexpression on cancer cells. However, a long-time light was exposed to the cells, the result showed 100% cell viability in 15 min as shown in Figure 4.31, indicating that the light did not show any toxicity to the cells.

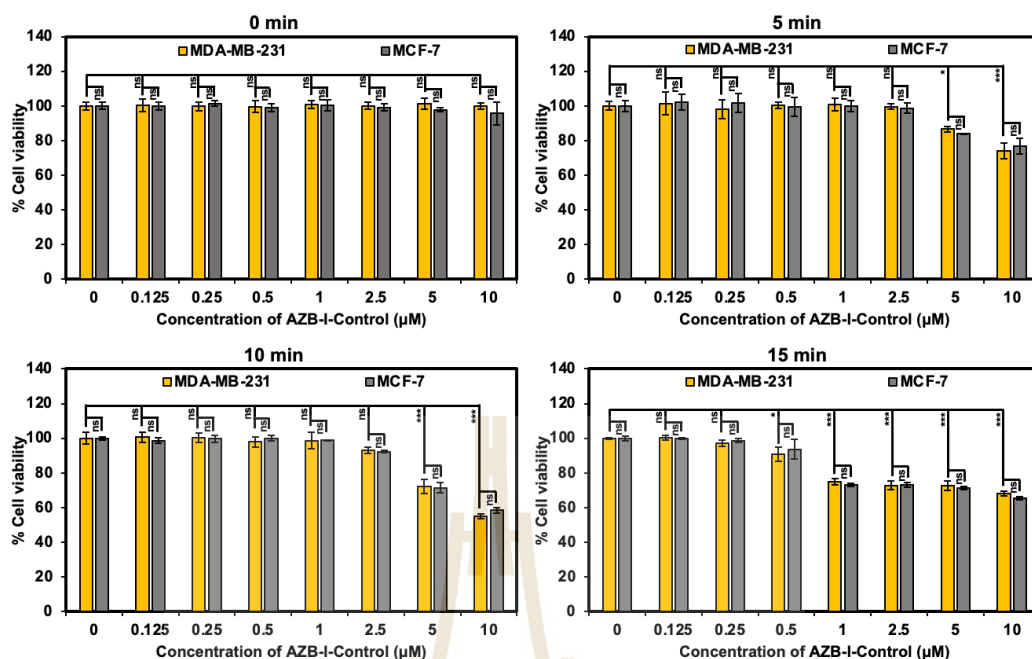


Figure 4.30 Light-induced cell cytotoxicity of AZB-I-Control in human cell lines. Cell viability when all human cells were incubated with various concentrations of AZB-I-Control for 6 h and irradiated with a lamp (660 nm, power density of  $8.7 \text{ mW cm}^{-2}$ ) for different time periods. The data statistical analysis by One-way ANOVA (Tukey's analysis) using GrapPad Prism9 software. P values of less than 0.05 (95% confidence interval) are considered significant (ns  $p < 0.12$ , \*  $p < 0.033$ , \*\*  $p < 0.002$ , \*\*\*  $p < 0.001$ ).

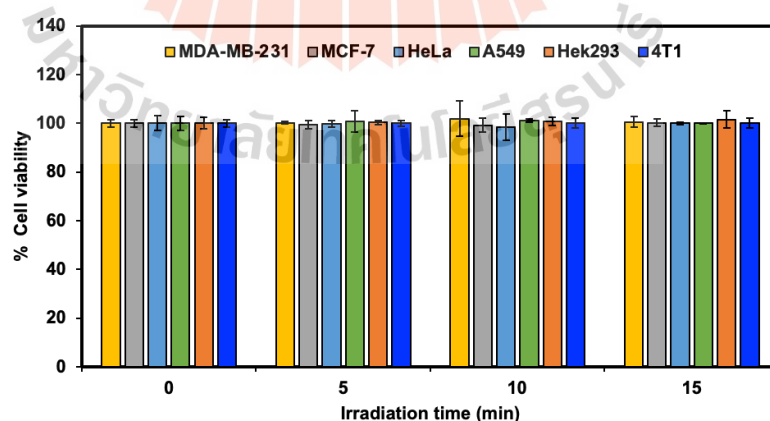
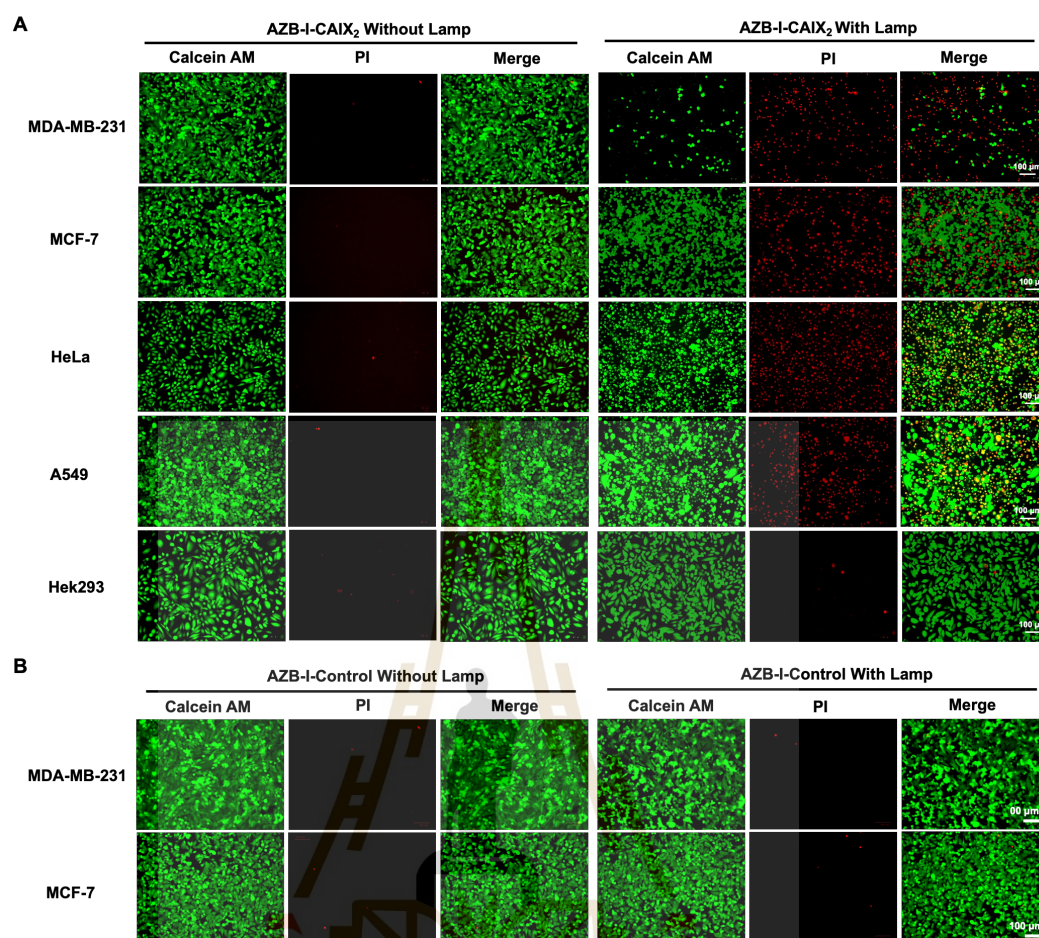


Figure 4.31 The cell viability of all cells after irradiation with light.

#### 4.2.5 Live/Dead staining

To further confirm that the (+) CAIX cancer cells were destroyed by reactive oxygen species (ROS) from light activation reaction, viability/cytotoxicity and intracellular ROS detection assays were performed. Viable and dead cells were visualized using calcein AM and propidium iodide (PI) staining. Once calcein AM enters live cells, green fluorescence can be observed after the dye is cleaved the acetoxymethyl (AM) ester group by intracellular esterase upon entering the cell, resulting in the membrane-impermeable Calcein fluorescent dye which Calcein is not maintained in apoptotic and dead cells with damaged cell membranes, while PI is a commonly used reagent for determining cell viability and excluding non-viable cells but it freely penetrates cell membranes of dead or dying cells but is excluded from viable cells and gives red fluorescence. As shown in Figure 4.32A, all the cells incubated with **AZB-I-CAIX<sub>2</sub>** (no light irradiation) barely showed any dead cells (indicated as a red signal), but after cells were irradiated with the light, a high number of dead cells could be observed from MDA-MB-231, while the live cells (indicated as green signal) were very few. Other (-) CAIX cancer cells showed some dead cells signal along with a high population of viable cells. Moreover, little to no dead cells were detected in the case of a normal cell (HEK293). The cells samples incubated with **AZB-I-control** (with and without illumination) mostly retained a large number of surviving cells and showed none of the dead cells (Figure 4.32B). The results indicated that **AZB-I-CAIX<sub>2</sub>** causes light-induced cell death by PDT via CAIX expression and the CAIX inhibitor part is important to target the cells.



**Figure 4.32** Live/dead cell staining in (+) CAIX cells and (-) CAIX cells. **A)** AZB-I-CAIX<sub>2</sub> and **B)** AZB-I-control, cells were treated with 0.5  $\mu\text{M}$  for 6 h before being exposed to the light from a lamp (660 nm, power density of 8.7  $\text{mW cm}^{-2}$ ) for 5 min and continued cultured for another 24 h in dark.

#### 4.2.6 Intracellular Singlet Oxygen Generation

To detect intracellular Reactive Oxygen Species (ROS) production, 2',7'-dichlorofluorescein diacetate (DCFH-DA) was used as its non-fluorescent form can be oxidized by ROS to produce the fluorescence 2',7'-dichlorofluorescein (DCF) that exhibits green fluorescence inside the living cells (Yu et al., 2021). As shown in Figure 4.33, bright green emission was clearly observed only in the case of MDA-MB-231 cells incubated with AZB-I-CAIX<sub>2</sub> followed by light activation. The green fluorescence increased when a higher amount of AZB-I-CAIX<sub>2</sub> was used, implying the ROS was generated from AZB-I-CAIX<sub>2</sub> inside the cells in the dose-response relationship.

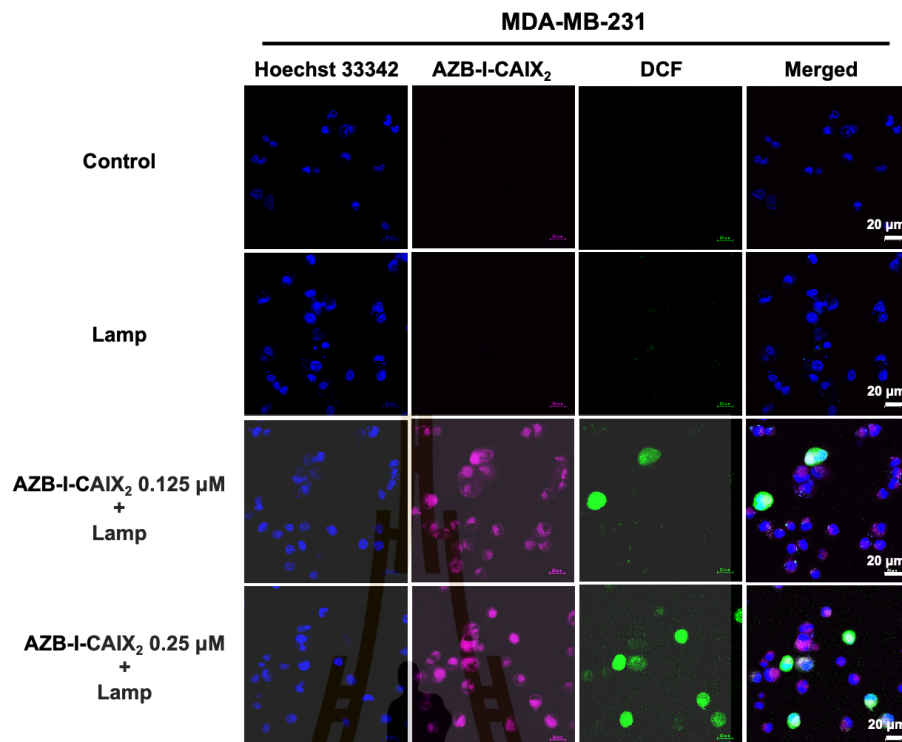


**Figure 4.33** Detection of intracellular reactive oxygen species generation. Concentration of 0.125 and 0.25  $\mu\text{M}$  of AZB-I-CAIX<sub>2</sub> were treated for 6 h and exposed with the lamp (660 nm, power density of 8.7  $\text{mW cm}^{-2}$ ) for 5 min in MDA-MB-231 cells using DCFH-DA cellular ROS detection assay.

#### 4.2.7 Murine cell internalization under hypoxia condition

We wanted to expand our study to an animal model. Therefore, two murine breast cancer lines were used as a comparison. 4T1 cells are highly metastatic breast cancer cells. Compared to nonmetastatic 67NR cells, tumors formed by 4T1 have significantly higher amounts of hypoxia, necrosis, and apoptosis due to fewer blood vessels. In the previously published finding (Y. Lou et al., 2008; Robertson, Potter, & Harris, 2004), the bioinformatic analysis revealed several hypoxia-regulated genes, including CAIX, that are expressed at higher levels in the 4T1 tumors in contrast to the absence of hypoxia induced CAIX in the 67NR cells. Therefore, the 4T1 mouse could be a suitable model to study the effect of overexpression of CAIX on the progression of breast cancer (Chafe et al., 2015; Yuanmei Lou et al., 2011).

Prior to testing in an animal model, internalization experiments were performed in 4T1 and 67NR cells under normoxia and hypoxia conditions. **AZB-I-CAIX<sub>2</sub>** could be observed only from hypoxic 4T1 cells since 1 h incubation (Figure 4.34) and the fluorescence increased in a time-dependent manner, while lower fluorescence signals were displayed in hypoxic 67NR cells. Despite extensive incubation times, little fluorescence was seen in both normoxic 4T1 and 67NR cells.

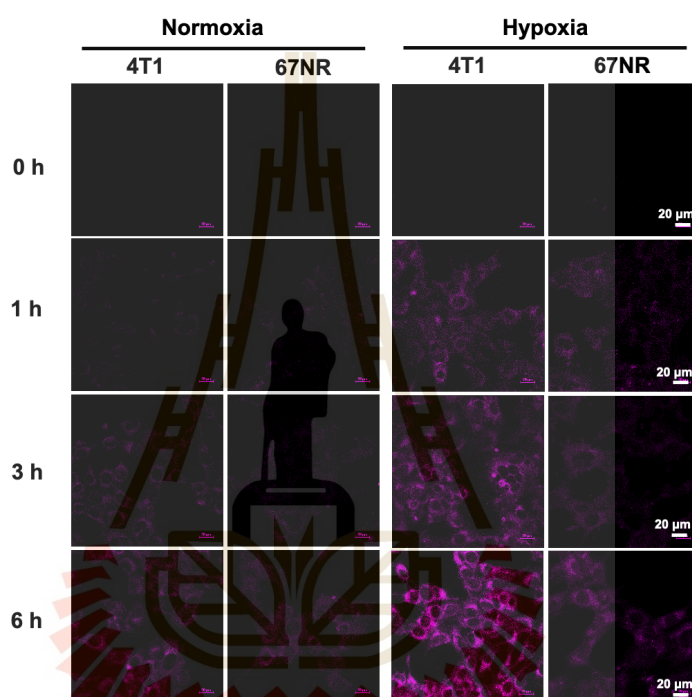


**Figure 4.34** Confocal image of murine cell lines (4T1 and 67NR) under normoxia and hypoxia. All cells were induced CAIX expression in the hypoxia chamber for 12 h before being treated with **AZB-I-CAIX<sub>2</sub>** (5  $\mu$ M) for 0, 1, 3, and 6 h.

#### 4.2.8 Photo-induced murine cell cytotoxicity assay under hypoxia condition

After 4T1 cells (normoxia and hypoxia) were treated with **AZB-I-CAIX<sub>2</sub>** for 6 h, the light at different time durations (0, 5, 10, and 15 min) was exposed to the cells. As shown in cell viabilities and IC<sub>50</sub> curves of photo-induced cytotoxicity (Figure 4.35A-B), hypoxic cells were significantly more sensitive to light compared to the normoxic ones. When a longer exposure time was given, the IC<sub>50</sub> of hypoxic 4T1 cells was lower (Table

4.3). Therefore, under hypoxia conditions in which 4T1 expresses higher CAIX levels, AZB-I-CAIX<sub>2</sub> can be internalized more, leading to a higher accumulation of tumor cells. Moreover, PDT was still active even under a low oxygen concentration environment.

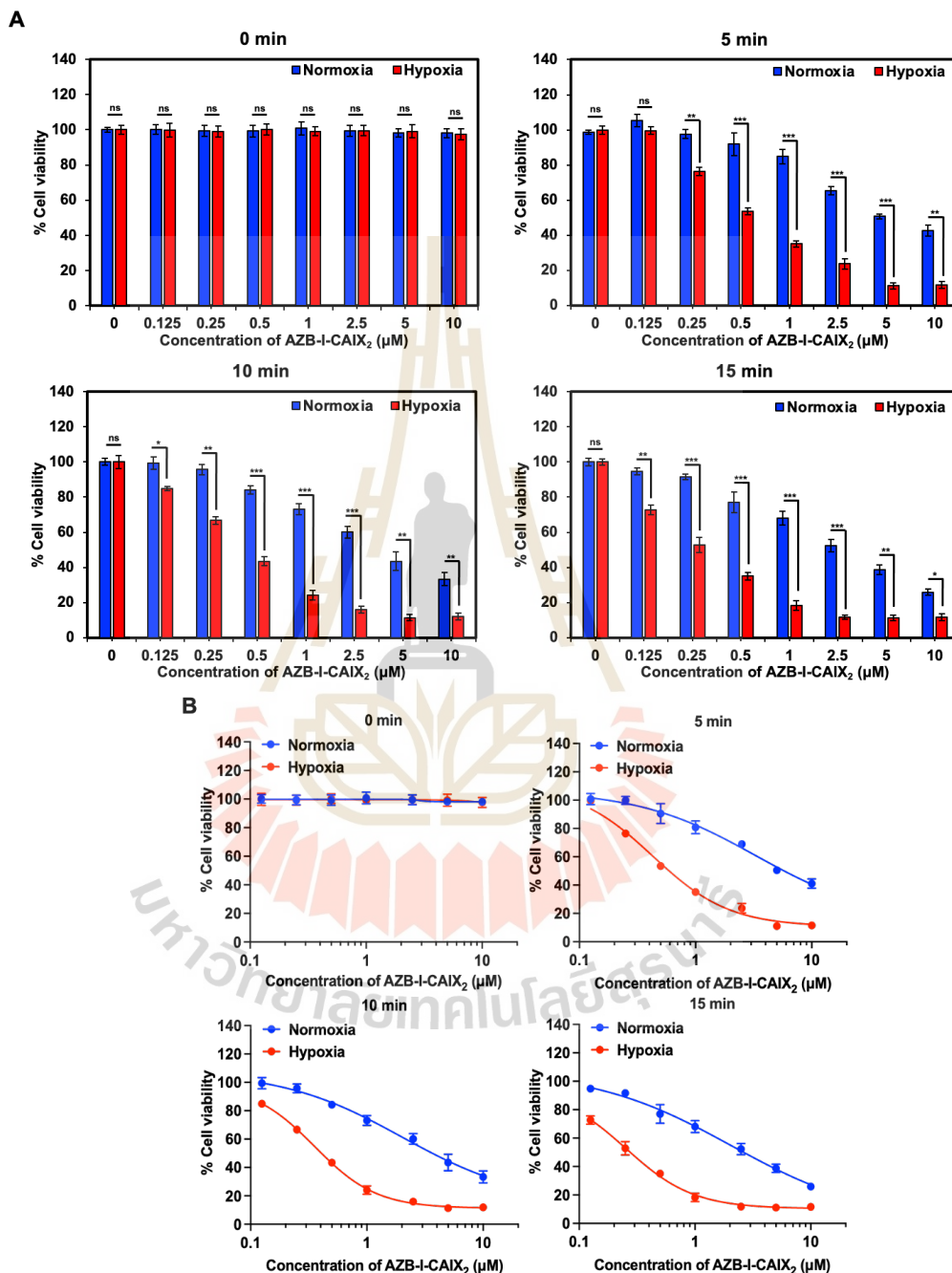


**Figure 4.35** Light-induced cell cytotoxicity of AZB-I-CAIX<sub>2</sub> in murine cell lines under hypoxia condition. **A**) Cell viability when 4T1 cells were induced to increase the CAIX levels by hypoxia and normoxia as a control for 12 h before incubation with various concentrations of AZB-I-CAIX<sub>2</sub> for 6 h and irradiated with light from a lamp (660 nm,

power density of  $8.7 \text{ mW cm}^{-2}$ ) for different time periods. The data statistical analysis by One-way ANOVA (Tukey's analysis) using GrapPad Prism9 software. P values of less than 0.05 (95% confidence interval) are considered significant (ns  $p < 0.12$ , \*  $p < 0.033$ , \*\* $p < 0.002$ , \*\*\* $p < 0.001$ ). **B)** Dose-response curve of **AZB-I-CAIX<sub>2</sub>** under normoxia and hypoxia with the light exposure used to generate IC<sub>50</sub> by GrapPad Prism9 software.

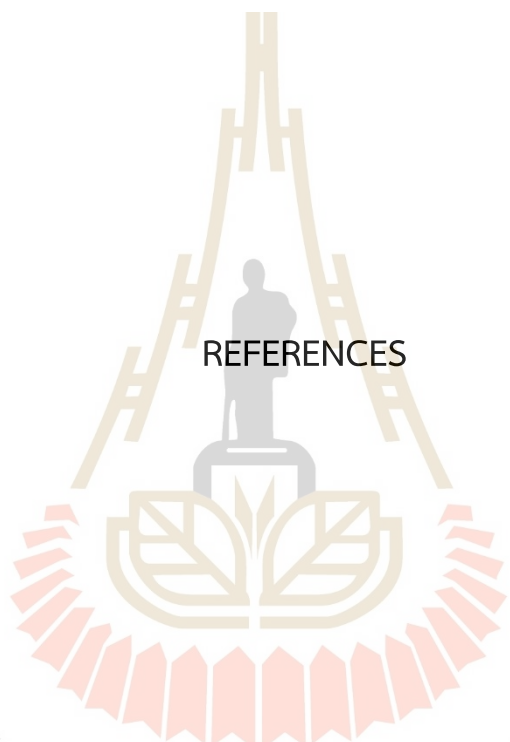
**Table 4.3** IC<sub>50</sub> values of **AZB-I-CAIX<sub>2</sub>** under hypoxic environment for 12 h before treatment for 6 h and irradiation with the light in 4T1 cells.

Irradiation time (min)	IC <sub>50</sub> (μM)	
	Normoxia	Hypoxia
0	>10	>10
5	3.30	0.43
10	2.02	0.36
15	2.01	0.25

## CHAPTER V

### CONCLUSION

This thesis reported a combination of photosensitizer and anti-angiogenesis (CAIX inhibitor, acetazolamide) strategies for cancer treatment. **AZB-I-CAIX<sub>2</sub>** has been developed by conjugation of two equivalent acetazolamide to aza-BODIPY which is a NIR singlet oxygen-producing photosensitizer. A similar structure without acetazolamide was proposed as control which offers only PDT effect without any targeting ability (**AZB-I-control**). *In vitro* studies revealed that **AZB-I-CAIX<sub>2</sub>** preferentially localizes in the ER of human breast cancer cells that overexpress CAIX, whereas **AZB-I-control** did not show any cell uptake. Moreover, **AZB-I-CAIX<sub>2</sub>** generates singlet oxygen efficiently upon irradiation at 660 nm and provides selectively photo-induced cell cytotoxicity at a very low concentration and short-time light exposure. Furthermore, murine cells cultured in a hypoxic environment were used as a hypoxia model. Under hypoxia, 4T1 exhibited a strong fluorescence of **AZB-I-CAIX<sub>2</sub>** and was more sensitive when treated by PDT. Based on this study, **AZB-I-CAIX<sub>2</sub>** is the NIR photosensitizer that could be a remarkable probe for detecting CAIX expressed cells and enhancing therapeutic efficacy via decreasing PDT-induced hypoxia limitation by angiogenesis knockdown through CAIX.



REFERENCES

มหาวิทยาลัยเทคโนโลยีสุรนารี

## REFERENCES

- Abd-El Fattah, A. A., Darwish, H. A., Fathy, N., and Shouman, S. A. (2017). Carbonic anhydrase inhibition boosts the antitumor effects of Imatinib mesylate via potentiating the antiangiogenic and antimetastatic machineries. *Toxicol Appl Pharmacol*, 316, 123-138.
- Ahlskog, J. K., Dumelin, C. E., Trüssel, S., Mårlind, J., and Neri, D. (2009). In vivo targeting of tumor-associated carbonic anhydrases using acetazolamide derivatives. *Bioorg Med Chem Lett*, 19(16), 4851-4856.
- Baldea, I., and Filip, A. G. (2012). Photodynamic therapy in melanoma an update. *J Physiol Pharmacol*, 63(2), 109-118.
- Becker, H. M. (2020). Carbonic anhydrase IX and acid transport in cancer. *British Journal of Cancer*, 122(2), 157-167.
- Brahimi, F., Ko, E., Malakhov, A., Burgess, K., and Saragovi, H. U. (2014). Combinatorial assembly of small molecules into bivalent antagonists of TrkC or TrkA receptors. *PLOS ONE*, 9(3), e89617.
- Bui, M. H., Seligson, D., Han, K. R., Pantuck, A. J., Dorey, F. J., Huang, Y., Horvath, S., Leibovich, B. C., Chopra, S., Liao, S. Y., Stanbridge, E., Lerman, M. I., Palotie, A., Figlin, and R. A., Belldegrun. (2003). Carbonic anhydrase IX is an independent predictor of survival in advanced renal clear cell carcinoma: implications for prognosis and therapy. *Clin Cancer Res*, 9(2), 802-811.
- Calixto, G. M., Bernegossi, J., De Freitas, L. M., Fontana, C. R., and Chorilli, M. (2016). Nanotechnology-Based Drug Delivery Systems for Photodynamic Therapy of Cancer: A Review. *Molecules*, 21(3).
- Carlson, C. B., Mowery, P., Owen, R. M., Dykhuizen, E. C., and Kiessling, L. L. (2007). Selective tumor cell targeting using low-affinity, multivalent interactions. *ACS Chem Biol*, 2(2), 119-127.
- Chafe, S. C., Lou, Y., Sceneay, J., Vallejo, M., Hamilton, M. J., McDonald, P. C., Bennewith, K. L., Möller, A., and Dedhar, S. (2015). Carbonic Anhydrase IX Promotes Myeloid

- Derived Suppressor Cell Mobilization and Establishment of a Metastatic Niche by Stimulating G-CSF Production. *Cancer Research*, 75(6), 996-1008.
- Chinen, A. B., Guan, C. M., Ferrer, J. R., Barnaby, S. N., Merkel, T. J., and Mirkin, C. A. (2015). Nanoparticle Probes for the Detection of Cancer Biomarkers, Cells, and Tissues by Fluorescence. *Chem Rev*, 115(19), 10530-10574.
- De Simone, B. C., Mazzone, G., Pirillo, J., Russo, N., and Sicilia, E. (2017). Halogen atom effect on the photophysical properties of substituted aza-BODIPY derivatives. *Physical Chemistry Chemical Physics*, 19(3), 2530-2536.
- Ding, H., Yu, H., Dong, Y., Tian, R., Huang, G., Boothman, D. A., Sumer, B. D., and Gao, J. (2011). Photoactivation switch from type II to type I reactions by electron-rich micelles for improved photodynamic therapy of cancer cells under hypoxia. *Journal of controlled release : official journal of the Controlled Release Society*, 156(3), 276-280.
- Dolmans, D. E. J. G. J., Fukumura, D., and Jain, R. K. (2003). Photodynamic therapy for cancer. *Nature Reviews Cancer*, 3(5), 380-387.
- Dubois, L., Lieuwes, N. G., Maresca, A., Thiry, A., Supuran, C. T., Scozzafava, A., Wouters, B. G., and Lambin, P. (2009). Imaging of CA IX with fluorescent labelled sulfonamides distinguishes hypoxic and (re)-oxygenated cells in a xenograft tumour model. *Radiother Oncol*, 92(3), 423-428.
- Ercin, U., Aribas, Y. K., Tefon Aribas, A. B., Bilgihan, A., and Bilgihan, K. (2021). Singlet oxygen formation during accelerated and hyperaccelerated corneal cross-linking: in vitro study. *Eye*, 35(11), 3147-3151.
- Ferrara, N., and Kerbel, R. S. (2005). Angiogenesis as a therapeutic target. *Nature*, 438(7070), 967-974.
- Ferrario, A., and Gomer, C. J. (2010). Targeting the 90 kDa heat shock protein improves photodynamic therapy. *Cancer Lett*, 289(2), 188-194.
- Ferrario, A., von Tiehl, K. F., Rucker, N., Schwarz, M. A., Gill, P. S., and Gomer, C. J. (2000). Antiangiogenic treatment enhances photodynamic therapy responsiveness in a mouse mammary carcinoma. *Cancer Res*, 60(15), 4066-4069.
- Galbán, S., and Gorospe, M. (2009). Factors interacting with HIF-1 alpha mRNA: novel therapeutic targets. *Current pharmaceutical design*, 15(33), 3853-3860.

- Gallagher-Colombo, S. M., Maas, A. L., Yuan, M., and Busch, T. M. (2012). Photodynamic therapy-induced angiogenic signaling: consequences and solutions to improve therapeutic response. *Israel journal of chemistry*, 52(8-9), 681-690.
- Grosjean, P., Wagnieres, G., Fontolliet, C., van den Bergh, H., and Monnier, P. (1998). Clinical photodynamic therapy for superficial cancer in the oesophagus and the bronchi: 514 nm compared with 630 nm light irradiation after sensitization with Photofrin II. *British Journal of Cancer*, 77(11), 1989-1995.
- He, S., Song, J., Qu, J., and Cheng, Z. (2018). Crucial breakthrough of second near-infrared biological window fluorophores: design and synthesis toward multimodal imaging and theranostics. *Chemical Society Reviews*, 47(12), 4258-4278.
- Huang, Z. (2005). A review of progress in clinical photodynamic therapy. *Technol Cancer Res Treat*, 4(3), 283-293.
- Hulikova, A., Zatovicova, M., Svastova, E., Ditte, P., Brasseur, R., Kettmann, Supuran, C. T., Kopacek, J., Pastorek, J., and Pastorekova, S. (2009). Intact intracellular tail is critical for proper functioning of the tumor-associated, hypoxia-regulated carbonic anhydrase IX. *FEBS Letters*, 583(22), 3563-3568.
- Jung, H. S., Han, J., Shi, H., Koo, S., Singh, H., Kim, H.-J., Sessler, J. L., Lee, J. Y., Kim, J.-H., and Kim, J. S. (2017). Overcoming the Limits of Hypoxia in Photodynamic Therapy: A Carbonic Anhydrase IX-Targeted Approach. *Journal of the American Chemical Society*, 139(22), 7595-7602.
- Kalinin, S., Malkova, A., Sharonova, T., Sharoyko, V., Bunev, A., Supuran, C. T., and Krasavin, M. (2021). Carbonic Anhydrase IX Inhibitors as Candidates for Combination Therapy of Solid Tumors. *International Journal of Molecular Sciences*, 22(24).
- Kaluz, S., Kaluzová, M., Liao, S. Y., Lerman, M., and Stanbridge, E. J. (2009). Transcriptional control of the tumor- and hypoxia-marker carbonic anhydrase 9: A one transcription factor (HIF-1) show? *Biochim Biophys Acta*, 1795(2), 162-172.
- Kamkaew, A., and Burgess, K. (2015). Aza-BODIPY dyes with enhanced hydrophilicity. *Chemical Communications*, 51(53), 10664-10667.

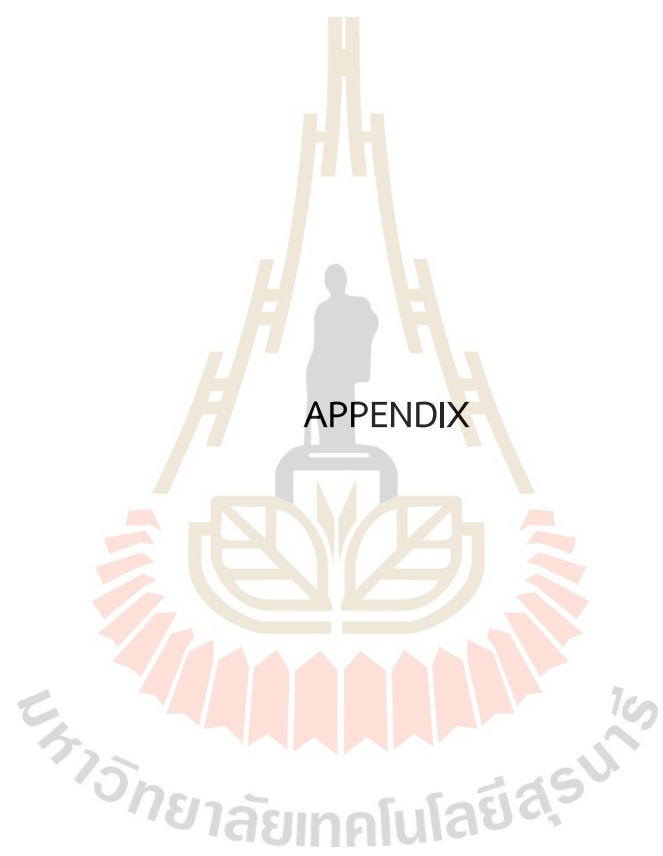
- Kamkaew, A., Lim, S. H., Lee, H. B., Kiew, L. V., Chung, L. Y., and Burgess, K. (2013). BODIPY dyes in photodynamic therapy. *Chem Soc Rev*, 42(1), 77-88.
- Kamkaew, A., Lim, S. H., Lee, H. B., Kiew, L. V., Chung, L. Y., and Burgess, K. (2013). BODIPY dyes in photodynamic therapy. *Chemical Society Reviews*, 42(1), 77-88.
- Kikuchi, R., Stevens, M., Harada, K., Oltean, S., and Murohara, T. (2019). Anti-angiogenic isoform of vascular endothelial growth factor-A in cardiovascular and renal disease. *Adv Clin Chem*, 88(1), 1-33.
- Krall, N., Pretto, F., Decurtins, W., Bernardes, G. J., Supuran, C. T., and Neri, D. (2014). A small-molecule drug conjugate for the treatment of carbonic anhydrase IX expressing tumors. *Angew Chem Int Ed Engl*, 53(16), 4231-4235.
- Krall, N., Pretto, F., and Neri, D. (2014). A bivalent small molecule-drug conjugate directed against carbonic anhydrase IX can elicit complete tumour regression in mice. *Chemical Science*, 5(9), 3640-3644.
- Krzykawska-Serda, M., Dąbrowski, J. M., Arnaut, L. G., Szczygieł, M., Urbańska, K., Stochel, G., and Elas, M. (2014). The role of strong hypoxia in tumors after treatment in the outcome of bacteriochlorin-based photodynamic therapy. *Free Radic Biol Med*, 73(1), 239-251.
- Kue, C. S., Ng, S. Y., Voon, S. H., Kamkaew, A., Chung, L. Y., Kiew, L. V., and Lee, H. B. (2018). Recent strategies to improve boron dipyrromethene (BODIPY) for photodynamic cancer therapy: an updated review. *Photochemical & Photobiological Sciences*, 17(11), 1691-1708.
- Li, Y., Wang, H., Oosterwijk, E., Tu, C., Shiverick, K. T., Silverman, D. N., and Frost, S. C. (2009). Expression and activity of carbonic anhydrase IX is associated with metabolic dysfunction in MDA-MB-231 breast cancer cells. *Cancer Invest*, 27(6), 613-623.
- Liang, P., Ballou, B., Lv, X., Si, W., Bruchez, M. P., Huang, W., and Dong, X. (2021). Monotherapy and Combination Therapy Using Anti-Angiogenic Nanoagents to Fight Cancer. *Adv Mater*, 33(15), e2005155.
- Liu, L., Wang, W., Huang, J., Zhao, Z., Li, H., and Xu, Y. (2018). Novel benzoyl thioureido benzene sulfonamides as highly potent and selective inhibitors of carbonic

- anhydrase IX: optimization and bioactive studies. *Medchemcomm*, 9(12), 2100-2105.
- Lock, F. E., McDonald, P. C., Lou, Y., Serrano, I., Chafe, S. C., Ostlund, C., Aparicio, S., Winum, J.-Y., Supuran, C. T., and Dedhar, S., (2013). Targeting carbonic anhydrase IX depletes breast cancer stem cells within the hypoxic niche. *Oncogene*, 32(44), 5210-5219.
- Lou, Y., McDonald, P. C., Oloumi, A., Chia, S., Ostlund, C., Ahmadi, A., Kyle, A., Keller, U., Leung, S., Huntsman, D., Clarke, B., Sutherland, B. W., Waterhouse, D., Bally, M., Roskelley, C., Overall, C. M., Minchinton, A., Pacchiano, F., Carta, F., Scozzafava, A., Touisni, N., Winum, J.-Y., Supuran, C. T., and Dedhar, S. (2011). Targeting Tumor Hypoxia: Suppression of Breast Tumor Growth and Metastasis by Novel Carbonic Anhydrase IX Inhibitors. *Cancer Research*, 71(9), 3364-3376.
- Lou, Y., Preobrazhenska, O., auf dem Keller, U., Sutcliffe, M., Barclay, L., McDonald, P. C., Roskelley, C., Overall, C. M., and Dedhar, S. (2008). Epithelial-mesenchymal transition (EMT) is not sufficient for spontaneous murine breast cancer metastasis. *Dev Dyn*, 237(10), 2755-2768.
- Lucky, S. S., Soo, K. C., and Zhang, Y. (2015). Nanoparticles in photodynamic therapy. *Chem Rev*, 115(4), 1990-2042.
- Macdonald, I. J., and Dougherty, T. J. (2001). Basic principles of photodynamic therapy. *Journal of Porphyrins and Phthalocyanines*, 5(2), 105-129.
- Mahalingam, S. M., Chu, H., Liu, X., Leamon, C. P., and Low, P. S. (2018). Carbonic Anhydrase IX-Targeted Near-Infrared Dye for Fluorescence Imaging of Hypoxic Tumors. *Bioconjug Chem*, 29(10), 3320-3331.
- Mahfouz, N., Tahtouh, R., Alaaeddine, N., El Hajj, J., Sarkis, R., Hachem, R., Raad, I., and Hilal, G. (2017). Gastrointestinal cancer cells treatment with bevacizumab activates a VEGF autoregulatory mechanism involving telomerase catalytic subunit hTERT via PI3K-AKT, HIF-1 $\alpha$  and VEGF receptors. *PLOS ONE*, 12(6), e0179202.
- McDonald, P. C., Winum, J. Y., Supuran, C. T., and Dedhar, S. (2012). Recent developments in targeting carbonic anhydrase IX for cancer therapeutics. *Oncotarget*, 3(1), 84-97.

- Mitra, S., Cassar, S. E., Niles, D. J., Puskas, J. A., Frelinger, J. G., and Foster, T. H. (2006). Photodynamic therapy mediates the oxygen-independent activation of hypoxia-inducible factor 1 $\alpha$ . *Mol Cancer Ther*, 5(12), 3268-3274.
- More, K. N., Lee, J. Y., Kim, D.-Y., Cho, N.-C., Pyo, A., Yun, M., Kim, H. S., Kim, H., Ko, K., Park, J.-H., and Chang, D.-J. (2018). Acetazolamide-based [ $^{18}\text{F}$ ]-PET tracer: In vivo validation of carbonic anhydrase IX as a sole target for imaging of CA-IX expressing hypoxic solid tumors. *Bioorganic & Medicinal Chemistry Letters*, 28(5), 915-921.
- Nishida, N., Yano, H., Nishida, T., Kamura, T., and Kojiro, M. (2006). Angiogenesis in cancer. *Vasc Health Risk Manag*, 2(3), 213-219.
- Pewklang, T., Chansaepak, K., Lai, R.-Y., Noisa, P., and Kamkaew, A. (2019). Aza-BODIPY probe for selective visualization of cyclooxygenase-2 in cancer cells. *RSC Advances*, 9(24), 13372-13377.
- Robertson, N., Potter, C., and Harris, A. L. (2004). Role of carbonic anhydrase IX in human tumor cell growth, survival, and invasion. *Cancer Res*, 64(17), 6160-6165.
- Semenza, G. L. (2010). Defining the role of hypoxia-inducible factor 1 in cancer biology and therapeutics. *Oncogene*, 29(5), 625-634.
- Song, X., Feng, L., Liang, C., Yang, K., and Liu, Z. (2016). Ultrasound Triggered Tumor Oxygenation with Oxygen-Shuttle Nanoperfluorocarbon to Overcome Hypoxia-Associated Resistance in Cancer Therapies. *Nano Letters*, 16(10), 6145-6153.
- Staderini, M., Legname, G., Bolognesi, M. L., and Menéndez, J. C. (2013). Modulation of prion by small molecules: from monovalent to bivalent and multivalent ligands. *Curr Top Med Chem*, 13(19), 2491-2503.
- Stiti, M., Cecchi, A., Rami, M., Abdaoui, M., Barragan-Montero, V., Scozzafava, A., Guari, Y., Winum, J.-Y., and Supuran, C. T. (2008). Carbonic anhydrase inhibitor coated gold nanoparticles selectively inhibit the tumor-associated isoform IX over the cytosolic isozymes I and II. *J Am Chem Soc*, 130(48), 16130-16131.
- Supuran, C. T. (2008). Carbonic anhydrases: novel therapeutic applications for inhibitors and activators. *Nature Reviews Drug Discovery*, 7(2), 168-181.

- Supuran, C. T. (2012). Structure-based drug discovery of carbonic anhydrase inhibitors. *J Enzyme Inhib Med Chem*, 27(6), 759-772.
- Supuran, C. T. (2017). Carbonic Anhydrase Inhibition and the Management of Hypoxic Tumors. *Metabolites*, 7(3).
- Supuran, C. T., Alterio, V., Di Fiore, A., K, D. A., Carta, F., Monti, S. M., and De Simone, G. (2018). Inhibition of carbonic anhydrase IX targets primary tumors, metastases, and cancer stem cells: Three for the price of one. *Med Res Rev*, 38(6), 1799-1836.
- Supuran, C. T., and Winum, J.-Y. (2015). Carbonic anhydrase IX inhibitors in cancer therapy: an update. *Future Medicinal Chemistry*, 7(11), 1407-1414.
- Tavares, M. R., Pechar, M., Chytil, P., and Etrych, T. (2021). Polymer-Based Drug-Free Therapeutics for Anticancer, Anti-Inflammatory, and Antibacterial Treatment. *Macromol Biosci*, 21(8), e2100135.
- Teleanu, R. I., Chircov, C., Grumezescu, A. M., and Teleanu, D. M. (2019). Tumor Angiogenesis and Anti-Angiogenic Strategies for Cancer Treatment. *Journal of clinical medicine*, 9(1), 84.
- Treekoon, J., Pewklang, T., Chansaenpak, K., Gorantla, J. N., Pengthaisong, S., Lai, R.-Y., Cairns, J. R. K., and Kamkaew, A. (2021). Glucose conjugated aza-BODIPY for enhanced photodynamic cancer therapy. *Organic & Biomolecular Chemistry*, 19(26), 5867-5875.
- V. Rapozzi, G. J. (2015). Resistance to Photodynamic Therapy in Cancer. *Anticancer Research*, 35(7), 4377.
- Vaeteewoottacharn, K., Kariya, R., Dana, P., Fujikawa, S., Matsuda, K., Ohkuma, K., Kudo, E., Kraiklang, R., Wongkham, C., Wongkham, S., and Okada, S. (2016). Inhibition of carbonic anhydrase potentiates bevacizumab treatment in cholangiocarcinoma. *Tumor Biology*, 37(7), 9023-9035.
- van der Meel, R., Vehmeijer, L. J., Kok, R. J., Storm, G., and van Gaal, E. V. (2013). Ligand-targeted particulate nanomedicines undergoing clinical evaluation: current status. *Adv Drug Deliv Rev*, 65(10), 1284-1298.
- Wang, Q., Zorn, J. A., and Kuriyan, J. (2014). A structural atlas of kinases inhibited by clinically approved drugs. *Methods Enzymol*, 548(1), 23-67.

- Wenzl, T., and Wilkens, J. J. (2011). Theoretical analysis of the dose dependence of the oxygen enhancement ratio and its relevance for clinical applications. *Radiation Oncology*, 6(1), 171.
- Wichert, M., and Krall, N. (2015). Targeting carbonic anhydrase IX with small organic ligands. *Current Opinion in Chemical Biology*, 26(1), 48-54.
- Winum, J.-Y. (2005). Carbonic anhydrase inhibitors : CA IX selective inhibitors incorporating aromatic or heterocyclic sulfonamide. *Expert Opinion on Therapeutic Patents*, 15(1), 233-236.
- Winum, J. Y., Colinas, P. A., and Supuran, C. T. (2013). Glycosidic carbonic anhydrase IX inhibitors: a sweet approach against cancer. *Bioorg Med Chem*, 21(6), 1419-1426.
- Winum, J. Y., Rami, M., Scozzafava, A., Montero, J. L., and Supuran, C. (2008). Carbonic anhydrase IX: a new druggable target for the design of antitumor agents. *Med Res Rev*, 28(3), 445-463.
- Yogo, T., Urano, Y., Ishitsuka, Y., Maniwa, F., and Nagano, T. (2005). Highly efficient and photostable photosensitizer based on BODIPY chromophore. *J Am Chem Soc*, 127(35), 12162-12163.
- Yu, D., Zha, Y., Zhong, Z., Ruan, Y., Li, Z., Sun, L., and Hou, S. (2021). Improved detection of reactive oxygen species by DCFH-DA: New insight into self-amplification of fluorescence signal by light irradiation. *Sensors and Actuators B: Chemical*, 339(1), 129878.
- Zhang, X.-F., Li, X., Niu, L., Sun, L., and Liu, L. (2009). Charge Transfer Photophysics of Tetra( $\alpha$ -amino) Zinc Phthalocyanine. *Journal of Fluorescence*, 19(6), 947.
- Zou, J., Yin, Z., Ding, K., Tang, Q., Li, J., Si, W., Shao, J., Zhang, Q., Huang, W., and Dong, X. (2017). BODIPY Derivatives for Photodynamic Therapy: Influence of Configuration versus Heavy Atom Effect. *ACS Applied Materials & Interfaces*, 9(38), 32475-32481.



APPENDIX

## APPENDIX

### PUBLICATION

**Pewklang, T.**, Wet-osot, S., Wangngae, S., Ngivprom, U., Chansaenpak, K., Duangkamol, C.; Lai, R.-Y., Noisa, P., Sukwattanasinitt, M., Kamkaew, A. (2021). Flavylium-based hypoxia-responsive probe for cancer cell imaging. **Molecules**. 26(16). doi: 10.3390/molecules26164938.

Treekoon, J., **Pewklang, T.**, Chansaenpak, K., Gorantla, J. N., Pengthaisong, S., Lai, R.-Y., Ketudat-Cairns, J. R., Kamkaew, A. (2021). Glucose conjugated aza-BODIPY for enhanced photodynamic cancer therapy. **Organic & Biomolecular Chemistry**. 19(26), 5867. doi: 10.1039/D1OB00400J.

Wangngae, S., **Pewklang, T.**, Chansaenpak, K., Ganta, P., Worakaensai, S., Siwawannapong, K., Kluaiphanngam, S., Nantapong, N., Lai, R.-Y., Kamkaew, A. (2021). A chalcone-based fluorescent responsive probe for selective detection of nitroreductase activity in bacteria. **New Journal of Chemistry**. 45(26), 11566. doi: 10.1039/D1NJ01794B.

Wet-Osot, S., **Pewklang, T.**, Chansaenpak, K., Chudapongse, N., Lai, R. Y., Kamkaew, A. (2021). One-Pot Synthesis of Coumarin-Indomethacin Hybrids as COX-2 Targeting Probes for Cancer Imaging. **ChemMedChem**. 16(10), 1660. doi: 10.1002/cmdc.202100003.

Rattanopas, S., Chansaenpak, K., Siwawannapong, K., Ngamchuea, K., Wet-Osot, S., Treekoon, J., **Pewklang, T.**, Jinaphon, T., Sagarik, K., Lai, R. Y., Cheng, L., Kamkaew, A., (2020). Synthesis and Characterization of Push-Pull Aza-BODIPY Dyes Towards Application in NIR-II Photothermal Therapy. **ChemPhotoChem**. 4(11), 5304. doi: 10.1002/cptc.202000164.

**Pewklang, T.**, Chansaenpak, K., Lai, R.-Y., Noisa, P., Kamkaew, A. (2019). Aza-BODIPY probe for selective visualization of cyclooxygenase-2 in cancer cells. **RSC Advances**. 9(24), 13372. doi: 10.1039/C9RA01948K

## CURRICULUM VITAE

<b>Name</b>	Miss Thitima Pewklang
<b>Date of birth</b>	August 27 <sup>th</sup> , 1996, Nakhon Ratchasima, Thailand
<b>Education</b>	
2015-2019	B.Sc. (Chemistry), First class honors, Suranaree University of Technology, Nakhon Ratchasima, Thailand
2019-Present	M.Sc. candidate (Organic Chemistry), Suranaree University of Technology, Nakhon Ratchasima, Thailand
<b>Scholarship</b>	
2019-Present	Development and Promotion of Science and Technology Talents Project (DPST), supported by the Thai government. Funding for graduate study from National Research Council of Thailand (NRCT).



มหาวิทยาลัยเทคโนโลยีสุรนารี